Chapter 1

Introduction

1.1 Overview of thermoacoustics

Thermoacoustics is a field of study which includes devices purpose-built to exploit the phenomenal interaction between heat and sound. Thermoacoustics has been demonstrated as an effective technology which can potentially serve a variety of purposes such as cryogenics, commercial refrigeration or electricity generation, without adverse environmental impact or commercial drawbacks such as expensive construction or maintenance costs or high part counts. Thermoacoustic refrigerators and electric generators can be driven directly using heat as an energy source, and therefore are an appealing technology for waste energy recovery. Examples of potential energy sources for thermoacoustic devices are solar collectors and hot exhaust gas streams from internal combustion engines and industrial burners.

Thermoacoustic systems developed to date have comparably lower 'power density' and lower thermal efficiency than existing well-developed, mature refrigeration technologies and critics of thermoacoustics cite these aspects as two major drawbacks. Issues regarding the perceived low power density and thermal efficiency are currently being addressed by the research community, by understanding the behaviour of devices at more intense (higher power density) operating conditions. Not all potential applications of thermoacoustics demand compactness and thermal

efficiency. An example is waste heat energy recovery on large industrial sites where space is relatively plentiful and hot gases are emitted on a large scale. As a technology with potential cost and environmental advantages for a wide range of applications in Australia and around the world, it may be a technology capable of arresting the human impact on climate change.

'Linear theory', which collectively refers to the quantitative one-dimensional thermoacoustic prediction tools and formulations developed over the last thirty years (Swift 2002, Rott 1980, Swift 1988, Ward & Swift 2001), has progressed to the point where effective design and optimisation of thermoacoustic devices operating *at low pressure amplitudes* can be made. However, high pressure amplitude operation of thermoacoustic devices has been shown to deviate significantly from linear theory predictions due to non-linear flow phenomena.

It is expected that thermoacoustic devices will need to operate at relatively high pressure amplitudes for commercial and practical applications, to achieve power densities similar to competing technologies. Where the accuracy of linear formulations deteriorates, analyses utilising higher order models and computational fluid dynamics (CFD) methods will be needed.

The numerical studies presented in this thesis were simulated using the commercial *Fluent* two-dimensional double-precision CFD environment. Models developed using the preprocessor *Gambit* were executed using a networked computing cluster.

1.2 Outline

The vast proportion of two-dimensional numerical studies specific to thermoacoustic devices in the literature have modelled what Wheatley et al. (1983) have termed a 'thermoacoustic couple' (TAC), which in its most abstract form is a single infinitely

wide plate in an oscillatory flow field. Presumably, the thermoacoustic couple is intended to provide a tractable means to approximate a stack consisting of many parallel plates. The aim of the current work is to investigate the thermoacoustic couple using advanced numerical models to a point where it may offer further insight into the operation of thermoacoustic systems. The specific aims are listed in Section 2.4.

The following paragraphs describe the contents of each chapter in this thesis.

Chapter 2 describes the basic operation of a thermoacoustic device and also presents a review of existing literature pertinent to the numerical study of thermoacoustic couples. Consideration of the state-of-the-art knowledge in **Chapter 2** leads to the conclusions that

- there is a lack of knowledge with regards to undesirable loss mechanisms in thermoacoustic devices operating at drive ratios in excess of 3%;
- the influence of stack plate thickness upon the distribution of effective heat transfer and efficiency of a thermoacoustic couple at drive ratios in excess of 3% has not been fully investigated;
- there is a lack of knowledge with regards to the effectiveness and efficiency of thermoacoustic stack plates with non-rectangular edge shapes; and
- time-averaged gas flow (also referred to as 'DC flow' or 'acoustic streaming') within parallel-plate thermoacoustic stacks has not been fully investigated.

Chapters 4 to 6 present studies that seek to address these knowledge gaps. In **Chapter 3**, advancements to the computational model representing the 'thermoacoustic couple' are introduced, and compared with published results. A computational model for the simulation of thermoacoustic couples of finite thickness

is presented along with studies of suitable solver, mesh and timescale parameters. Discussion regarding the level of agreement of the presented modelspace to published experimental data (Garrett 2004) is included.

Chapter 4 presents the results of an investigation into the influence of finite plate thickness upon the performance of thermoacoustic couples. In **Chapter 5**, thermoacoustic couples with various stack plate edge shapes are simulated to determine if non-rectangular edge shapes can improve the system thermodynamic performance compared to simple rectangular sections. **Chapter 6** presents an expanded multiple plate model which is used to investigate time-averaged mass streaming within parallel plate stack regions.

Chapter 7 summarises the findings drawn in Chapters 3 to 6. This final chapter provides conclusions from the current work and suggestions for future work in this area.

Appendix A lists the various animation files included with the electronic media attached to this thesis. The selection of various grid, solver and discretisation settings is discussed in **Appendix B**. Post-processing techniques used to generate the various figures presented in this thesis are described in **Appendix C**.

Appendix D presents several studies which investigate the applicability of the model developed in **Chapter 3** to numerical and experimental results obtained over much larger spatial and temporal scales. These studies give confidence that the simulation techniques employed in this thesis are suitably accurate.

The papers originating from the work presented in this thesis are listed in **Appendix E**.

Chapter 2

Background and previous work

The state-of-the-art knowledge and literature pertinent to this thesis are presented in the following subsections. Section 2.1 describes the principles of thermoacoustic device operation and the opportunities for the technology. Section 2.2 presents the development of first-order prediction tools for thermoacoustic devices, and Section 2.3 reviews the current progress on non-linear prediction tools. Section 2.4 discusses the research opportunities that this thesis addresses.

2.1 Thermoacoustic refrigeration

The term 'thermoacoustic' is often used in simple reference to conversion of thermal energy into acoustic energy and vice versa. However, thermoacoustic systems constructed to date are a complex application of both thermodynamic and acoustic theory.

Thermoacoustic systems are here divided into two different classes known as 'heat-engines' (also known as 'prime movers') and 'heat-pumps'. In principle, heat-engines take heat energy from a hot reservoir, convert some of the heat energy into acoustic energy and dump the unused heat to a cool reservoir. Heat-pumps use acoustic energy to 'pump' heat from one temperature reservoir to another,

resulting in a temperature gradient between the two reservoirs. When a heat-engine or other acoustic source is used to drive a heat-pump as shown in Figure 2.1, the overall mechanical system is termed a 'refrigerator'. Figure 2.1 shows a potential automotive application for a thermoacoustic refrigerator which uses the temperature difference between hot engine exhaust gases and outside ambient air to provide cooling of the cabin interior.

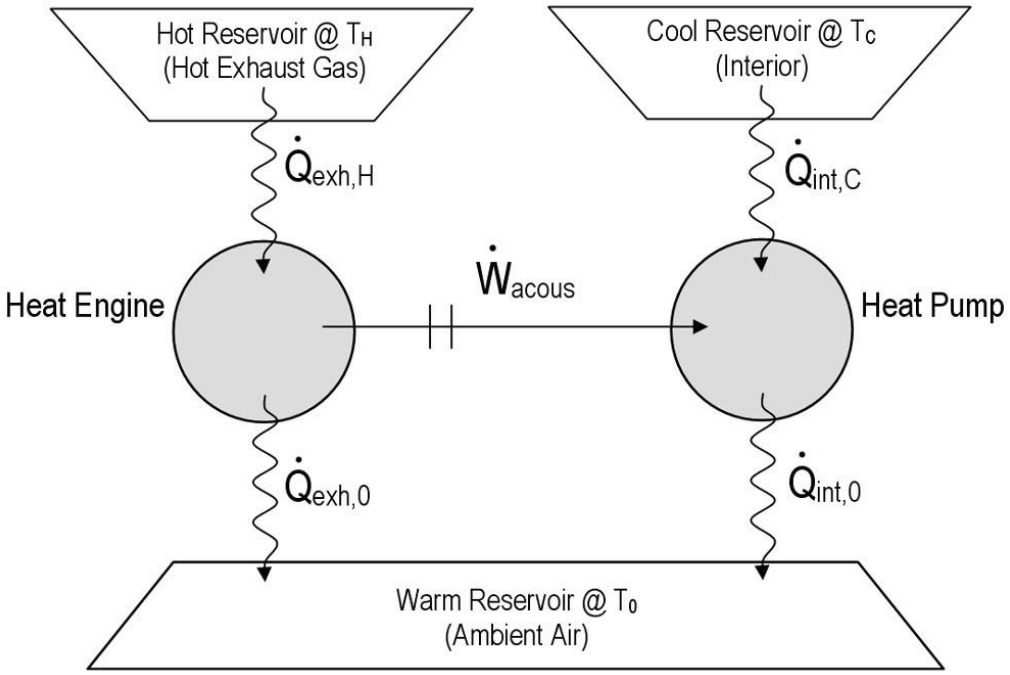

Figure 2.1: Example of an ideal thermoacoustic heat-engine driving an ideal thermoacoustic heat-pump for an automobile air conditioner.

Since the thermodynamic cycle by which thermoacoustic systems operate is ideally reversible, refrigerators are typically driven by either a mechanical gas displacement system (such as a loudspeaker) or a heat-engine. Loudspeakers or electrodynamic shakers convert electrical power into acoustic power, are relatively easy to implement and can be relatively inexpensive. However, heat-engines have typically higher efficiencies and have no moving parts, resulting in a much more extensive and robust operational lifetime. For example, Hofler & Adeff (2001) built a miniature thermoacoustic heat-engine using a flame or electrical source and a

horn which created a sound pressure level as high as 149dB re 20μPa at a frequency of 930Hz. Many experimental heat-engines use resistive heating elements to convert electrical power into thermal power, which the heat-engine itself converts into acoustic power. Purpose-built heat-engines may use any heat source such as solar radiation, hot waste gases from industrial plants, or exhaust gases from internal combustion engines.

Various aspects of thermoacoustic systems are briefly discussed in the following sections.

2.1.1 Principles of operation

Figure 2.2(a) shows a sketch of a simple half-wavelength standing-wave thermoacoustic heat-pump, in which the fluid inside the tube is excited by an acoustic source (not shown) such as a loudspeaker or heat-engine. An important component termed a 'stack' is located in the tube between a hot heat exchanger (HHX) and a cold heat exchanger (CHX), and its purpose is to provide thermal capacity and maintain imperfect thermal contact with the oscillating fluid. This imperfect thermal contact between the gas and the solid stack introduces a shift in phase between the temperature and pressure oscillations of each gas 'parcel'. It will be shown that this phase shift is a key mechanism to effective heat-pumping within the stack region. The distances over which each gas parcel moves in one period of oscillation are much less than the length of the stack plate. One may compare the process of heat transfer across the stack to a 'bucket brigade', where many small pumping actions along the stack combine together in series to create effective heat transfer from one end of the stack to the other.

The stack in thermoacoustic devices vary in geometry and construction but all provide a series of narrow gaps through which the fluid oscillates. Stacks are

often constructed by assembling a stack of thin plates (Tijani et al. 2002*a*), rolling up a sheet into a spiral (Tijani et al. 2002*a*) or drilling holes through solid billets (Hatazawa et al. 2004). Recent analytical studies (Wakeland & Keolian 2002*b*, 2004) indicated that thermoacoustic heat-pumps could operate without a stack. The design, construction and execution of a stackless device of comparable efficiency to devices with stacks are "workable", although they have geometry constraints requiring the enclosure to have a large ratio of exchanger area to sidewall area.

For thermoacoustic devices incorporating stacks, the stack is 'sandwiched' between heat exchangers designated in Figure 2.2(a) as the cold heat exchanger (CHX) and hot heat exchanger (HHX). The thermoacoustic effect occurs at all interior surfaces, but is most effective within the stack and heat exchanger region. The effect produces small incremental movements of heat which overall combine to 'pump' heat from the CHX to the HHX, cooling the CHX. During intended operation, heat is transferred to the exterior environment via the HHX, and heat is drawn from the exterior environment into the CHX, providing refrigeration.

Figure 2.2(b) shows the distribution of pressure and velocity throughout the device shown in Figure 2.2(a). The device operates at a frequency corresponding to the first acoustic mode, in this case that of a half-wavelength resonator. The acoustic velocities are minima at the terminations of the tube, and a velocity antinode is present at the midsection where the acoustic impedance is at a minimum.

Figure 2.2(c) shows a close-up sketch of the stack in Figure 2.2(a), showing the stages in which the thermoacoustic heat-pump cycle operates. The first and second graphs of Figure 2.2(d) indicate the temperature versus position, and pressure versus volume of a parcel of fluid oscillating inside the stack, respectively. With reference to Figures 2.2(c) and 2.2(d), consider a parcel of fluid oscillating along the axis

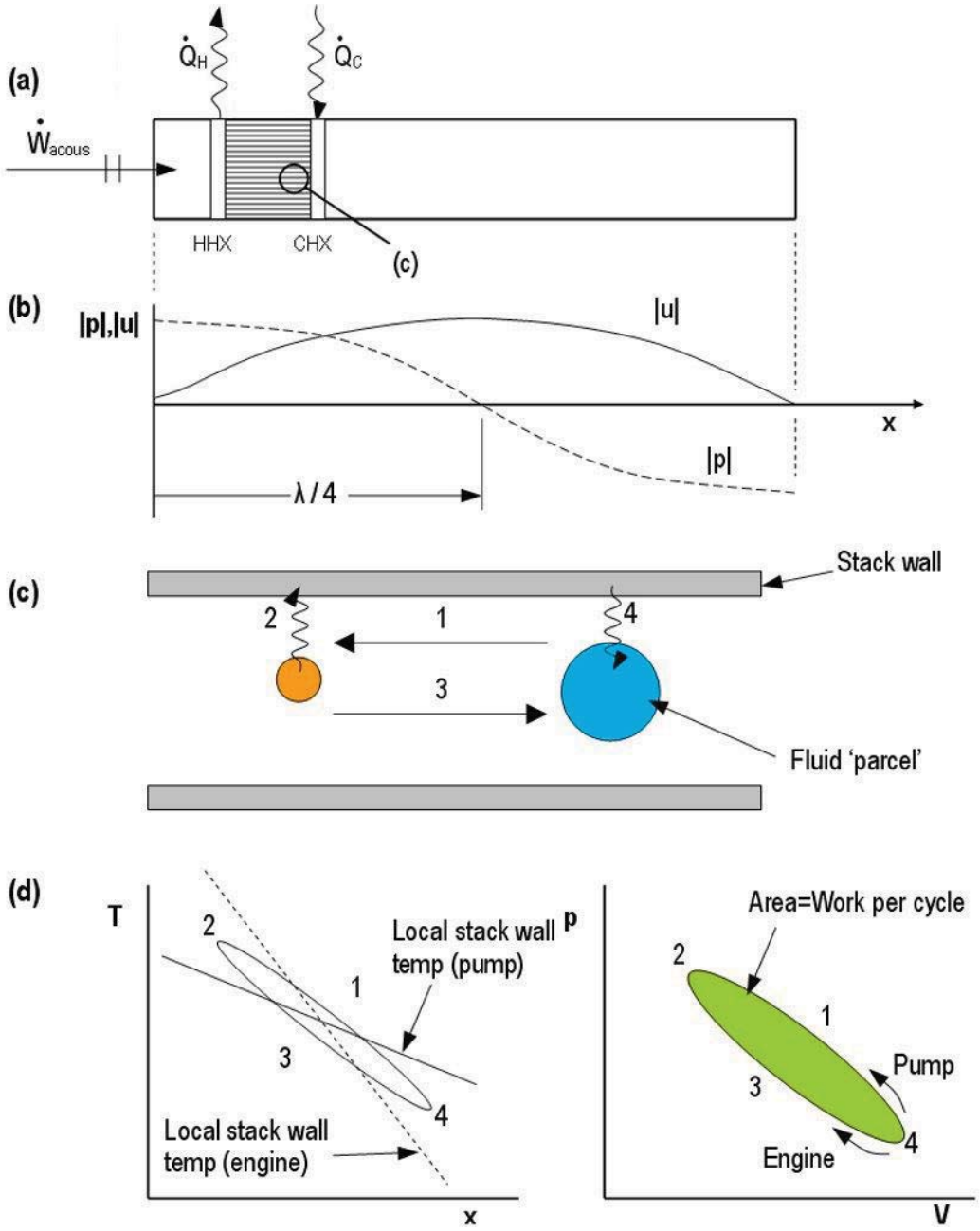

Figure 2.2: (a) Diagram of a half-wavelength thermoacoustic pump; the tube is closed at each end and an acoustic source (such as a loudspeaker) is used to pump heat; (b) Distribution of acoustic pressure and velocity amplitude along the axis of the device shown in (a); (c) Sketch of the thermodynamic cycle of a gas parcel inside the stack shown in (a); (d) Temperature versus position, and pressure versus volume for the gas parcel shown in (c). (a) and (b) adapted from Wetzel & Herman (1997), (c) and (d) adapted from Backhaus & Swift (2002).

of the device, in thermal contact with the stack plates. The four stages of the thermoacoustic heat-pump cycle that the fluid experiences are:

1. **Compression**: The parcel of fluid is compressed as it moves from a lower pressure region to a higher pressure region, which causes an increase in its temperature;

2. **Cooling**: The fluid parcel in its compressed state is hotter than the local stack temperature, so heat is transferred to the stack, cooling the parcel;

3. **Expansion**: The parcel is returned to a lower pressure, and under expansion the fluid experiences a decrease in temperature; and

4. **Heating**: The parcel is now colder than the local stack temperature, so heat is transferred from the stack to the fluid.

The material of the stack and its surrounding walls is usually selected to be of good thermal capacity but poor thermal conductivity, such that little heat is conducted from the HHX to the CHX via axial conduction in the wall. It is desirable for the two heat exchangers to each have excellent thermal conductivity for contact with external heat sources and sinks. In this way, heat is 'pumped' up a thermal gradient between the ends of the stack, which are themselves exchanging heat with the exterior of the device.

The thermodynamic cycles presented in Figures 2.2(c) and 2.2(d) are reversible and may therefore also be used to describe the operation of thermoacoustic heat-engines. Thermoacoustic heat-engines operate in reverse to heat-pumps and generate an acoustic response from an applied temperature gradient across the stack ∇T_{stack}. When the thermal gradient in the stack sufficiently exceeds what is commonly termed the critical temperature gradient, an acoustic response in the stack is spontaneously generated. The critical temperature gradient ∇T_{crit} is defined as (Swift 2002, Equation 4.44)

$$\nabla T_{\text{crit}} = \frac{\omega A \left|p_1\right|}{\rho_m c_p \left|U_1\right|}, \tag{2.1}$$

where ω is the radial frequency, A is the cross-sectional area, $|p_1|$ is the acoustic pressure amplitude, ρ_m is the mean gas density, c_p is the gas thermal capacity and $|U_1|$ is the acoustic velocity amplitude. The adverb 'sufficiently' is used since while this criterion is valid for an inviscid working fluid, viscous effects result in the need for higher temperature gradients to operate real devices (Swift 2002).

In practice, the thermal gradient is often applied by heating the HHX whilst maintaining the CHX at ambient temperature, although cooling of the cold heat exchanger, using say liquid nitrogen (Wheatley et al. 1986), has also been proven to be effective. Conventionally, when one heat exchanger is held at ambient temperature it is instead referred to as the ambient heat exchanger (AHX). For example, studies of practical heat-engines will refer to a HHX and an AHX, whereas the two heat exchangers in a heat-pump are usually referred to as the AHX and CHX.

The relationship between the applied temperature gradient and resultant acoustic pressure amplitude within heat-engines may be described by a hysteresis loop (Chen & Jin 1999). This means that if the input heat source for a thermoacoustic heat-engine is shut off and the applied temperature gradient decreases, the operation of the device will continue for some time even with the condition $\nabla T_{stack} \leq \nabla T_{\text{crit}}$.

2.1.2 Geometry and performance scales

Common scales exist for the operating states and geometry of thermoacoustic devices and are often cited in literature concerning the design and optimisation of such devices (Wetzel & Herman 1997, Swift 2002). The blockage ratio

$$BR = \frac{\text{ratio of open area}}{\text{total cross-sectional area}} \tag{2.2}$$

is often used to describe the portion of open area through a stack or regenerator, and is used to characterise the performance of systems for various stack configurations. For a stack comprising many parallel plates each $l{=}2t_s$ thick and centred $2y_0$ apart,

$$BR \approx \frac{y_0 - t_s}{y_0}. \tag{2.3}$$

The drive ratio is calculated as

$$DR = \frac{|p_1|}{p_m} \tag{2.4}$$

and is the ratio of the amplitude of the acoustic (dynamic) pressure, p_1, to mean (static) pressure, p_m, and is typically expressed as a percentage. Wetzel & Herman (1997) acknowledge that the DR is a useful indicator of the nonlinearity of the system, since it is linked to the acoustic Mach number and hence the flow velocity.

Two length scales of interest to a designer of thermoacoustic stacks are the thermal penetration depth, δ_κ, and the viscous penetration depth, δ_υ. Swift (2002, p7) defines these scales as

$$\delta_\kappa = \sqrt{\frac{2k}{\rho_m c_p \omega}} \tag{2.5}$$

and

$$\delta_\upsilon = \sqrt{\frac{2\mu}{\rho_m \omega}} \tag{2.6}$$

where k is the thermal conductivity of the working fluid, ρ_m is the mean fluid density, c_p is the fluid thermal capacity, ω is the radial frequency, and μ is the dynamic viscosity. Swift notes that

> *"These characteristic lengths tell us how far heat and momentum can diffuse laterally during a time interval of the order of the period of oscillation divided by π. At distances much greater than these penetration depths from the nearest solid boundary, the gas feels no thermal contact or viscous contact with the solid boundaries ... Clearly the heat exchange components in thermoacoustic systems must have lateral dimensions of the order of δ_κ in order to exchange heat with the working gas."*

It would therefore seem appropriate to set the half-thickness of the stack plates t_s equal to δ_κ, since plate material at depths greater than this value do not participate in contributing to the thermoacoustic effect and instead contribute more so to the physical flow resistance through the stack region.

The gas displacement amplitude $|\xi_1|$ is defined as (Swift 2002, p7)

$$|\xi_1| = \frac{|u_1|}{2\pi f} \tag{2.7}$$

where u_1 is the acoustic velocity, f is the frequency and $2\pi f{=}\omega$. $2|\xi_1|$ approximates the total axial distance a parcel of gas moves in one period of oscillation. Both δ_κ and δ_v are expected to be smaller in length than $|\xi_1|$, which is in turn smaller than the acoustic wavelength $\lambda{=}c/f$.

2.1.3 Working gases

To reduce costs and device complexity, many experimental and didactic thermoacoustic devices use air itself as the working fluid. However, the majority of

purposeful thermoacoustic systems use helium or a binary mixture of noble gases such as helium and argon or helium and xenon. The choice of working gas is often based upon the thermoacoustic power density, which Swift (1988, p205) determined to scale with $p_m cA$, the product of mean pressure, sound speed, c, and cross sectional area, A. Since helium has the highest sound velocity and thermal conductivity of all inert gases (Tijani 2001), it makes for an excellent initial design choice. The high sound velocity and high thermal conductivity and associated increased δ_κ (see Section 2.1.2) allow the construction of relatively high-frequency devices without being too small in dimension. The high thermal conductivity increases the thermal penetration depth of the device, which increases the stack geometry to sizes that can be accommodated by relatively inexpensive manufacturing methods (Swift 2002).

Other noble gases such as argon and xenon have been added to helium to improve the efficiency of thermoacoustic systems. The addition of these heavier gases to helium is designed to reduce the Prandtl number, σ, of the working gas, which in turn reduces viscous dissipation losses throughout the system (Swift 2002). Noting that *"the smaller the Prandtl number the bigger the thermal effects (heating and cooling)"*, Merkli & Thomann (1975*b*) suggested that the effectiveness of thermoacoustic devices could be maximised through careful selection of working gas. More recently, Wetzel & Herman (1997) demonstrated that using a 62%-38% He-Xe mixture led to a doubling in the relative coefficient of performance (COP_r) of the system. However, from a design standpoint, power density was traded for efficiency: the addition of xenon vastly reduced the sound speed of the working gas, reducing the system power density.

Thermoacoustic devices are unique amongst potential automotive refrigeration systems in their use of helium gas. The environmental benefits that exist using

helium in thermoacoustics over conventional refrigeration technologies include

- zero global warming potential (GWP) from direct emissions;
- zero ozone depletion potential (ODP) from direct emissions;
- the working gas is non-toxic and non-combustible; and
- the working gas does not necessarily need to be recaptured if replaced.

Other refrigerants used in rival refrigeration technologies such as ammonia, butane, propane, HFCs, CFCs, HCFCs, and carbon dioxide have one or more of these issues associated with their use.

2.1.4 Electrodynamic drivers (loudspeakers)

The use of simple 'off the shelf' loudspeakers is an option for an extremely low-cost thermoacoustic refrigerator, although more efficient thermoacoustic refrigerators have been constructed using custom-built electrodynamic shakers, highly-modified loudspeakers or compression drivers. Reid & Swift (2000) demonstrated the use of simple generic loudspeakers in a thermoacoustic refrigerator, however small external modifications (in the form of water cooling jackets) were applied to the loudspeaker coils to prevent overheating.

Good quality standard loudspeakers in thermoacoustic devices typically have an electroacoustic efficiency of less than 5% (Tijani et al. 2002*b*). An electroacoustic circuit analysis by Wakeland (2000) found that the efficiency of a loudspeaker for a thermoacoustic application could be vastly improved by matching the driver to the acoustic load, such that the loudspeaker was driven at resonance. This included the suggestion of adjusting the mechanical stiffness of the driver by placing an enclosed volume of gas behind the driving piston face to act as a gas 'spring.' A thermoacoustic refrigerator incorporating a loudspeaker coil driver and the gas

spring concept was built in 2001 by Tijani et al. (2002*b*) and delivered measured electroacoustic efficiencies in excess of 35%. Using a commercial purpose-built acoustic source in a thermoacoustic refrigerator, an electroacoustic efficiency of 60% was achieved by Mongeau et al. (2001).

The PhD thesis of Hofler (1986) presents the construction details and experimental data for a small thermoacoustic cryogenic refrigerator in which the electric driver was a voice coil from a simple conventional loudspeaker. Displacement of the working fluid was achieved using a lightweight aluminium cone attached to the moving voice coil, which presented a flat vibrating piston face. The 'Shipboard Electronics Thermoacoustic Chiller' (SETAC), previously referred to as the 'Thermoacoustic Life Science Refrigerator' (TALSR), was designed by Garrett (1997) and is another example of a thermoacoustic refrigeration device operated by electrodynamic drivers. The SETAC design had an interesting 'U-tube' configuration with two electrodynamic drivers for the sake of redundancy in case one of the loudspeakers failed. The SETAC (Garrett 1997) was the first device to use loudspeakers designed and built specifically for a thermoacoustic application, which carried very high levels of electroacoustic efficiency ($\approx$50%) and power (up to 100W acoustic power) (Poese & Garrett 2000). The SETAC was designed to provide cooling for racks of electronics onboard a warship. Another more publicised design was a compact thermoacoustic refrigerator (Smith et al. 2004) for cooling an icecream display cabinet, for which its high power density and use of a compact electrodynamic driver were notable.

2.1.5 Historical origins of thermoacoustic devices

According to Tijani (2001), observations of possibly the first working heat-engines, termed 'singing flames', were recorded by Higgins (1802) in 1777. These devices were found to produce sound by placing a naked candle flame at a specific location inside a vertical glass tube, open at each end. 19th century glassblowers were

also witness to the phenomenon of heat-generated sound, when the temperature differential between the hot bulb end and open end of cooling glass tubes caused the tubes to generate audible tones (Swift 1988). Sondhauss (1850) in the mid 19th century was able to relate the acoustic tone frequency to the physical geometry of the tubes. These cylindrical devices, closed and heated at one end and open at the other, were termed Sondhauss tubes.

Rijke (1859) found that vertical glass tubes open at each end could also produce audible tones when a heated screen was placed approximately one-quarter length from the bottom of the tube. His observations published in 1859 suggested that for operation of these tubes, since called Rijke tubes, convective air flow was necessary through the tube (such that a thermal gradient could be established inside). Matveev & Culick (2003) performed experiments with a Rijke tube at approximately ambient mean temperature and pressure to determine the gas flow rates, heater position and heat inputs for which the system produced an acoustic response. The authors referred to this event as the point of system instability; in thermoacoustic nomenclature, this point is usually defined by the critical temperature gradient.

The next major development in heat-engines was in the 1940s, when according to Ceperley (1979), Bell Telephone Laboratories in the United States received a patent for electrical generators which converted the acoustic power from Sondhauss tubes into useful levels of electrical power. Ceperley noted that whilst these devices were attractive in terms of their comparable simplicity in construction, they were inefficient since their design was based around standing waves (as opposed to travelling-wave systems). It seems that to this point in time, no standing-wave heat-engine has achieved thermal efficiencies in excess of 20% (Backhaus & Swift 2000).

A detailed review article by Swift (1988) cites the dissertation of Feldman (1966), which showed that the addition of a porous media into a Sondhauss tube (such as a stack of parallel plates) increased the thermoacoustic efficiency and power output. This concept was considered by Swift to be a major milestone in the development of experimental thermoacoustics.

According to Swift (1988), theoretical modelling of the complex thermoacoustic environment in detail did not begin until the late 1960s. Swift describes Rott and colleagues as the developers of useful theoretical formulation for thermoacoustic devices, citing their progressive development in articles from 1969 until 1983. Rott's equations have formed a solid basis for the design of low-amplitude thermoacoustic heat-engines and pumps, and his work of 1980 (Rott 1980) is considered to be the foundation from which modern thermoacoustics has developed.

2.1.6 Modern thermoacoustic engines

In the late 1970s, Ceperley (1979) found that the phasing of acoustic velocity and pressure in a travelling-wave was similar to that of the Stirling cycle, as shown in Figure 2.3. Prior to this point, thermoacoustic heat-engines were of standing-wave form, whereby the acoustic pressure lagged the gas velocity by 90°. In a Stirling engine, heating and cooling phases are in phase with pressure (Figure 2.3(c)). Ceperley noted that travelling-waves consisted of acoustic velocity and pressure components in phase, in similar fashion to the Stirling cycle. To explain why standing-wave heat-engines also worked despite pressure and velocity not being in phase, Ceperley noted that in a standing-wave heat-engine, additional thermal delays in the system meant that effective heating occurred during high pressure and vice versa to achieve Rayleigh's criterion. By this, he found that the most effective standing-wave heat-engines possessed heating and cooling phases which,

like the pressure, lagged the acoustic velocity by 90°. Since the travelling-wave heat-engine does not require this thermal delay, it is ideally a reversible process with the capacity for higher efficiencies (Ceperley 1979). According to Gardner & Swift (2003), the potential efficiency increase of a travelling-wave design over that of a standing-wave design is 50%.

Further to this, Ceperley (1979) proposed a toroidal-shape travelling-wave heat-engine, in which the acoustic flow of the working gas was circulated back to form a positive-gain closed-loop system. In this arrangement, the acoustic power leaving the hot end of the regenerator was fed back to the cold end of the regenerator, to amplify the acoustic power output. In 1999, researchers at the Los Alamos National Laboratory in New Mexico, USA, constructed a thermoacoustic refrigerator driven by a toroidal-shape travelling-wave type heat-engine, titled the Thermoacoustic Stirling Heat Engine (TASHE) (Backhaus & Swift 2000), shown in Figure 2.4.

The research in New Mexico by Backhaus & Swift (2000) on the development of the TASHE also addressed two major efficiency losses found in heat-engines: boundary layer flow losses termed 'Rayleigh streaming' and a time-averaged mass flow effect found in closed-loop travelling-wave engines, termed 'Gedeon streaming.' Rayleigh streaming losses were identified by Olson & Swift (1997) as a convective heat loss along the walls of the tube generated by the acoustic oscillation, and were successfully reduced by using a carefully selected tube taper angle. Gedeon streaming was identified as a significant loss mechanism, since the time-averaged mass flow carried heat away from the hot exchanger and returned it to the cold exchanger via the feedback path, eroding the heat difference across the stack. Backhaus & Swift (2000) successfully addressed Gedeon streaming by introducing an orifice-plate type obstruction next to the cold heat exchanger. High acoustic

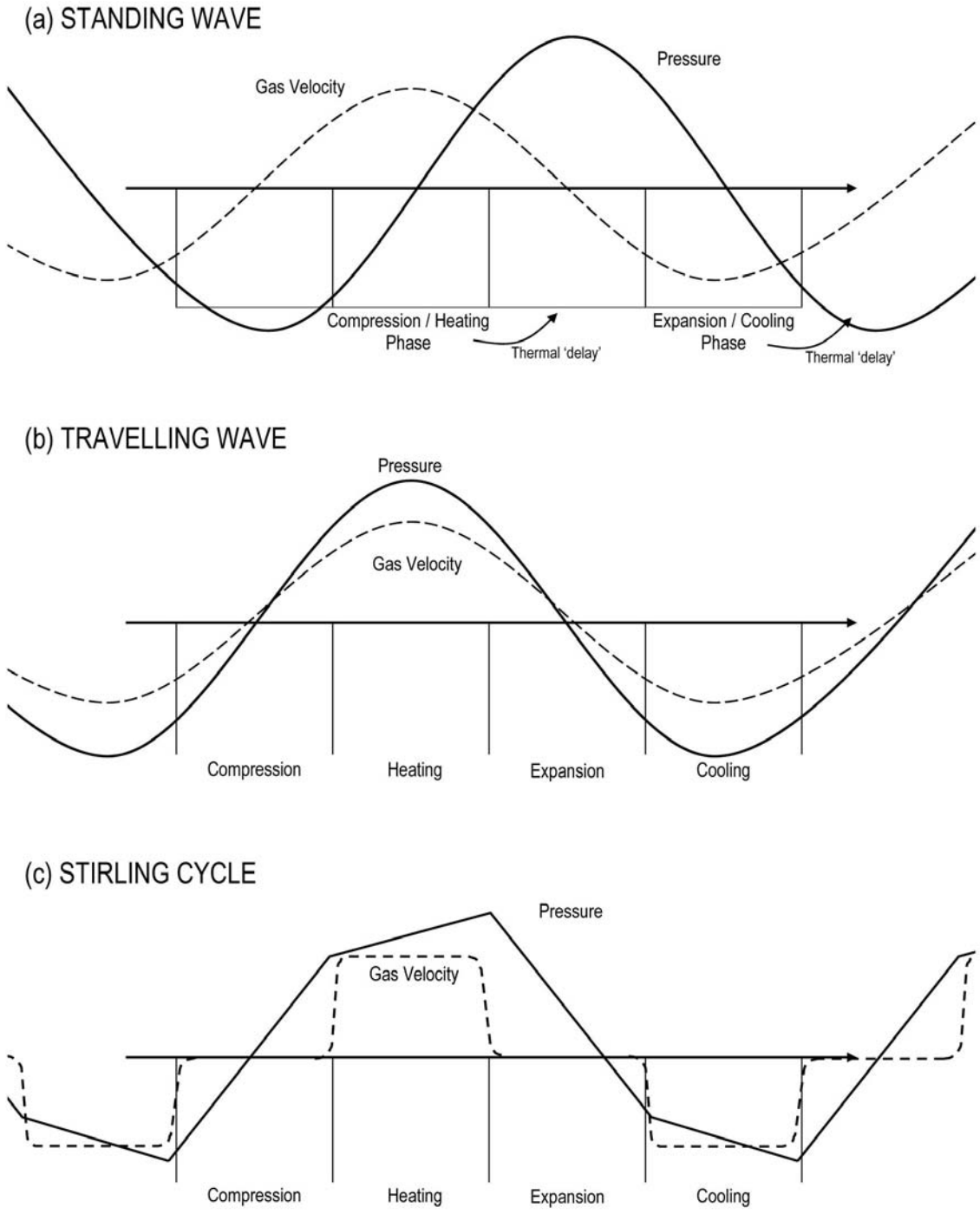

Figure 2.3: Plots of pressure and velocity versus time for various thermodynamic cycles: (a) Standing Wave, showing 90° phasing between acoustic velocity and pressure; (b) Travelling Wave, showing acoustic velocity and pressure in phase; and (c) Stirling Cycle. The thermal 'delay' in standing-wave devices discussed in the text is indicated in (a). (a) and (b) adapted from Ceperley (1979), (c) adapted from Garrett & Backhaus (2000).

.

NOTE: This figure is included on page 21 of the print copy of the thesis held in the University of Adelaide Library.

Figure 2.4: The TASHE refrigerator (reproduced with permission from Swift (2002, p23)). © The Acoustical Society of America.

velocity through the orifice plate created a turbulent region in which a sufficient pressure drop formed to choke the time-averaged mass flow. Using these controls, a thermal efficiency of 30% was achieved. The additional design and manufacturing effort involved in addressing Gedeon streaming is a drawback to the development of travelling-wave devices.

Construction and performance details of a third generation thermoacoustic heat-engine, termed a 'cascade' thermoacoustic engine, were published in 2003 by Gardner & Swift (2003). Cascade thermoacoustic devices comprise thermoacoustic stack elements with both standing and travelling-wave phasing. The output of a standing-wave heat-engine is amplified by two travelling-wave engines in series, forming a straight-line configuration. As noted by the authors, the removal of acoustic feedback (recirculation) loops eliminated Gedeon streaming, whilst the location of efficient travelling-wave engines at a zero phase loci (positions at which the acoustic field is purely 'travelling-wave') further improved the system efficiency. Despite incorporating several design parameters known to reduce efficiency, such as the use of pure argon gas (as opposed to helium), a less-than-optimal mean pressure and the use of honeycomb instead of parallel plate stacks, the cascade

engine delivered 2kW of acoustic power at 20% efficiency (Gardner & Swift 2003). The authors noted the high probability of a revised future cascade engine design reaching at least the efficiency of the TASHE (Gardner & Swift 2003). From a manufacturing viewpoint, the linear design topology of the cascade engine is more appealing than the toroidal section of the TASHE.

Backhaus et al. (2004) presented a novel thermoacoustic electric generator which shows promising efficiency. The electric generator is actually a pair of lubrication-free linear alternators located in opposition to each other at a pressure antinode of a travelling-wave engine. At its most efficient operating point, the generator outputs 39W of 120Hz alternating current with a heat to electricity conversion efficiency of 18% and a drive ratio of 6.3%. The applied focus of the device is seen in its differences to previous thermoacoustic systems: the device is highly pressurised ($p_m = 5.5MPa$) compared to previous thermoacoustic systems, but relatively small; and the flat surfaces presented by the hot heat exchanger are better suited to external heating sources such as solar or hot exhaust gases from a combustion process.

2.2 Linear prediction models

With the advancement of inexpensive computing resources, numerical prediction tools reduce the overhead and expense of developing new products. This is especially true for thermoacoustic devices, which are very sensitive to the operational states of the device, and require an iterative design approach. For example, subtle changes in the temperature distribution within the device lead to changes in the natural frequency and hence the efficiency of the device at the intended operating point.

A review of the numerical models commonly used in the design of thermoacoustic systems is presented in the following subsections.

2.2.1 The 'standard' linear formulation

'Linear theory', which collectively refers to the quantitative one-dimensional thermoacoustic prediction tools and formulations developed over the last forty years (Rott 1969, 1975, 1980, Swift 1988, Ward & Swift 2001, Swift 2002), has progressed to the point where effective design and optimisation of thermoacoustic devices operating *at low amplitudes* can be made. Low amplitude operation is here considered to be the range of operating conditions for which the drive ratio DR is less than three per cent.

The linear theory includes assumptions that the device geometry and flow of energy are one-dimensional and along a path extending from one termination to the other along the central axis of gas oscillation. Standing wave devices are therefore approximated using a series of one-dimensional segments which extend from termination to termination. In this context, the linear theory is also referred to as a set of 'first-order' approximations.

The set of first-order linear approximations developed by Rott (1980) was perhaps the first quantitative representation of thermoacoustic devices. With sufficient boundary condition data, Rott's acoustic approximations could be used to estimate the steady-state complex pressure, complex volume velocity and temperature of the working gas in one-dimension along the central axis of the device. Tominaga (1995) notes that Swift's review of thermoacoustic engines (Swift 1988) later extended the formulation to consider the effect of finite heat capacity of solids in contact with the working gas.

Specifically for a parallel plate stack, these approximations are summarised by Swift (2002, Equations 4.54, 4.70) as

$$dp_1 = -\frac{j\omega\rho_m dx/A}{1-f_v}U_1 \tag{2.8}$$

and

$$dU_1 = -\frac{j\omega A dx}{\gamma p_m}[1 + (\gamma - 1)f_\kappa]p_1 + \frac{(f_\kappa - f_\upsilon)}{(1 - f_\upsilon)(1 - \sigma)}\frac{dT_m}{T_m}U_1 \tag{2.9}$$

with mean gas density ρ_m, radial frequency ω, gas area A, first-order terms pressure p_1, particle velocity U_1, mean temperature T_m, ratio of specific heats γ, Prandtl number σ, with thermoviscous functions

$$f_\kappa = \frac{\tanh\left[(1 + j)y_0/\delta_\kappa\right]}{(1 + j)y_0/\delta_\kappa} \tag{2.10}$$

and

$$f_\upsilon = \frac{\tanh\left[(1 + j)y_0/\delta_\upsilon\right]}{(1 + j)y_0/\delta_\upsilon}. \tag{2.11}$$

The terms f_κ and f_υ can be calculated from the plate half-spacing y_0, the thermal penetration depth

$$\delta_\kappa = \sqrt{\frac{2k}{\rho_m c_p \omega}} \tag{2.12}$$

and viscous penetration depth

$$\delta_\upsilon = \sqrt{\frac{2\mu}{\rho_m \omega}} \tag{2.13}$$

with wavenumber k, dynamic viscosity μ and thermal capacity c_p. The thermoviscous functions f_κ and f_υ are based upon the geometry of the stack pores and their derivation follows from a previous analytical study by Arnott et al. (1991) of heat and work flows of arbitrary thermoacoustic stack cross sections such as parallel plates, rectangular or circular pores. The terms f_κ and f_υ can be considered to

represent the level of 'intimacy' between the oscillating fluid and surrounding solid structures.

Using a suitable discretisation method for the axial direction x, this formulation enables resolution of complex pressure p_1, complex volume velocity U_1 and temperature T at all positions within the device. This is a basic description of the method implemented in the thermoacoustic modelling program *DeltaE* (Ward & Swift 2001).

An alternative numerical implementation of the previous equations is the program titled Design Simulation for ThermoAcoustic Research (DSTAR). *DSTAR* is a numerical code originally developed by E.W. Purdy (Curtis 2000) that is designed to solve the ODE

$$\begin{aligned}\frac{dT'}{d(kx)} &= T' \ \mathrm{Im}\left[\frac{dP'^*}{d(kx)}P'\left(1-f_\upsilon^*-\frac{f_\kappa-f_\upsilon^*}{(1+\epsilon_s)(1+\sigma)}\right)-\dot{H}_2'\right] \\ &\div \ \{\frac{T'}{(\gamma-1)(1-\sigma)}\left[\frac{dP'}{d(kx)}\right]^2 \mathrm{Im}\left[1-f_\upsilon^*-\frac{(f_\kappa-f_\upsilon^*)(1+\epsilon_s f_\upsilon/f_\kappa)}{(1+\epsilon_s)(1+\sigma)}\right] \\ &\quad +\frac{2\gamma(k_0+k_s/y_0)kT_m}{p_m c}\left(\frac{p_m}{p_1}\right)^2\} \end{aligned} \tag{2.14}$$

derived from the second-order enthalpy flux (Swift 1988, Equation 55)

$$\begin{aligned}\dot{H}_2 &= \frac{\Pi y_0}{2\omega p_m}\mathrm{Im}\left[\frac{dp_1^*}{dx}\left(1-f_\upsilon^*-\frac{T_m\beta(f_\kappa-f_\upsilon^*)}{(1+\epsilon_s)(1+\sigma)}\right)\right] \\ &+ \frac{\Pi y_0 c_p}{2\omega^3 p_m(1-\sigma)}\frac{dT_m}{dx}\frac{dp_1}{dx}\frac{dp_1^*}{dx}\times\mathrm{Im}\left[f_\upsilon^*+\frac{(f_\kappa-f_\upsilon^*)(1+\epsilon_s f_\upsilon/f_\kappa)}{(1+\epsilon_s)(1+\sigma)}\right] \\ &- \Pi(y_0k_0+t_sk_s)\frac{dT_m}{dx}, \end{aligned} \tag{2.15}$$

with the plate heat capacity ratio (Swift 1988, Equation 59)

$$\epsilon_s = \frac{\rho_m c_p \delta_\kappa \ \tanh\left[(1+j)y_0/\delta_\kappa\right]}{\rho_s c_{ps} \delta_{\kappa s} \ \tanh\left[(1+j)t_s/\delta_{\kappa s}\right]} \tag{2.16}$$

where Π is the internal perimeter, t_s is the plate half-thickness, and β is the thermal expansion coefficient. The asterisk (*) represents the complex conjugate and P', T' and $\dot{H}_2'$ (Equation (2.14)) are dimensionless terms defined by Curtis (2000, p77) using localised states of pressure p, temperature T and total energy flux $\dot{H}_2$ respectively. The major advantages apparent in use of *DSTAR* over *DeltaE* are the graphical interface and the option to select either an initial value problem (IVP) or boundary value problem approach (BVP). Curtis (2000) investigated the accuracy and effectiveness of *DSTAR* Version 1.0 through comparison with experimental data obtained from a simple standing-wave engine. Although *DSTAR* was shown to consistently underestimate the operating temperature by ten to fifteen percent and the operating frequency by approximately 3%, Curtis concluded that "DSTAR does an accurate job of simulating the operation of an actual device".

The program *Sage* (Gedeon 1995) is described by Swift (2002) as similar to *DeltaE* on the basis that it considers the device as a one-dimensional network of connected segments, but provides improved accuracy for high amplitude devices. Unlike *DeltaE*, *Sage* was developed initially from finite difference approximations and can account for higher order harmonic content. In comparing the suitability of *Sage* and *DeltaE* to modelling thermoacoustic systems, Kotsubo (2005) stated that

> *"... (in general) there is very good agreement between the two codes, with the exceptions being conventional thermoacoustics stacks, where* Sage *loses accuracy, and low temperatures, where* DeltaE *does not include real gas properties."*

On the basis of the comparison made by Kotsubo (2005), *DeltaE* is considered to be more accurate for modelling the performance of thermoacoustic couples.

2.2.2 On the effectiveness of linear numerical models

The linear theory does not fully characterise the flow and energy fields in physical thermoacoustic devices, and several studies (Worlikar et al. 1998, Piccolo & Cannistraro 2002) have used this basis to suggest that the accuracy of linear prediction tools may actually break down at drive ratios below 3%. This has prompted a number of scholars to challenge the notion that the linear theory 'works well' for DR <3%.

Central to the application of linear theory is the inviscid short-stack boundary layer approximation (SSBLA), which does not take into account higher-order flow conditions such as entrance or exit effects for flow around stack channels. In terms of flow structure, the stack plates are considered to have zero thickness and be of infinite length. However, the SSBLA also assumes that the stack plates are 'short stacks' that are much shorter than the acoustic wavelength. Furthermore, Cao et al. (1996, p3456) note that according to Rott's approximations, the time-averaged heat-flux between the working gas and solid is zero, a finding they describe as "another reason to doubt (Rott's analysis) applicability in heat exchangers".

In physical examples of thermoacoustic systems where the plate has finite thickness and length, the resultant flow impedance leads to unique flow structures about the stack. These flow structures are expected to contribute to linear prediction errors at drive ratios above a limit that Poese & Garrett (2000) consider to be approximately DR=3%. Note that the same flow structures may be present at or below the 3% limit but are considered to have negligible impact upon the performance of the device.

Despite these concerns, *DeltaE* is demonstrably effective as a linear prediction tool for the initial design of low-amplitude thermoacoustic systems, whereby the

flow is considered laminar, and second-order effects are considered to be of little importance. Criticisms of the DR=3% 'linear theory' accuracy limit often cite an equation derived by Wheatley et al. (1983, Equation 17) for estimation of steady-state temperature difference as an example of applied 'linear theory'. The study by Atchley et al. (1990, Equation 1) which compared experimental temperature distributions with this equation found significant errors at drive ratios as low as 1.1%. A form of this equation was also demonstrated numerically as inaccurate by Marx & Blanc-Benon (2005*a*). It is generally agreed that this equation and its modified form from Atchley et al. (1990, Equation 1) do indeed break down at DR <3%. But this outcome was published over 17 years ago, and it is argued here that the 'linear theory' in the sense of 1D propagation has certainly advanced from the early 1990s, to the point where it is now reliably and demonstrably accurate enough for the design of thermoacoustic devices operating up to a DR of 3%. Assumptions of a constant temperature gradient in the stack plate and zero heat conduction in the working fluid, have been shown as sources of error and have since been addressed. In the opinion of the author, the works of Arnott et al. (1991), Reid (1999), and the maturation of *DeltaE* (arguably in 2004), applied correctly and sensibly, have been shown to be effective for DR <3%.

Publications from the last 8 years that support this view include

- the dissertation of Poese (1998), in which he notes several discrepancies with data obtained from the 'Frankenfridge', a high powered variant of a Hofler-style thermoacoustic refrigerator (Hofler 1986) (however, he attributes these errors to the resonator calculation and not the stack);
- the dissertation of Reid (1999);
- the experimental study by Backhaus et al. (2004) which concludes "The agreement (between the experimental and numerical data in Figure 2) demonstrates

the quality of the numerical integration's ($DeltaE$) predictive power";

- the experimental works of Zhou & Matsubara (1998);
- Figures 5 to 7 presented by Backhaus & Swift (2001) for a DR of 3.8% which show excellent agreement even for a non-conventional stack construction; and
- the highly-regarded study of a travelling-wave system by Backhaus & Swift (2000), in particular Figures 11 and 12, which demonstrate excellent agreement between the predicted and experimental rates of acoustic power lost and delivered.

It is not suggested that the linear theory by itself is the solution to full characterisation of thermoacoustic devices below a DR of 3%, but the author considers that linear formulations executed correctly do provide results sufficiently accurate for design of thermoacoustic systems. Recent studies which indicate that linear models have insufficient accuracy often use single-equation approaches to the calculation of experimental temperature differences. For example, Piccolo & Cannistraro (2002) applied the same steady state temperature difference formulation from Wheatley et al. (1983) and also used by Atchley et al. (1990). It is of no surprise then that they consequently presented similar levels of error at low amplitudes to the study of Atchley et al. presented twelve years earlier.

2.2.3 Modifications to the linear model

Swift (2002, Chapter 7) acknowledges that advancement of prediction tools for thermoacoustic devices from the 'standard' linear theory of Rott (1980) has been driven by the increased desire to quantify prediction errors at high pressure amplitudes. Tortuous flow paths, turbulence, entrance and exit conditions, mass streaming and harmonics are discussed as sources of prediction error which might be accounted for through modification of the standard linear formulations. Swift

(2002, p155) describes this approach as a way to "... build upon and extend Rott's acoustic approximation, adding (one might say kludging) various phenomena onto it". He adds that a "strength" of this approach is that it builds upon a "firm foundation", perhaps inferring that the accuracy of the linear theory is already accurate to a useful degree.

Tortuosity in thermoacoustic stacks and regenerators is encountered with the use of mesh screens or reticulated wires as elements in the stacks and regenerators. Assuming that instantaneous heat transfer and viscous loss mechanisms are independent of flow history, or in other words, are evaluated at pseudo-steady-state, gas flow through the stack is considered reasonably constant at each small time period of interest, and provided that the distance travelled by gas particles in the specified time period is much less than the gas displacement amplitude, then steady-state experimental data may be used to estimate the performance of the stack. The condition for this approach is expressed by Swift (2002, p157) in terms of the hydraulic radius

$$r_h \ll \delta_\upsilon \sqrt{|N_{R,1}|} \tag{2.17}$$

with the complex Reynolds number defined as (Swift 2002, Equation 7.12)

$$N_{R,1} = \frac{4\,|U_1|\,r_h \rho_m}{\phi A \mu} \tag{2.18}$$

where ϕ represents the porosity of the stack, or proportion of 'open' volume (occupied by the gas) within the stack.

Turbulence is accounted for using the same assumption and estimation of the Moody friction factor f_M (Swift 2002, Equation 7.21)

$$\Delta p = f_M \frac{L}{D} \frac{1}{2} \rho \langle u \rangle^2 \tag{2.19}$$

where $\langle u \rangle$ is the average fluid velocity, in conjunction with estimation of $N_{R,1}$ and wall roughness, where L and D are the length and internal diameter of the pipe section respectively. To predict the performance of a thermoacoustic refrigerator at drive ratios between 0.5% and 6%, Poese & Garrett (2000) used *DeltaE* with and without the turbulence model activated. With reasonably low error in prediction of the input acoustic power and cooling power, the effect of 'modifying' the linear theory to account for turbulence was demonstrably beneficial, but was only achieved with "outrageously" (many orders of magnitude) higher values of wall roughness than that expected in realised devices.

Entrance effects for stacks are not yet directly accounted for in modified linear formulations, although the experimental study of Smith & Swift (2003) indicates that minor losses in oscillatory flow through a sudden area change are not expected to be as high as that in steady flow conditions. In a similar method used by Wakeland & Keolian (2002*a*), an estimate of minor losses were calculated using a linear formulation based upon prediction of the velocity profile and coefficients for kinetic energy and momentum.

2.3 Beyond first-order analyses

First-order prediction methods are without doubt important to the current design and development of thermoacoustic devices since they allow relatively quick performance estimations within a design phase. Unlike first-order models which have been developed to the point where power and efficiency can be computed with useful accuracy (albeit for low amplitude operation), higher-order considerations of entire thermoacoustic systems currently cannot be evaluated cost-effectively due to ex-

cessive computational costs. As a result, higher-order numerical analyses have so far considered models of reduced dimension and a small region of a thermoacoustic device (i.e. focussing on just one or two stack plates).

2.3.1 Higher order heat and flow transportation models

Whilst Rott's approximation is an acoustic approximation, Tominaga (1995) instead proposed a formulation rooted in thermodynamic theory, whereby the two-dimensional Navier-Stokes equations were linearized, stripped of viscous terms and simplified for steady-state operation. Oscillatory time dependence of complex state variables was achieved using the representation $e^{j\omega t}$, where $j = \sqrt{-1}$. As with Swift's implementation of Rott's acoustic approximation, Tominaga's formulation is incapable of modelling non-linear, second-order effects which are considered important to the modelling of thermoacoustic systems operating at drive ratios in excess of 3%.

Worlikar & Knio (1996) used a two-dimensional formulation similar to that used by Tominaga (1995), to model the unsteady flow of the working gas in the vicinity of the thermoacoustic stack plates. Various plate thicknesses were investigated and in each case were modelled as rectangular in cross section. The 'streamfunction' distribution (which here could be used as an approximate vorticity field distribution) calculated by Worlikar & Knio (1996, Fig. 3) for a drive ratio DR of 0.2% is shown in Figure 2.5. The figure shows that the generation of vortices at each edge of the stack plates due to the gas oscillations is not only symmetric about the midplane of the stacks but also about the midlength of the plates over a full oscillation. In Figure 2.5, the diagrams which are 180° apart in phase (such as 2.5(a) and 2.5(e)) are mirror images about the midlength of the stack plates. It is likely that this would not be the case if the computational domain was extended to the full cross-sectional area of the thermoacoustic device, and accounted for

transitions or blockages upstream or downstream of the stack.

Figure 2.5:

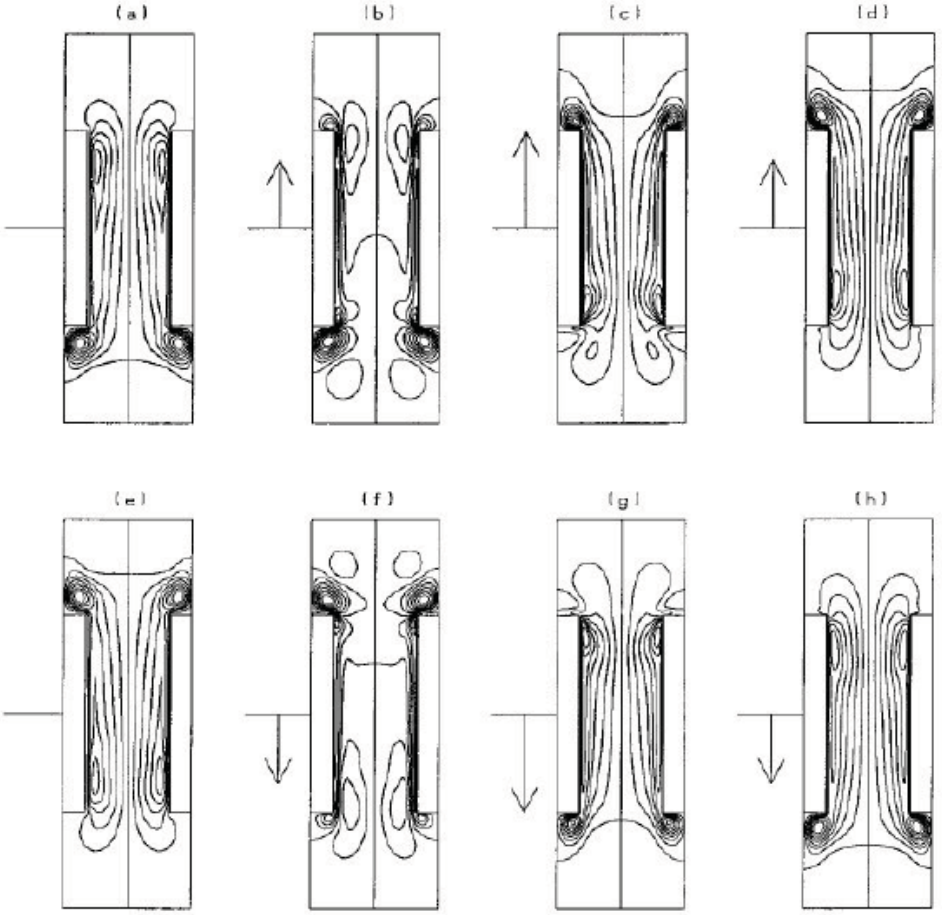

Diagram showing the evolution of the 'streamfunction' distribution, reproduced from Worlikar & Knio (1996, Fig. 3). Time interval between each figure is 45◦ shown with reference to the acoustic velocity (arrows to left of each diagram). © Elsevier Limited.

"Reprinted from *Journal of Computational Physics*, vol. 127 (2), Worlikar, A. S. & Knio, O. M., Numerical simulation of a thermoacoustic refrigerator. I. Unsteady adiabatic flow around the stack, pp. 424-451, Copyright (1996), with permission from Elsevier."

Further to this, Worlikar & Knio (1996) do not account for variations in viscosity or thermal conductivity with temperature, the spacing between plates ($2y_0$) or drive ratios above 1%. However in a follow-up article by the same authors (Worlikar et al. 1998), consideration of the drive ratio was extended to 2%, in addition to approximations regarding thermal conduction in the stack plates.

Following the results of Cao et al. (1996), which indicated that the time-averaged transverse heat flux distribution in thermoacoustic stacks is effectively non-linear,

Mozurkewich (1998*a*,*b*) used a one-dimensional representation for heat transfer in parallel stacks and heat exchangers. His study considered the stack to be thermally isolated, in that heat could only be transferred to the adjacent fluid within the stack, and this forced the transfer of heat from the stack to an adjacent heat exchanger to occur via the oscillating fluid and not via direct conduction. This requirement also forced an opposing transverse heat flux differential between the stack plate ends, as heat deposited into one end was forced to leave at the other. This approach was also used by Piccolo & Pistone (2006) to calculate a time-averaged transverse heat-flux distribution which showed excellent agreement with the numerically derived results of Cao et al. (1996) and Ishikawa & Mee (2002).

Despite effectively enabling calculation of non-linear stack temperature distributions, which compared well with published numerical results (Cao et al. 1996), the boundary-value model of Mozurkewich (1998*a*) still largely follows the short-stack boundary layer analysis of previous studies (Swift 1988) which do not account for higher-order effects such as flow entrance or exit effects through the stack, flow separation and flow recirculation. Nonetheless, it was an improvement to conventional linear theory. Mozurkewich noted that the 'standard' linear model of thermoacoustics, which refers to the approximations developed by (Rott 1980) and later (Swift 1988, 2002), did not correctly predict the concentration of heat flux at the stack ends because it considers time-averaged temperature profiles between the fluid and stack wall to be equal (Mozurkewich 1998*b*, p380):

> *"The standard theory of thermoacoustics assumes (a) that the time-averaged temperature of the fluid across any cross section of a pore is equal to the time-averaged temperature of the adjacent pore walls and (b) that the acoustic displacement amplitude is negligible compared to the length of the stack ... both assumptions are suitable well inside the stack but fail near its ends ... (this consideration) has been demonstrated*

explicitly in a recent numerical computation."

Indeed, Cao et al. (1996) and later Ishikawa & Mee (2002), using higher-order numerical models, found indications that heat transfer is concentrated at the stack ends in a thermoacoustic device.

There exists various non-linear computational tools that have been developed for Stirling engines which may also be applied to thermoacoustic phenomena. Examples of these programs are the CFD code *CAST* (Computer Aided Simulation of Turbulent Flows), which was modified by Ibrahim et al. (2001) to model the Stirling engine of Kornhauser & Smith (1989). *CAST* allows two-dimensional simulation of enclosed compressible fluids, and employs the solution of compressible Navier-Stokes equations with turbulence modelling. Ibrahim et al. found that additional data was required for validation of *CAST* as an effective numerical tool.

2.3.1.1 The thermoacoustic couple

Ishikawa & Mee (2002) used full two-dimensional Navier-Stokes equations to model the heat transport effects in what is referred to as a 'thermoacoustic couple' (Wheatley et al. 1983). Thermoacoustic couples are best described as a short stack (with length the same or less than the acoustic wavelength) consisting of only a few parallel plates which can be placed at any position inside the resonator. Figure 2.6 presents several examples of computational domains used to model thermoacoustic couples. To date, all computational domains used to model a thermoacoustic couple are two-dimensional and consider only one plate or a single channel between two plates. Although the range of thermoacoustic stacks used in practice are varied in shape and configuration, ranging from uniform rectangular cell types, to spiral wound designs, and random stacks of mesh, parallel plate arrangements are geometrically the simplest and appealing for those looking to minimise computational costs and yet build upon previous experimental studies.

There are many numerical and analytical studies of porous media in thermoacoustic devices (Jin et al. 2003, Mahmud & Fraser 2005, Lycklama à Nijeholt et al. 2005, Liang & de Waele 2007, Zhang et al. 2007) however it is argued that the results of these studies cannot be directly applied to thermoacoustic couples or stacks comprised of parallel plates, because of the physical differences between porous media and fabricated parallel plate configurations.

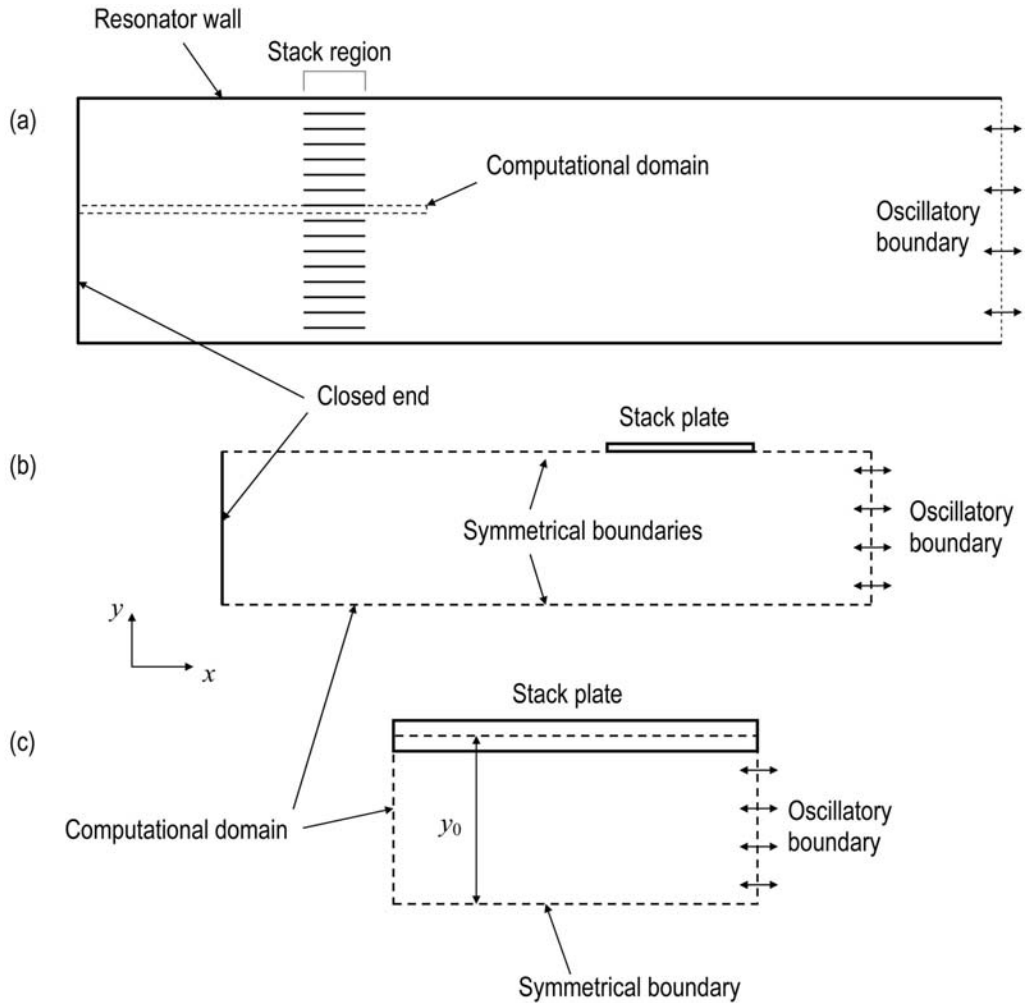

Figure 2.6: Computational domains (boundaries indicated by broken line) used by (a), (b) Ishikawa & Mee (2002, Figure 1) and (c) Piccolo & Pistone (2006).

In 2002, Ishikawa & Mee (2002) claimed Cao et al. (1996) as the only group to have simulated isothermal plates in a standing-wave using the full two-dimensional

Navier-Stokes equations at that time. This does not appear to be completely accurate: although Besnoin (2001) in his PhD dissertation did describe use of a reduced set of Navier-Stokes equations in his initial studies, when later considering "geometrical parameters" he claims to have used "the full (Navier Stokes) model" in which "the thickness of the stack is directly accounted for". The results presented by Besnoin are discussed further in Section 2.3.3.

One method of reducing the computational cost in numerically modelling thermoacoustic couples is to apply an isothermal boundary condition to the stack plate. Applying an isothermal stack plate condition reduces the computational effort through ignorance of conduction in the solid stack material and the fluid-side heat transfer coefficient. However, it also prevents the establishment of temperature gradients, which could readily show the performance of a thermoacoustic device. The relative performance of various thermoacoustic couples can still be evaluated on the basis of heat flux rate and distribution through the plate surface.

2.3.1.2 The thin plate limit case

Cao et al. (1996) modelled a small 'half-spacing' between plates of a thermocouple, in that the solution boundary extended in two dimensions from the centreline of one plate upstream of the thermocouple to a point downstream and midway between the plates. This is effectively the same computational domain later used by Ishikawa & Mee (2002) shown in Figures 2.6(a) and 2.6(b). While their analyses incorporated the compressible two-dimensional Navier-Stokes equations, they did not model the acoustic impedance offered by the plates, nor evaluate in detail the effect of plate thickness upon the results. The travelling-wave component incident on the plate edges was modelled as a simple sine wave, and the computations used were acknowledged to be applicable only to plates of negligible thickness or a half-thickness of order $0.026y_0$.

Like Cao et al. (1996), Ishikawa & Mee (2002) found that the heat flux in thermoacoustic stacks was concentrated at the edges of the stack, and that a time-averaged non-zero velocity profile existed for particles located within a quarter of the inter-plate spacing (i.e. $0.5y_0$) from the plate edges. They suggest these effects to be part of a large scale, low frequency vortex just outside the plate edges. However, Ishikawa & Mee note that their computational domain is unable to fully model this phenomenon or account for acoustic streaming at the walls, since their model only considers a small region between the stack plates from a two-dimensional cross-sectional viewpoint (Figure 2.6) in following the work of Cao et al. (1996).

Although thermoacoustic couples with zero plate thickness (such as that modelled by Ishikawa & Mee) offer some insight into thermoacoustic heat transport mechanisms, they do not represent the flow impedance resulting from physical implementation of a parallel plate stack, let alone other stack configurations such as pin array or rectangular pore stacks. Furthermore, despite the work of Ishikawa & Mee (2002) being a significant extension of the work of Cao et al. (1996), there is still no directly comparable experimental data to support the simulation results of either research group.

Schneider et al. (1999) applied a finite-volume method to numerically evaluate the time-averaged heat flux through heat exchanger plates placed in parallel to the stack plate for arbitrary flow conditions. The heat exchanger and stack plates were of zero thickness, and insufficient results were presented to enable comparison with previous experimental or numerical studies. Other important aspects of relevance to practical applications, such as significant Mach number flows, variations in plate-spacing and variations in thermal and viscous penetration depths were not

considered.

2.3.1.3 Time-averaged heat flux

Piccolo & Pistone (2006) expanded on the work of Ishikawa & Mee (2002) and Mozurkewich (2001) by evaluating the transverse heat flux distribution in a thermoacoustic couple, using linear 'short-stack' thermoacoustic approximations modified by energy conservation considerations within the stack region. Their model is shown in Figure 2.6(c), where only the fluid within the stack region was considered, and the computational domain extended horizontally from plate end to end and vertically from the plate mid-section to the plate mid-spacing. As the 'short stack' analysis assumes that the plate length is much shorter than the acoustic wavelength and the presence of the plate is not a disturbance to the acoustic field, the transverse pressure and velocity distribution was considered by Piccolo & Pistone (2006) to be constant and unperturbed by the flow constriction between the stack plates. Velocity amplitudes through the stack region were prescribed from a continuous volume velocity condition and the stack blockage ratio. Density was also considered constant. The plate was also considered to be thermally 'isolated' at each end, in that axial heat transfer between the stack and fluid at each vertical edge was prevented, and the transverse heat flux integral over the plate surface was zero. In effect, any heat transferred through the plate surface at one end of the plate was considered to be returned at the other end, and this thermal conduction within the plate was modelled using a solid thermal conductivity value of k_s=10W/mK.

The time-averaged transverse heat flux determined from Run 1 of Piccolo & Pistone (2006) showed good agreement with that presented from Run 2 of Cao et al. (1996) and Run 7 of Ishikawa & Mee (2002). All three runs solved a case with near-identical stack location and geometry using helium at a mean pressure

of p_m=10kPa, an operating frequency of f=100Hz and a relatively low drive ratio of DR=1.7%. However, all three studies used a different computational domain: the domain considered by Cao et al. extended past each end of the stack plates; Ishikawa & Mee extended the model to left-side end wall (Figure 2.6(b)), and the fluid region modelled by Piccolo & Pistone was limited to the stack plate region (Figure 2.6(c)). Regardless of the difference in solution domains, the agreement in results was expected, since in all three studies the stack plates were considered to be of zero-thickness and the local flow conditions at the plate surface were effectively the same.

2.3.1.4 Comparisons with experimental data

Both the publications of Yuan et al. (1997) and Watanabe et al. (1997) described models capable of incorporating non-linear processes. Ishikawa & Mee (2002) commented that in these previous papers simplifications were made to the governing equations; both Yuan et al. (1997) and Watanabe et al. (1997) used approximated terms which governed the important energy exchange behaviour between the fluid and the stack, and did not consider axial heat conduction in the stack. Also, both approaches were only one-dimensional and were not applied to refrigerators. Despite not accounting for axial heat conduction in the stack, the results from the numerical models presented by Yuan et al. and Watanabe et al. compared reasonably well with previously reported experimental data. Watanabe et al. comments that whilst the results from their model were in "very good agreement" with previous experimental data (Atchley et al. 1990), consideration of heat conduction within the stack is still desirable for future studies.

Matveev (2003) developed an interesting non-linear model for a Rijke tube, in which the total power output is assumed to be proportional to the input with a non-linear coefficient largely dependent on the oscillatory pressure amplitude.

Matveev himself acknowledges that the resultant system of equations is not justified by an underlying physics relation, and as a result it seems that the experimental data and model, for many aspects discussed in the paper, do not correlate well. Whilst this consideration of non-linear effects in a thermoacoustic device is notable for the purposes of this review, Matveev's findings are not applicable to a thermoacoustic refrigerator, in which the system components and their arrangement are significantly different to a Rijke tube (e.g. closed ends, standing-wave operation, presence of stacks and heat exchangers, significant cooling effects etc.).

Like the study of Matveev (2003), the findings of Hantschk & Vortmeyer (2000) regarding their simulations of a Rijke tube using linear Navier-Stokes equations, are not directly applicable to the current study. However, the method used by Hantschk & Vortmeyer is notable because they compared experimental data such as the operating frequency, mean flow velocity and limit cycle amplitude to numerical model estimates. Hantschk & Vortmeyer note that an advantage of a non-linear model over linear approximations is that inclusion of dissipative, performance limiting effects result in the ability to estimate the limit cycle conditions. In the case of the Rijke tube, Hantschk & Vortmeyer were able to predict the maximum acoustic pressure amplitude to within 1dB re 20μPa, which represents a very good prediction accuracy for acoustic phenomena.

2.3.2 Thermal distortion effects

'Temperature distortion' is a significant non-linear effect that has been observed using a numerical basis by Marx & Blanc-Benon (2004*b*) at drive ratios above 3%. Within the stack region, they predicted that with increasing Mach number, the ratio of oscillating gas temperature to ambient temperature reaches a 'pseudo saturation' point and the temperature temporal waveforms become more distorted and inharmonic. Marx & Blanc-Benon argue that because the temporal variations at a point

distant from the stack did not distort with higher Mach number flows, the effect must result from interaction with the stack plates and not nonlinear acoustic effects.

The model used by Marx & Blanc-Benon (2004*b*) was similar to that of Ishikawa & Mee (2002) in that the computational domain was one half plate-spacing wide and extended beyond an isothermal, zero-thickness plate to a hard reflective end. However, their model also included hot and cold heat exchanger plates which were separated from the stack plate. Their model used air at a mean pressure of 100kPa, which prevents any immediate comparison with the Ishikawa & Mee model which used helium at 10kPa. The Marx & Blanc-Benon (2004*b*) model also used an operating frequency of 20kHz, far higher than the 100Hz used by Ishikawa & Mee in 2002.

A later study by Marx & Blanc-Benon (2005*b*) utilised a revised computational domain which is simpler and closer to that used by Ishikawa & Mee (2002). The two heat exchanger plates considered in their 2004 work were omitted and the length of the stack plate was set to $\lambda/40$, as per the majority of the test cases considered by Ishikawa & Mee. Regardless, in this study Marx & Blanc-Benon investigate a nonlinear thermoacoustic effect not presented by Ishikawa & Mee (2002) or Cao et al. (1996). Marx & Blanc-Benon (2005*b*) conclude that temperature distortion effects are most likely to occur throughout stack regions located near velocity antinode(s), for high drive ratios, and with stack lengths less than four particle displacements long.

With sufficient cause to believe that high-drive-ratio induced temperature distortions could explain the significant inaccuracies of linear thermoacoustic theory for pressure amplitudes above 1% mean pressure, Marx & Blanc-Benon (2005*a*) used the numerical model from then-recent work (Marx & Blanc-Benon 2005*b*) to offer comparisons in prediction accuracy with conventional, linear models

developed from over twenty years of quantitative thermoacoustic research (Rott 1980, Swift 1988). The numerical model used (Marx & Blanc-Benon 2005*b*) employed two-dimensional compressible Navier-Stokes equations with consideration of mass and energy conservation equations to account for non-linear effects. The comparison found that whilst non-linear effects could explain discrepancies between the linear and numerical models at high drive ratios or flowrates, temperature distortion effects were present for all flow ranges of interest.

Conventional linear formulations for stacks assume a constant temperature gradient in the direction of gas oscillation, whereas the non-linear numerical model results presented by Marx & Blanc-Benon (2005*a*) showed a tapering effect at the stack ends. Although the temperature gradient in the stack was essentially the same between each model, the tapering effect meant that the linear model predicted an overall stack end temperature difference greater than the non-linear numerical model. Linear models also assume the stack and adjoining gas temperature gradients to be equal, however Marx & Blanc-Benon (2005*a*) argue that because of the greater heat transfer at each end of the stack, this assumption is not correct. To account for these differences, Marx & Blanc-Benon proposed correction terms to account for such temperature effects, however it is noted that these correction terms are offered in the absence of experimental findings.

With suitable correction terms in place, Marx & Blanc-Benon (2005*a*) indicated that discrepancies in predicted stack end temperature difference between the numerical and linear models are minimised for Mach numbers up to 4%, at which point non-linear effects are calculated to be significant. However, in the absence of experimental data, it is unknown what the true temperature difference would be for the case considered by Marx & Blanc-Benon (2005*a*). For example, flow vortices and eddy losses from high Mach number oscillatory flow over the stack ends would serve

to further reduce the actual temperature difference across the stack. Furthermore, whilst there is no reason at this stage to dispute the existence of thermal distortion in thermoacoustic stacks, the conclusion reached by Marx & Blanc-Benon that thermal distortion at high drive ratios only occurs in the stack regions should be treated cautiously until experimental data confirms this.

2.3.3 Flow fields and acoustic streaming

Whilst first-order linear theories are useful for basic investigative studies, they are not necessarily able to account for non-linear phenomena. This limitation of linear theories has led to increased study of second-order flow effects in thermoacoustic systems. There are many studies of second-order flow effects in fields of general fluid dynamics problems, but relatively few for thermoacoustic applications. Previous studies that investigated acoustic streaming within thermoacoustic systems predominantly used a numerical approach and investigated the flow effects for an oscillating fluid inside parallel or periodic pores. A form of acoustic streaming termed 'Rayleigh streaming' is described by Bailliet et al. (2001) as a "vortex-like" streaming (non-zero mean velocity) within the Stokes fluid boundary layer at the pipe and stack wall surfaces. For standing-wave devices where the mean gas flow-rate is zero, dissipative Rayleigh streaming at these fluid-solid interfaces has a significant effect upon the performance of thermoacoustic devices.

Bailliet et al. (2001) derived a series of analytical expressions for Rayleigh streaming effects in standing-wave devices, using a series of two-dimensional Navier-Stokes equations to evaluate the second-order components of pressure gradient, velocity and steady state mass-flux across a stack. While the work of Bailliet et al. is useful for estimating the magnitude of acoustic streaming for parallel plate stacks, analytical consideration of a variable cross-section as an acoustic streaming suppression measure would have been useful. Bailliet et al.

considered time-independent, steady-state operation *within* the stack; the effect of the blockages imposed by the stack wall thickness do not seem to be accounted for, and linear thermal gradients were assumed across the stack length (Bailliet et al. 2001).

Hamilton et al. (2003) comments that because the work of Bailliet et al. used a Eulerian streaming velocity, it did not fully provide for local mass transportation effects which Hamilton et al. considered important. Further to the work of Bailliet et al., Hamilton et al. developed a linear analytical model for the average mass transport velocity generated in a standing-wave resonator. The study considered a rectangular cross-section in two dimensions. An earlier numerical model such as that produced by Mohd-Ghazali & McHugh (2003) based on a finite-difference methodology was able to derive a similar result.

Marx & Blanc-Benon (2004*a*) used a computational domain identical to that used by Cao et al. (1996) and Ishikawa & Mee (2002) in that they examined a two dimensional half plate-spacing 'slice' extending to the rigid termination of a loudspeaker-driven thermoacoustic refrigerator, and did not account for plate thickness. Marx & Blanc-Benon (2004*a*) also use the compressible two dimensional Navier-Stokes equations in their computation of the velocity field. They computed the mean second-order velocity field, using a fourth-order Runge-Kutta method for time integration and a fourth-order finite-difference method for spatial derivatives. As per the numerical study of Ishikawa & Mee, the computational domain of Marx & Blanc-Benon (2004*a*) does not investigate the effect of acoustic streaming at the walls of the resonator, which may be significant in comparison to recirculation zones closer to the stack edges.

The works of Besnoin (2001) and Blanc-Benon et al. (2003) are perhaps the

most insightful of the literature reviewed here, since they directly compare graphical outputs from both experimental and computational investigations. Both Besnoin and Blanc-Benon et al. compared particle image velocimetry (PIV) measurements with low Mach number flow computational results, for a small region at one end of a thermoacoustic stack. As is evident in Figure 2.7, Blanc-Benon et al. (2003) demonstrated good agreement in flow structure between experimental and computational estimates.

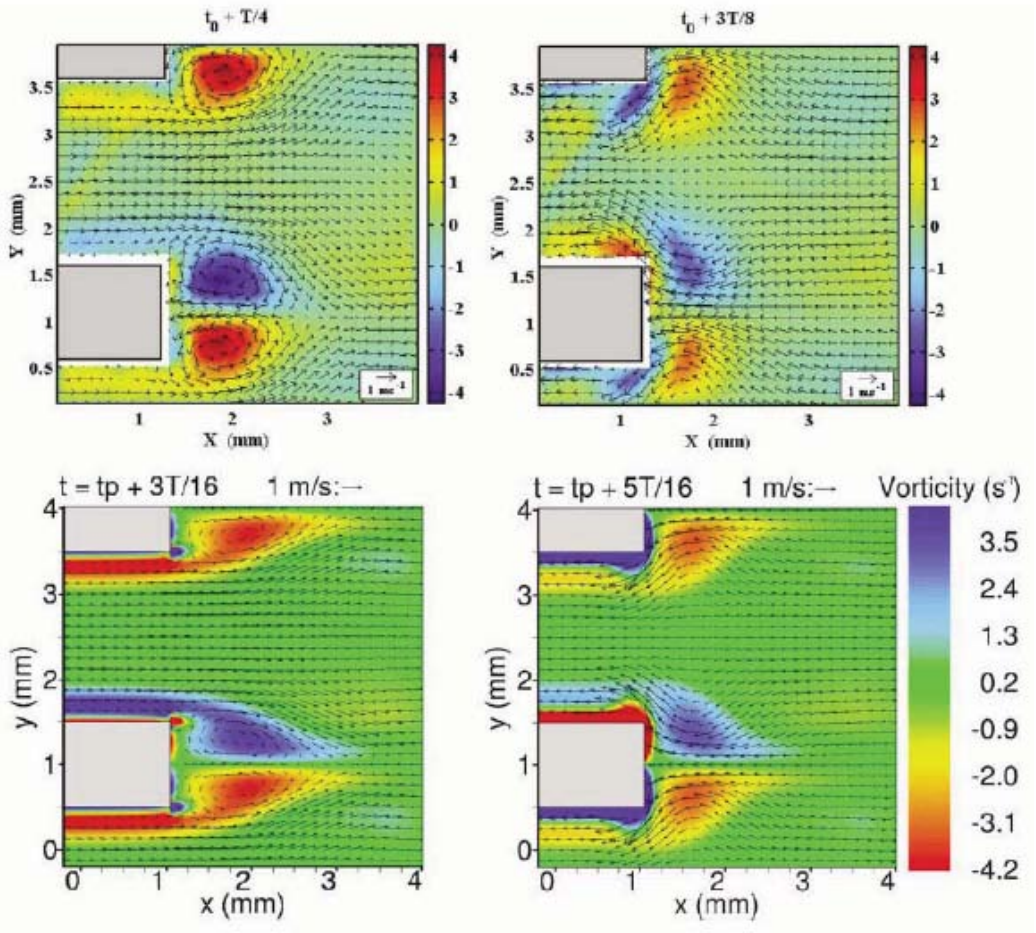

Figure 2.7: Experimental PIV (top row) and numerically predicted (bottom row) results of instantaneous velocity vectors and vorticity contours at selected timeframes at the cold end of a thermoacoustic stack (Reproduced with permission from Blanc-Benon et al. (2003, p22)). ©Comptes rendus Mécanique.

Although the experimental work of Blanc-Benon et al. (2003) does not extend to significant thermoacoustic effects such as those in pressurised, circular devices which

are designed for effective cooling performance, it does give confidence in the use of computational methods for investigations of flow structure around thermoacoustic stacks and heat exchangers. The design of highly efficient thermoacoustic stacks may indeed one day require computational tools to minimise adverse flow structures such as those shown in Figure 2.7.

The dissertation of Besnoin (2001) contained a comparison between his computational predictions and experimental PIV measurements (Duffourd 2001). The major finding from the comparison was that the edges of the stack plates were confirmed as critical to the performance of the stack. Besnoin concluded that

> *"around the stack corners, flow and heat transfer processes are dominated by edge effects and multidimensional phenomena."*

It should be acknowledged that his study considered the gas to have constant viscosity and thermal conductivity, and used a spatial discretisation scheme significantly coarser than that used by Ishikawa & Mee (2002) or the present study.

The dissertation of Aktas (2004) reported both numerical and experimental studies of streaming within thermoacoustic devices, however neither study is considered directly applicable to the current work. The numerical model used by Aktas (Aktas et al. 2004, Aktas 2004) for thermoacoustic streaming within enclosed regions used impulsive or rapidly increasing thermal inputs to a computational domain otherwise at ambient conditions. Such simulation conditions are not representative of experimental thermoacoustic systems since the resultant pressure response is a single pressure wave or pulse, as opposed to a continuous oscillatory pressure field. Also the experimental study investigated Rayleigh streaming for a standing-wave resonator using atmospheric air, and the resonator was stackless and without heat exchangers or other flow blockages typical of practical thermoacoustic systems. The qualitative acoustic mass streaming results presented in the

experimental study are acknowledged to describe Rayleigh streaming (Swift 2002, Chapter 7), observed previously elsewhere for oscillatory flows.

The numerical study of Lycklama à Nijeholt et al. (2005) is unique in that it considers the full length of an entire travelling-wave thermoacoustic heat-engine using a two-dimensional computational domain and employs solution of unsteady Navier-Stokes formulations. Lycklama à Nijeholt et al. used an axisymmetric computational domain which extended the entire axial length of an enclosed double Helmholtz resonator. The engine section was modelled as a porous zone inside a pipe concentrically aligned and within a larger circular pipe, to form an annular feedback loop for suitable acoustic phasing as a travelling wave heat-engine. In using a relatively low mesh density and modelling the stack and heat exchangers as porous elements, streaming within the stack region was not evident. However, flow separation and recirculation zones were evident downstream of the stack region and near the feedback inertance which is modelled as a flat plate with rectangular edges. The authors also state that the numerical model captured time-averaged flow circulating through the feedback loop, also known as Gedeon streaming (Gedeon 1997). The study of Lycklama à Nijeholt et al. (2005) also presents time-averaged temperature distributions in the stack region, however it is difficult to provide comparison with other work since the heat-engine stack has a forced temperature gradient and zero solid heat conduction.

Galiullina et al. (2005) developed a two-dimensional numerical model using the commercial CFD code *Fluent* to simulate acoustic streaming in simple circular pipes and in a separate case, near three parallel plates representing a stack of 0.2mm thick and 20mm long. Although acoustic streaming was 'forced' to rapidly develop with a non-uniform velocity boundary condition, and it is not clear what drive ratio was modelled, qualitative results were stated to be in agreement with

an experimental result reproduced from the work of Ozawa et al. (1999). The impact of the acoustic streaming upon the rate or distribution of heat transfer was not discussed in this paper. In a later numerical study, Galiullina & Botteldooren (2006) considered a region including a stack of ten parallel plates, however did not model the plate thickness or the influence of drive ratio. Within the stack plate channels, acoustic streaming patterns were demonstrated to be similar to the analytical result of Hamilton et al. (2003).

So et al. (2006) discussed the effect of streaming within a stack or regenerator region, and stated that streaming is a mechanism for excessive energy dissipation and hence reduced efficiency. The instabilities which lead to streaming in thermo-acoustic refrigerators are believed to be driven by non-linear flow impedances of the stack plates and surrounding walls, but inhibited by thermal transport mechanisms in the stack region.

Yu et al. (2006*a*,*b*) used the commercial CFD code *Fluent* to study flow and temperature fields in travelling-wave thermoacoustic heat-engines using time-averaged thermal and acoustic metrics. Yu et al. found that Gedeon streaming was present in the travelling-wave loop, however, their study did not investigate standing-wave thermoacoustic couples or directly simulate stacks comprised only of parallel plates. The study of Zhang et al. (2007) utilised *Fluent* to study flow recirculation in an axisymmetric model of an orifice pulse tube refrigerator (OPTR) but also considered the stack region as a porous volume, instead of rigid stack plates. Zhang et al. found that flow recirculation through the stack region adversely affected the performance of the device and was undesirable.

The study of Berson & Blanc-Benon (2007) confirmed the presence of 'vortex' shedding in parallel plate stacks. Berson & Blanc-Benon present experimental PIV

results over a region spanning several stack plates in the transverse direction and from within the stack region to a point well outside the stack region in the direction of oscillation, for atmospheric air at pressure amplitudes up to 5kPa. Berson & Blanc-Benon note that whilst the recirculation zones which develop at the edges of the stack plates remain stable at a drive ratio DR of 1%, at a drive ratio of 5% 'vortices' are observed to detach from the plate edges. At this pressure amplitude well in excess of DR=3%, Berson & Blanc-Benon (2007) note that

> *"the flow is no longer periodic ... As the flow within the gap does not repeat from one acoustic period to another, the average heat transfer through the gap is no longer steady, and oscillation of the cooling load will occur at high driving amplitudes."*

Berson & Blanc-Benon (2007) do not quantify the impact of the flow instabilities upon the rate of heat transfer, however their study demonstrates the potential for acoustic streaming despite flow conditions being in the laminar regime.

2.3.4 Transient effects

The classical studies of Rott (1980) and later Swift (1988, 2002) have largely assumed steady-state operation for reasons of simplicity. However the available power for a heat-driven thermoacoustic refrigerator is typically transient or unsteady, and as a result, the operation of such a thermoacoustic system will be to some degree unsteady. This section will discuss prior research regarding unsteady operation of thermoacoustic devices.

In transient or unsteady thermoacoustics, a key term used is the 'limit state' or 'limit cycle', which refers to the state of operation or operating conditions in which the phase and magnitude of the state variables such as p, U and T do not vary from one oscillation to the next. At the limit cycle, the time-averaged change

in enthalpy and entropy flux is zero and the enthalpy flux becomes constant and uniform along the length of the device (Bauwens 1998). Limit-cycle simplifications used in Rott's approximations may not be capable of accurately predicting the performance of thermoacoustic systems in transient states, if the upper frequency of disturbance approaches the operating frequency of the thermoacoustic device.

Bauwens (1998) noted that due to the large differences in thermal inertia between the working gas and the solid wall structures, transient heat transfer effects could be modelled by evaluating the thermoacoustic and the thermal conduction processes in different timescales. For example, Bauwens observed that during operation, the temperature of a wall in contact with the oscillating gas changes much more slowly than that of the gas itself. To simplify the calculation on account of this observation, he developed a dual timescale approach, whereby the thermoacoustic oscillations were modelled using a 'fast' timescale τ, and the net heat transport effects due to these oscillations were calculated on a 'slow' timescale t.

Bauwens incorporated these two timescales into two-dimensional cylindrical-polar forms of coupled momentum, continuity, and energy equations, to model a smooth round closed tube driven at one end. Like Farouk et al. (2000), Bauwens (1998) also assumed that the Mach number, M, and the reference Prandtl number, σ_{ref}, would be such that $M^2/\sigma_{\text{ref}} \ll 1$. However, as discussed previously, the high velocity amplitudes typically associated with non-linear thermoacoustic effects in practical devices would lead to Mach numbers approaching 1.0.

In the model of Bauwens (1998), longitudinal conduction in the wall was neglected, and most notably, internal features such as stacks or heat exchangers were omitted. Applying boundary conditions similar to Farouk et al. (2000), (Bauwens 1998, Eqn. 26) reduced the set of equations representing the thermoacoustic system

to

$$\left(2+\frac{d}{r}\right)\left(\pi\int_0^1\frac{1}{T_0}dx\right)^2\frac{\partial T_0}{\partial t}= \frac{11}{48}\int_0^1\dot{m}^2d\tau\frac{\partial}{\partial t}\left(\frac{k_{\text{ref}}}{k(T_0)}\int_0^x\frac{1}{T_0}dx\left(\frac{\partial T_0}{\partial t}\int_0^x\frac{1}{T_0}dx+\frac{8}{11}\frac{\gamma-1}{\gamma}\right)\right) \quad (2.20)$$

where d is the wall thickness, r is the inside radius, k is the gas thermal conductivity, T_0 is the mean gas temperature, x is the axial co-ordinate, γ is the ratio of specific heats, and $\dot{m}$ is the periodic mass flow rate amplitude. Bauwens then discretised Equation (2.20) to numerically model the change in dimensionless temperature along the axis of the tube with respect to change in dimensionless time. Whilst his results indicated that the numerical solution indeed reached stable conditions consistent with his theory, it seems no thermoacoustic cooling effects were modelled in the work. In Equation (2.20), the consideration of stacks or localised heating or cooling gradients are not present, and the equation is provided here to show the complexity of even relatively simple non-linear models used to describe thermoacoustic systems.

Brown & Churchill (1999) used a finite-difference computational model of a thermoacoustic wave propagating between two parallel plates, at each end of a smooth round tube. Whilst their work is notable for implementing a numerical model to investigate transient thermoacoustic waveforms, their work did not consider standing-wave arrangements, stacks, heat exchangers or other conditions necessary for effective thermoacoustic cooling.

The largest challenge to numerically simulating thermoacoustic devices subject to transient external states is the computational expense in capturing the low-frequency transient effects whilst also modelling in detail the internal 'cycle to cycle' operation of the thermoacoustic device at its characteristic operating frequency.

Farouk et al. (2000) numerically modelled the propagation of thermoacoustic

waves in a small two dimensional enclosure ($1mm^2$ square). The formulation used by Farouk et al. was based upon the compressible two dimensional Navier-Stokes equations in vector form, and discretised using a finite-volume method referred to as LCPFCT (Boris et al. 1993). For the scenario in which the fluid is modelled initially 'at rest', impulsive heat inputs and exponential heat inputs were modelled to compare their effect on the resultant pressure waveforms and temperature distributions. Although the model used by Farouk et al. was largely non-dimensional, the small model did not investigate the effect of varying cross-section and flow impedances formed by the thermoacoustic componentry. That is, the enclosure considered by Farouk et al. did not model the effect of flow impedances or thermoacoustic interactions at the surfaces of stack plates.

Rivera-Alvarez & Chejne (2004) used a non-linear model of a simple half-wavelength thermoacoustic engine to model what they describe as non-linear phenomena in a thermoacoustic device. Existing models such as the one used by Ward & Swift (2001) are based upon Rott's linear equations for thermoacoustic devices. Rivera-Alvarez & Chejne comment that this first-order model is limited in its use since it does not sufficiently include the effects of harmonics generation, high pressure amplitudes or transient behaviour (Rivera-Alvarez & Chejne 2004).

To address these limitations, Rivera-Alvarez & Chejne used coupled mass, momentum and energy balance equations for an ideal gas, and applied spatial Fourier series transformations to satisfy appropriate boundary conditions for a half-wavelength thermoacoustic engine. To find the 'limit cycle' of the thermoacoustic device, that is, the operating conditions at which the phase and magnitude of the state variables do not vary, Rivera-Alvarez & Chejne (2004, Equation 11) proposed the identity

$$d^2 = (\acute{T}_f - \acute{T}_0)^2 + (\acute{u}_f - \acute{u}_0)^2 \tag{2.21}$$

where $\acute{T}_f$ is the oscillatory (perturbed) temperature one period of oscillation in time after that of $\acute{T}_0$, and likewise for the oscillatory acoustic velocity $\acute{u}$. Note that the expression for d^2 does not include terms for the acoustic pressure, which has been arbitrarily set to zero. Rivera-Alvarez & Chejne use an iterative 'shooting method' to identify the conditions under which d^2 is zero, presumed to be the point of limit cycle operation (Rivera-Alvarez & Chejne 2004). However, the authors do not investigate non-linear phenomena such as second-order mode contributions and viscous streaming, and do not provide experimental data to validate their prediction technique.

2.4 Current gaps in knowledge

On this basis of this review, it is concluded that

- there is a lack of knowledge with regards to the understanding and modelling of the undesirable loss mechanisms in parallel plate stacks of thermoacoustic devices operating at drive ratios in excess of 3%;
- the influence of stack plate thickness upon the distribution of effective heat transfer and efficiency of a thermoacoustic couple at drive ratios in excess of 3% has not been fully investigated;
- there is a lack of knowledge with regards to the effectiveness and efficiency of thermoacoustic stack plates with non-rectangular edge shapes; and
- time-averaged gas flow (also referred to as 'DC flow' or 'acoustic streaming') within parallel-plate thermoacoustic stacks has not been fully investigated.

The first and second of these 'gaps' are addressed in Chapter 4. Chapters 5 and 6 seek to address the third and fourth 'gaps' respectively. Section 1.2 describes in detail the aims of this thesis and how they address each of these gaps.

Chapter 3

Methods for computational modelling of the flow disturbance effects in thermoacoustic couples

Whilst there are many publications demonstrating the usefulness of first-order prediction methods in the design and modelling of thermoacoustic devices (Swift 2002, Backhaus & Swift 2000, Gardner & Swift 2003), higher-order numerical models may assist in the understanding of various loss mechanisms during operation of these devices. Because of the intimate interaction between pressure, velocity, temperature and their derivatives, numerical modelling of thermoacoustic interactions require simultaneous conservation of momentum, continuity and energy of the working fluid and the surrounding solid structures in an unsteady formulation. The vast proportion of past numerical studies specific to thermoacoustic devices have used what Wheatley et al. (1983) has termed a thermoacoustic 'couple', which essentially consists of a single infinitely wide plate in an oscillatory flow field. The thermoacoustic couple is a two-dimensional approximation of a stack consisting of a series of parallel plates.

In modelling thermoacoustic couples, spatial and temporal scales must be selected to balance the resolution of the oscillatory flow structure with achieving limit state conditions within acceptable computational timeframes. Limit state operation is typically considered to be achieved when the changes in state variables are less than 0.1% when comparing two sucessive oscillations (Ishikawa & Mee 2002).

In Section 3.1, the modelspace used in this thesis is defined and the selection of appropriate numerical schemes will be discussed. Models developed specifically to investigate the applicability of solver settings, grid mesh sizings and solution timescales to maintain an acceptable level of model accuracy are presented and evaluated. Section 3.2 presents a discussion of error sources within the computational environment and the applicability of the numerical model to experimental data.

The numerical studies presented in this thesis were simulated using the commercial *Fluent* two-dimensional double-precision CFD environment. The techniques used to post-process the results obtained from the computational environment are presented in Appendix C.

3.1 System for modelling thermoacoustic couples of non-zero thickness

In expanding on the computational domain of Ishikawa & Mee (2002), Piccolo & Pistone (2006) and Cao et al. (1996), the modelspace used for the current work shown in Figure 3.1 is divided into six subdomains which together can facilitate changes to the fundamental characteristics of the thermoacoustic environment, such as the addition of plate thickness or a change in resonant frequency.

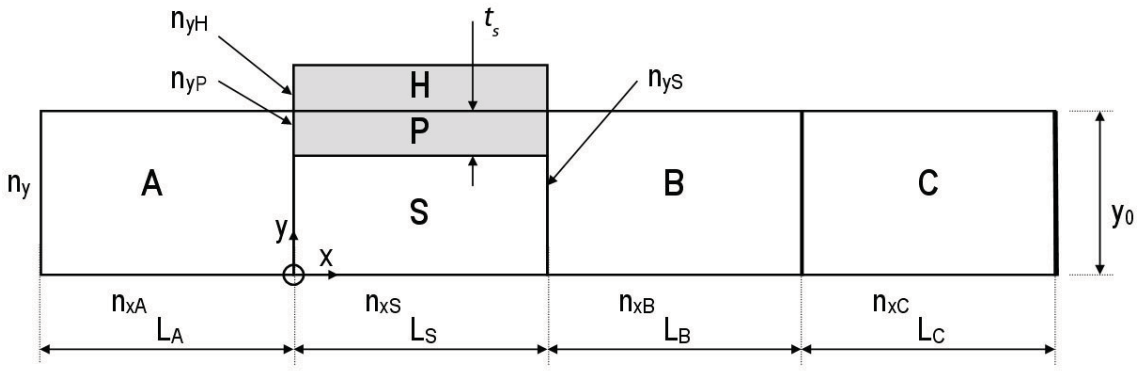

Figure 3.1: Annotated sketch of the thermoacoustic couple modelspace. Shaded areas are regions of solid material. Dimensions of axial length are denoted by L, transverse length scales by y. n_{xS} and n_{yS} describe the number of mesh subdivisions in the x and y directions respectively for domain S.

The plate and thermal reservoir comprises subdomains 'P' and 'H' respectively. Subdomain 'S' is the region bordered by the plate axially within the stack. The length y_0 is the half-spacing between plate centrelines. Subdomains 'A' and 'B' enable the modelling of flow structures which may develop outside the stack region due to non-zero plate half-thickness t_s, and are of sufficient lengths L_A and L_B such that the pressure changes can be considered adiabatic. Subdomain 'C' links subdomain 'B' to the hard walled end of the duct at the right edge of subdomain 'C'. Symmetric boundary conditions have been imposed on all lateral fluid boundaries. An oscillatory boundary condition on the left side of subdomain 'A' has been used to represent an oscillating pressure field.

Subdomain 'H' is important to the solution as it provides a thermal 'reservoir' to the model. Cao et al. (1996) and Ishikawa & Mee (2002) used the time-averaged heat transfer through a plate at fixed temperature to benchmark the performance of a thermoacoustic couple. However, Piccolo & Pistone (2006) demonstrated that similar results could also be obtained by including a finite heat capacity in the stack plate and forcing all heat fluxes to pass through the same boundary. In following Piccolo & Pistone (2006), the top and sides of subdomain 'H' are

thermally insulated, forcing any heat leaving the solid region to pass through subdomain 'P' into subdomains 'A', 'S' and 'B'. Whilst the thermal properties of the stack are therefore important because unsteady temperature distributions are allowed to form within the stack region, the thickness of subdomain 'H' is negligible compared to that of subdomain 'P'.

The effect of non-zero plate thickness can be accommodated by varying t_s, indicated as the vertical size of subdomain 'P'. The number of mesh divisions along each edge of the subdomains is indicated in Figure 3.1 as n, with the appropriate subscript describing the domain and x or y corresponding to the x or y axis. To preserve a consistent and rectangular computational mesh, n_{yP} is increased at the expense of n_{yS} such that n_y=n_{yP}+n_{yS}. This will be further expanded on in Chapter 4 which presents the results of a study that evaluates the effect of finite thickness t_s upon the performance of the thermoacoustic couple.

Note that Figure 3.1 shows the subdomain 'P' to have a rectangular shape which implies that the thermoacoustic couple has straight, rectangular edges. However, it is interesting to develop a greater understanding of the effects that arise from incorporating stack plate edges that are rounded or less restrictive to oscillatory flow entering the stack region. Chapter 5 presents a study using the system for modelling thermoacoustic couples shown in Figure 3.1 to investigate such effects. Different edge shapes are modelled by altering the shape of domain 'P' with subdomain 'S' expanded or reduced accordingly to ensure a continuous solution domain.

The applicability of the thermoacoustic couple model for the current work is summarised in the following sections, while Appendix B presents further details of several studies used to select appropriate grid mesh, timescale and solver settings within the computational environment.

3.2 Applicability of the thermoacoustic couple model

The system of modelling thermoacoustic couples presented in this chapter cannot completely represent a practical thermoacoustic device, but is believed to offer additional information compared to previous studies. In the absence of experimental data, the numerical estimates presented in this thesis are considered to provide the best guide available as to the flow and energy fields in thermoacoustic couples. The aim of the current work is to advance the model of the thermoacoustic couple to a point where it may yield useful insight into the performance of practical thermoacoustic refrigerators operating at high pressure amplitudes. This section will discuss the limitations of the numerical model and attempt to quantify error sources where possible.

The significant sources of error expected in simulations using the presented thermoacoustic couple model are outlined from a numerical viewpoint in Section 3.2.1. Section 3.2.2 discusses the difficulties and limitations to be expected when attempting to compare results from the presented numerical model to experimental results and to the design of practical thermoacoustic systems.

3.2.1 Numerical error sources

Ishikawa (2001, Section 4.3) states that the main sources of error in modelling thermoacoustic systems are

- discretisation of the governing equations,
- incomplete iterations or excessively high residuals (also known as convergence error or residual error),
- approximation of boundary conditions, and

- truncation and round-off errors, particularly in calculation of heat flux and other second-order variables.

In his error analysis, Ishikawa (2001) considered use of the commercial CFD code *PHOENICS* which used a single precision numerical basis. This means that by using double-precision values in the current work it is expected that the level of error associated with round-off will be lower than in the work by Ishikawa.

Section 3.2.1.1 discusses the errors expected in model implementation using the *Fluent* computational environment, and Section 3.2.1.2 presents the uncertainty of measurement of the results to be presented in Chapters 4, 5 and 6, due to aspects discussed in Appendices B.2, B.3, B.4 and Section 3.2.1.1.

3.2.1.1 Convergence (residual) errors

For all simulations, the two dimensional double precision ('2ddp') segregated solver environment was utilised, which enables changes to residual values of twelve orders of magnitude before round-off or truncation errors are expected. At time step N, *Fluent* normalises the residual of continuity, calculated as the sum of rate of mass creation within each individual cell, by dividing it by the maximum residual obtained after the first five iterations (*FLUENT 6.2.16 User Manual* 2006, Equation 26.19-6), i.e.

$$\bar{R}^c = \frac{R^c_{iteration}|_N}{\max(R^c_{iteration}|_{N\leq 5})}. \tag{3.1}$$

Residuals of general variables such as energy, x velocity and y velocity (represented by ϕ in the following) were scaled over all cells using (*FLUENT 6.2.16 User Manual* 2006, Equation 26.19-4)

$$\bar{R}^\phi = \frac{\Sigma_{cells}\,|\Sigma_{nb}a_{nb}\phi_{nb} + b - a\phi|}{\Sigma_{cells}\,|a\phi|} \tag{3.2}$$

where a is the centre coefficient value and b is the source term contribution for each cell, with subscript nb referring to influential neighbouring cells. The solver automatically advances the time step when scaled residuals are equal to or less than 10^{-6} for energy and 10^{-4} for all other variables. Figure 3.2 presents the screen output within the *Fluent* environment for the first five time steps of a simulation, showing that the reduction of each residual is reasonably stable. However, using these criteria alone does not guarantee an accurate solution. The *Fluent* documentation notes that there are two issues related to this method for establishing model convergence (*FLUENT 6.2.16 User Manual* 2006, Section 26.24.1):

> *"If you make a good initial guess of the flow field, the initial continuity residual may be very small leading to a large scaled residual for the continuity equation. In such a situation it is useful to examine the unscaled residual and compare it with an appropriate scale, such as the mass flow rate at the inlet. (Also) for some equations, such as for turbulence quantities, a poor initial guess may result in high scale factors. In such cases, scaled residuals will start low, increase as non-linear sources build up, and eventually decrease. It is therefore good practice to judge convergence not just from the value of the residual itself, but from its behavior."*

In developing suitable grid mesh profiles and solution control parameters, the change of each scaled residual with each iteration was observed and the integral of pressure, velocity and temperature over specific boundaries or zones within the model were monitored. The simulation was considered to have converged when each scaled residual was shown to exhibit a 'smooth' reduction behaviour and the integrated values of each state monitored were within a predicted or expected range using past studies, analytical calculations or first-order steady-state approximations as a guide.

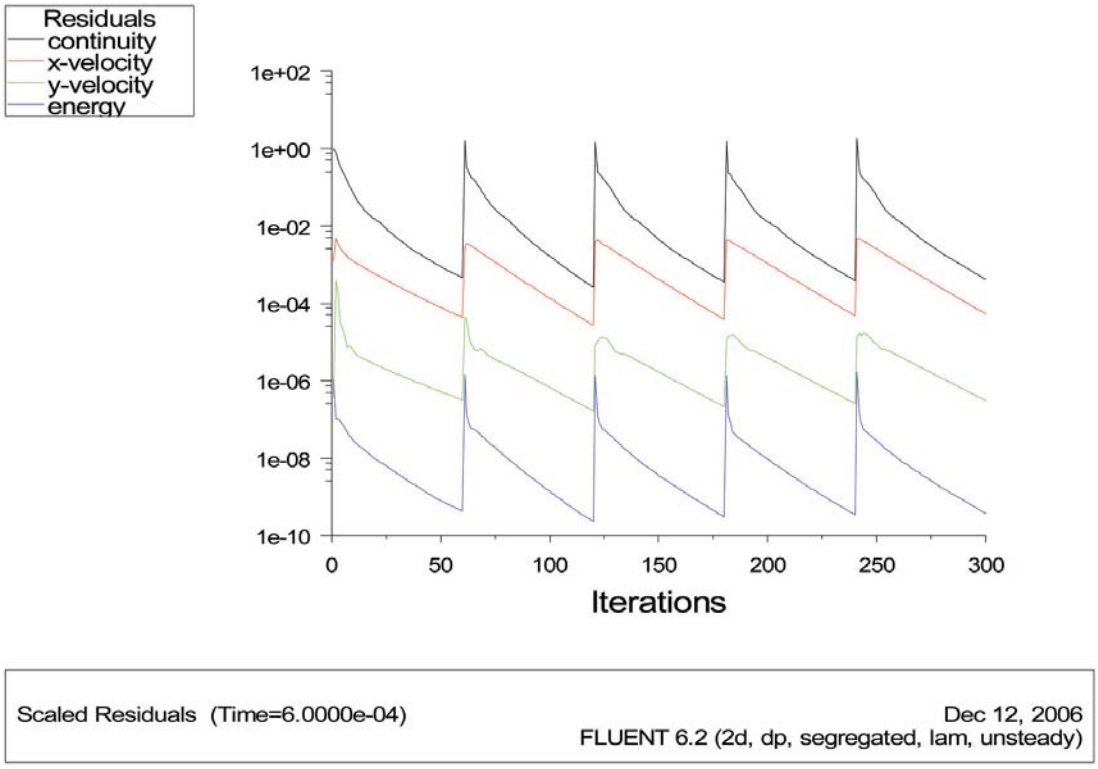

Figure 3.2: Fluent *6.2.16* typical screen output of scaled residuals over 5 time steps.

The computational error associated with convergence and state residuals was investigated using a model of a thermoacoustic couple with a high drive ratio and plate thickness (Case 'B' of Section B.3, a.k.a. Run 20 of Chapter 4). This model was repeatedly simulated from initialisation (t=0) until limit state (t=0.2s) using solver profile 'S2' (Section B.2), mesh sizing profile 'G3' (Section B.3) and timescale profile 'T0', a combination demonstrated to provide acceptable accuracy and stability given the context of this work.

Ten simulations of this model on ten individual computers running identical operating systems and hardware configurations were completed. Each case was run with an initial value for the axial velocity u randomly selected from the range 0 to 10m/s. At the solution time t=0.2s, the time-averaged gas temperature difference across the stack, $\Delta T_{k,hx}$, and time averaged rate of heat flux over the stack plate

surface, $\left\langle \dot{h}_S \right\rangle_t$, were calculated in order to determine the statistical uncertainty of measurement inherent in using *Fluent* on individual computers. The experimental standard deviation of the mean (ESDM) is defined as (Cook 1999, Section 4)

$$ESDM = \frac{\text{Standard deviation of } x}{\sqrt{n}} = \sqrt{\frac{\sum_1^{i=n}(x_i - \bar{x})^2}{n-1}} / \sqrt{n} \qquad (3.3)$$

where x is the individual measurement and $\bar{x}$ is the mean value of n measurements taken.

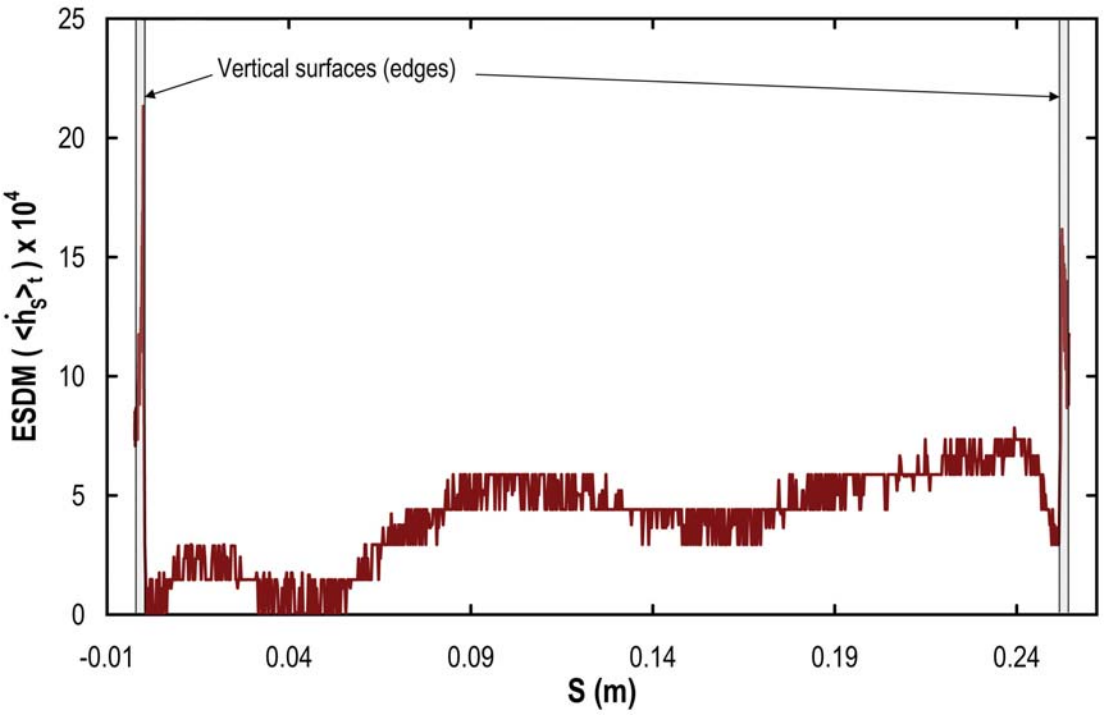

Figure 3.3: Experimental standard deviation of the mean (ESDM) of the time-averaged heat flux across the heat exchanger surface S, $\langle \dot{h}_S \rangle_t$. The ESDM result for vertical edge surfaces at each end of the plate are highlighted.

Figure 3.3 shows the ESDM of the time-averaged heat flux across the heat exchanger surface S, $\langle \dot{h}_S \rangle_t$. The ESDM for the performance measure $\int \langle \dot{h}_y \rangle_t dA$ is $\approx 5.36 \text{x} 10^{-5}$, or over six orders of magnitude less than the smallest result expected. Using a similar method, the estimated ESDM of $\Delta T_{k,hx}$ was found to be less than 10^{-5}. On this basis, this modelling approach is demonstrated to offer excellent

repeatability, and minimise as far as practicable the associated convergence error.

Within the *Fluent* environment, additional error reporting functions are available. The mass imbalance over the entire fluid volume is calculated internally and was determined to be at least five orders of magnitude less than the time-averaged mass of fluid within the domain at limit state operation. For example, the mass imbalance of fluid for Run 4 of Chapter 6 was reported by Fluent to be 4.205 x 10^{-8} kg/s with 14.37g of helium within the domain, or a rate of just over 3.4 grams/s per tonne. This is acceptable in the context of this study.

3.2.1.2 Uncertainty of model predictions

The estimated uncertainty of measurement for various performance measures at full scale are provided in Table 3.1 based upon the findings in Appendices B.2, B.3, B.4 and Section 3.2.1.1, and therefore include effects of convergence (residual) error, spatial and temporal discretisation of the governing equations, and truncation or round-off errors. U_{95} is defined as the expanded uncertainty at a 95% confidence limit, and k is the coverage factor (also known as *Student's* t-factor) (Cook 1999).

Table 3.1: Expanded uncertainty of measurement.

	Chapter 4	results	Chapter 5	results
Measurand	U_{95}	k	U_{95}	k
$\Delta T_{k,hx}$	0.21K	1.99	0.13K	1.98
$\left\langle \dot{h}_y \right\rangle_t$, $\dot{Q}_{S,\text{cold}}$	1.38W/m^2	1.97	0.4W/m^2	1.98

U_{95} is improved in the results presented in Chapter 5 through use of more detailed meshing (profiles 'G3' and 'G5' over 'G2'), timescale sizing (profile 'T1' and 'T2' over 'T3') and increased retention of significant figures during the post-processing of results.

3.2.2 Physical implementation and boundary conditions

The following subsections present discussion of the key factors expected to lead to significant variations between numerical and experimental results of thermoacoustic devices.

3.2.2.1 Limit states

In transient or unsteady thermoacoustics, a key term used is the 'limit state' or 'limit cycle', which refers to the state of operation or operating conditions in which the phase and magnitude of state variables such as p, U and T at each phase in the cycle do not vary from one oscillation to the next. At the limit cycle, the time-averaged change in enthalpy and entropy flux is zero and the enthalpy flux becomes constant and uniform along the length of the device (Bauwens 1998). Limit-cycle simplifications used in Rott's approximations (Rott 1980) are not capable of accurately predicting the performance of thermoacoustic systems in transient states, although this is not currently of specific interest to the study of thermoacoustic couples.

In the context of numerical modelling thermoacoustic couples, in this thesis use of the term 'limit state' is not equivalent to an experimental sense, where the limit state is usually observed from stabilisation of measured temperature differences (with orders-of-magnitude larger time constants). Here, the simulation is advanced in time until pressure, velocity and performance measures such as $\Delta T_{k,hx}$ and $\langle \dot{h}_{hx} \rangle_t$ stabilise to within set limits on a cycle to cycle basis. The simulation does not continue until the time-averaged change in enthalpy and entropy flux is zero, as applied boundary conditions on the plate, end wall and inlet surfaces would then control the rate of any energy transfer out of the domain and the computed result would still be no more compatible with experimental data. Instead, the time-averaged change in enthalpy and entropy flux is identified as reasonably

constant in the timeframe for which results are presented.

In Section B.5 of Appendix B, results are presented for a numerical model intended to predict the time-averaged gas temperature distribution. Implemented as per Section 3.1 and Appendix B but continued for a time period 100 times longer than usual (over 2,275 acoustic cycles instead of the default 20), this model overpredicted the temperature gradient obtained experimentally. There are however, some concerns regarding the influence of the thermocouple wires on the experimental results and some unknowns with regard to the experimental method, although demonstrably logarithmic growth in calculated temperature difference in the numerical model results highlights the potential for error in the selection of boundary conditions and computational domain size. In this thesis, this error potential is minimised through consistent selection of boundary conditions in the studies presented in Chapters 4 and 5. A comparison between Run 4 in Chapter 6 and Run 4 in Section D.3 indicates that the selection of symmetric boundary conditions was suitable in the context of available computational resources and requirements for comparison with previous studies.

3.2.2.2 Influence of adjacent heat exchangers

Besnoin (2001) and Marx & Blanc-Benon (2004*b*) acknowledge that the location of heat exchangers at each end of a parallel plate stack will influence the flow field interacting with the stack surface. In a similar study to Besnoin (2001), Marx & Blanc-Benon (2004*b*) considered the presence of adjacent heat exchange surfaces (with suitably higher thermal conductivity properties) at each end of a stack surface and presented results for various combinations of stack and heat exchanger lengths and location. However in a deviation from the dissertation of Besnoin (2001), all heat exchanging surfaces in all runs considered by Marx & Blanc-Benon (2004*b*) were considered to be of zero thickness and hence did not present the same physical

flow impedance expected from a non-zero thickness example.

Marx & Blanc-Benon (2004*b*) and Besnoin (2001) assumed the heat exchanger plates were aligned with the stack surfaces. In physical examples, heat exchangers adjacent to parallel plate stacks are typically offset and at different pitch scales to the stack plates. This creates a significant challenge to those who may try to incorporate this variation yet model the acoustic flow field in high fidelity, since the heat exchangers are offset from the stack plates.

Consideration of the various pitch scales and offset distances would require either a large series of runs based upon a parametric approach, or a model which considers the wider cross sections of the stack and heat exchanger region such that wall or symmetric boundary conditions may be imposed on boundaries parallel to the flow. Both approaches were considered to be too computationally expensive for these studies and therefore heat exchangers at each of the stack region were omitted.

3.2.2.3 Edge condition and shape

Variation in the shape and size of each individual stack pore will lead to challenges in predicting the expected stack performance and may require a statistical approach to represent the typical solution domain.

Chapter 5 presents discussion and results of an investigation which considers the influence of stack tip (or edge) shape upon the performance of a thermoacoustic couple model.

3.2.2.4 Acoustic streaming

Recent publications by Bailliet et al. (2001) and Swift (2002) acknowledge that various forms of time-averaged finite mean velocity, or 'acoustic streaming', exist in

both travelling-wave and standing-wave thermoacoustic devices.

The 'half-spacing' thermoacoustic couple model requires that the upper and lower fluid boundaries be periodic (when modelling a full pore width) or symmetrical. This requirement reduces the computational cost associated with the model, but most likely suppresses the ability to model forms of acoustic streaming which occur near those boundaries. In the case of streaming around stack plates, this would require modelling of multiple channel pores. Acoustic streaming, referred to in other work as 'acoustic streaming instabilities' (So et al. 2006) and 'mass streaming' (Swift 2002), is discussed further in Section 2.3.

The description of acoustic streaming by So et al. (2006) suggests that it is likely to be asymmetric in the pipe axis since the flow impedance of the stack would never be perfectly symmetrical in its axis. An attempt to capture this effect by modelling a half section of a parallel plate stack including four whole stack plates and applying a symmetry condition on the pipe axis is presented in Chapter 6. The results presented in this chapter indicate that the multiple plate model is shown to be capable of modelling acoustic streaming localised to the stack plates and therefore addressing the fourth 'gap' identified in Section 2.4. The expanded thermoacoustic couple model is shown to be effective in the identification of conditions for which acoustic streaming is likely to occur.

Chapter 4

On the effect of blockage ratio upon the performance of thermoacoustic couples

The vast proportion of two-dimensional numerical studies specific to thermoacoustic devices in the literature have modelled what Wheatley et al. (1983) termed a 'thermoacoustic couple' (TAC), which in its most abstract form is a single infinitely wide plate in an oscillatory flow field. Presumably, the thermoacoustic couple is intended to be a two-dimensional approximation of a stack consisting of a series of parallel plates. Thermoacoustic couples are best described as a 'short stack' (being much shorter than the acoustic wavelength) consisting of only a few parallel plates inside the resonator duct. The majority of numerical studies of thermoacoustic couples assume infinite periodicity (infinite number of plates) in the transverse direction of the duct. Infinite periodicity infers that the flow structure in the vicinity of the plate may therefore be periodic and/or symmetrical in the transverse direction. Using this assumption only one side of a single, infinitely wide stack plate is modelled on a boundary of a two-dimensional computational domain.

The study of Worlikar & Knio (1996) and dissertation of Besnoin (2001) are examples of numerical models in which *two* halves of parallel stack plates are modelled including the full plate-spacing. The results presented by Worlikar & Knio indicate that the flow structure is symmetrical at low pressure amplitudes, although Besnoin demonstrated numerically that at higher pressure amplitudes the flow was strongly asymmetrical for various combinations of stack geometry.

This study aims to build upon existing knowledge by using CFD to investigate the effect of increased drive-ratio and plate thickness upon the time-averaged heat transfer rate through a stack. The models presented in this study include finite heat conductivity and heat capacity for plates of zero and non-zero thickness.

A detailed discussion of work related to the current study is provided in the following subsections.

In Section 4.1, the numerical model, operating conditions and performance characteristics considered are introduced. Results are presented in Section 4.2 using two different viewpoints. Section 4.2.1 contains discussion of the flow structures that develop, and Section 4.2.2 reports on the influence of plate thickness upon the distribution of heat flux across the plate surface.

Results presented in the following subsections demonstrate that the introduction of finite plate thickness into the model produces new results which show significant disturbances to the flow field and changes to the expected rate and distribution of heat flux along the stack plate. The thickness of the plate, t_s, is found to strongly influence the generation of vortices outside the stack region and perturbs the flow structure and heat flux distribution at the extremities of the plate. Increases in t_s are also shown to improve the integral of the total heat transfer rate but at

the expense of increased entropy generation. The results presented in this chapter therefore address the first and second 'gaps' in the current knowledge, summarised in Section 2.4.

4.1 Numerical model

Figure 4.1 shows a sketch of the computational domain of the half-wavelength resonator. The resonator is shown as a two-dimensional representation of a smooth duct with rigid terminations at each end. Ignoring effects of the finite resonator diameter and duct surfaces, a parallel plate stack located inside the resonator is then for the purposes of this study, of infinite width.

Figure 4.2 presents a comparison of computational domains used in previous studies relevant to the current work (Ishikawa & Mee 2002, Piccolo & Pistone 2006). To enable comparison with these studies, the numerical model described here uses similar operating conditions but an expanded solution domain to account for physical flow disturbances. The model approximates a closed-ended, half-wavelength standing-wave resonator duct filled with helium at 10kPa absolute pressure, with a parallel-plate stack located in one end of the device. As the resonator length is fixed at 5.04m and the sound speed of the gas at ambient temperature T_0=300K is c_0=1008m/s, the operating frequency of the device is fixed to have its first natural frequency at 100Hz. The origin of the computational domain (x=0, y=0) is shown in Figure 4.2(d), at the left end of the stack region. The origin is located 1.194m to the right of the centre of the duct where x'=0, i.e. x'=x+1.194m.

4.1.1 Modelspace

The computational domain used for the current work is divided into six subdomains which together can facilitate changes to the fundamental characteristics of the

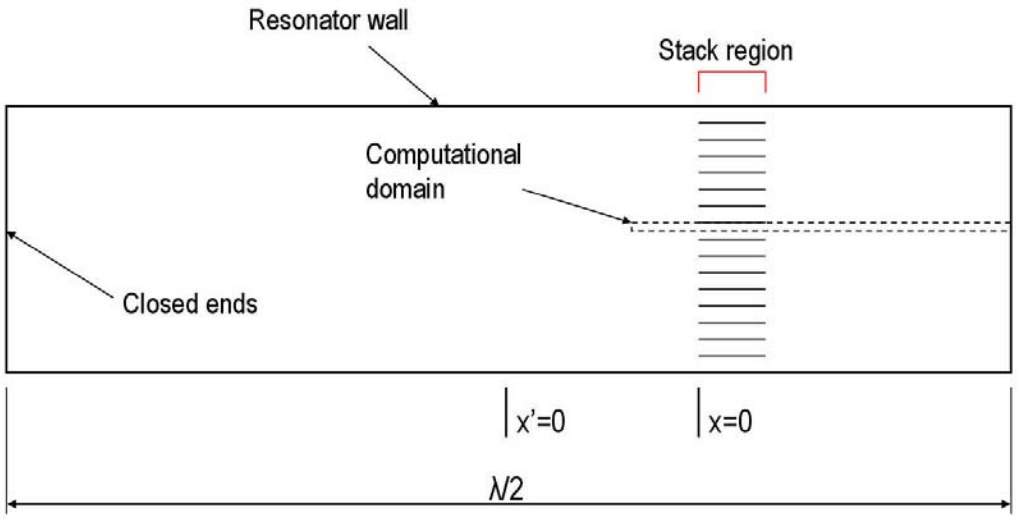

Figure 4.1: Region of the computational domain within the basic theoretical model of half-wavelength resonator tube with parallel plate stack. The acoustic source is located at the left end of the computational domain (not shown).

thermoacoustic environment, such as the addition of plate thickness or duct length. Figure 3.1 shows a sketch of the modelspace used in this study.

The plate and thermal reservoir comprises subdomains 'P' and 'H' respectively. Subdomain 'S' is the region encompassed by the plate axially within the stack. The length y_0 is the half-spacing between plate centrelines. Subdomains 'A' and 'B' enable consideration of flow structures which may develop outside the stack region due to non-zero plate half-thickness t_s, and are of sufficient lengths L_A and L_B such that the pressure changes can be considered adiabatic. Subdomain 'C' links subdomain 'B' to the hard walled end of the duct at the right edge of subdomain 'C'. Symmetric boundary conditions have been imposed on all lateral fluid boundaries and an oscillatory boundary condition on the left side of subdomain 'A', has been used to represent an acoustic standing-wave.

The inclusion of subdomain 'H' is to allow plates of zero thickness to be modelled with finite heat capacity and thermal conductivity. To provide comparative results with Ishikawa & Mee (2002) and Piccolo & Pistone (2006), the subdomain 'P' is set

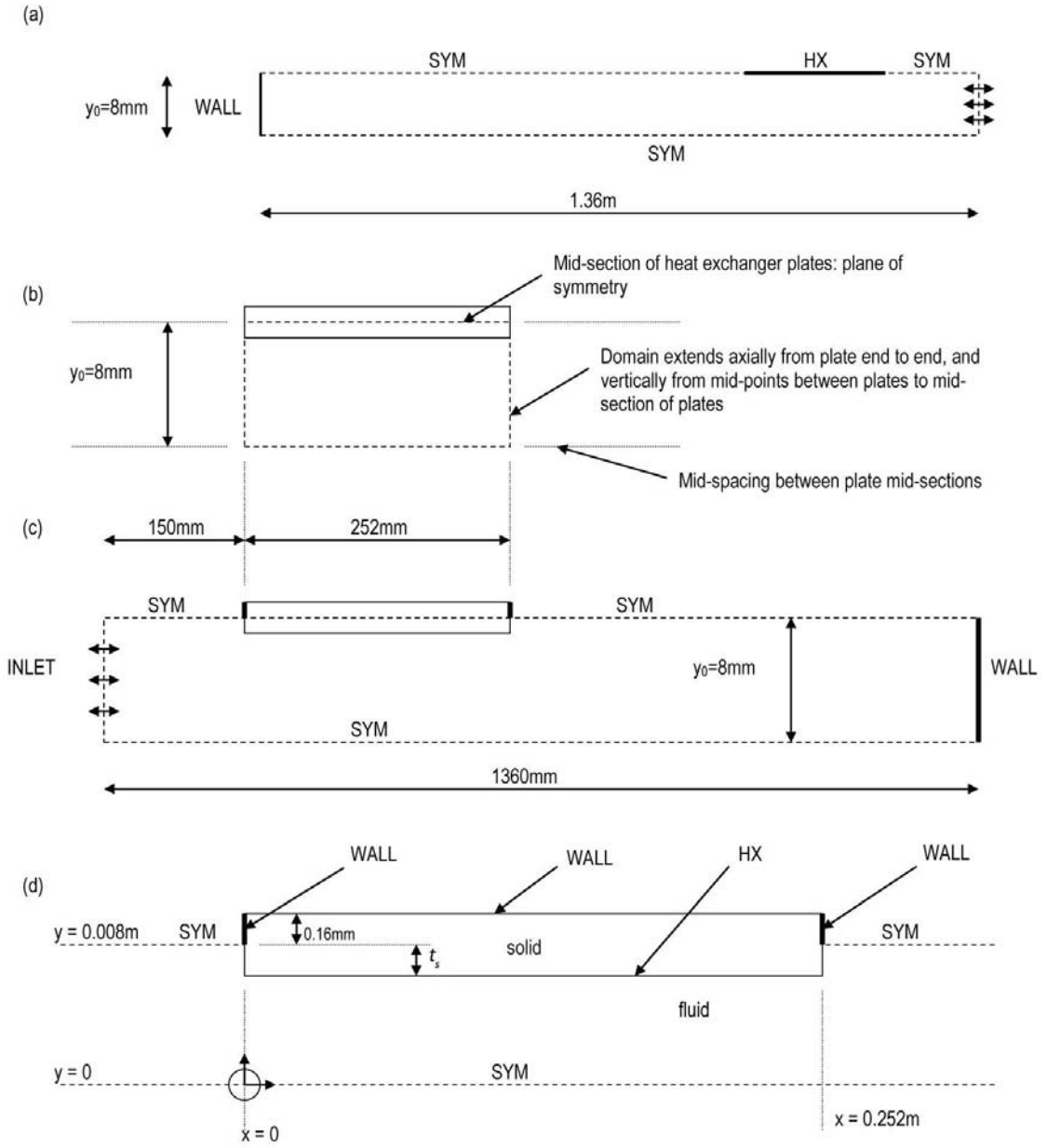

Figure 4.2: Comparison of computational domains used by (a) Ishikawa & Mee (2002), (b) Piccolo & Pistone (2006) and (c) this study. (d) a closer view of the stack region shown in (c).

to zero thickness, and subdomains 'H' and 'S' are adjacent. In following Piccolo & Pistone (2006), the top and sides of subdomain 'H' are thermally insulated, forcing any excess heat entering regions 'H' and 'P' to return back through the boundaries between subdomain 'P' and subdomains 'A', 'S' and 'B'. The thermal properties of the stack are important as unsteady temperature distributions are allowed to

form within the stack region. The thickness and hence influence of subdomain 'H' is intended to be minimal compared to that of subdomain 'P'.

The number of mesh intervals in the x and y directions, n_x and n_y respectively, can be easily adjusted to explore the grid dependency of the model or match the sizings used by previous studies. For example, in Section 4.1.3 where comparisons are drawn with the results of Piccolo & Pistone (2006), n_{xS}=244 and n_y=n_{yS}=50, with L_S=0.252m.

The effect of non-zero plate thickness can be accomodated by varying t_s, indicated as the vertical size of subdomain 'P'. To preserve a consistent and rectangular computational mesh, n_{yP} is increased at the expense of n_{yS} such that n_y=n_{yP}+n_{yS}. The transverse dimension (thickness) of subdomain 'H' was held fixed and equal to the grid interval size in the y direction, Δy=0.16mm.

4.1.2 Boundary conditions

Figures 4.3(a) and 4.3(b) indicate the boundary types and various length scales used in this study. The conditions imposed upon the boundaries shown in Figures 4.3(a) and 4.3(b) are described by Equations (4.1) to (4.5) with u and v the components of velocity in the x and y directions, and x' being the axial distance from the centre of the duct.

$$\left.\begin{array}{l} u = 0 \\ v = 0 \\ \frac{dT}{dy} = 0 \end{array}\right\} \text{on axial 'WALL' boundaries,} \tag{4.1}$$

$$\left.\begin{array}{l} u = 0 \\ v = 0 \\ \frac{dT}{dx} = 0 \end{array}\right\} \text{on transverse 'WALL' boundaries,} \tag{4.2}$$

$$\left.\begin{array}{l} u = 0 \\ v = 0 \end{array}\right\} \text{on 'HX' boundaries,} \tag{4.3}$$

$$\left.\begin{array}{l} v = 0 \\ \frac{dT}{dy} = 0 \end{array}\right\} \text{on 'SYM' boundaries, and} \tag{4.4}$$

$$\left.p = p_m + Re\left[|p_1|\, e^{j(\omega t + kx' - \frac{\pi}{2})}\right]\right\} \text{on 'INLET' boundaries.} \tag{4.5}$$

The axial length of subdomains 'A' and 'B' were set equal to L_A=L_B=0.15m. The axial length of the computational domain, L_{CV}, was set to 1.476m.

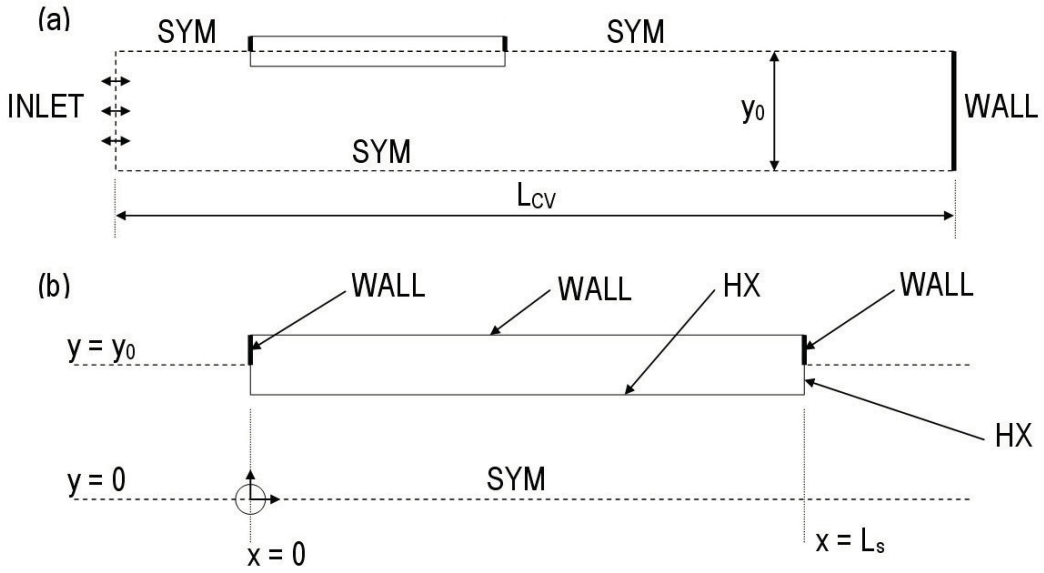

Figure 4.3: Computational domains used in this study showing boundary conditions and selected geometry. (b) a closer view of the stack region shown in (a).

4.1.3 Operating conditions

Throughout the computational domain, the pressure, velocity and temperature were initialised at ambient conditions, that is

$$\left.\begin{aligned} u &= 0 \\ v &= 0 \\ T_k &= T_m \end{aligned}\right\} \text{for } t{=}0 \text{ at all } x \text{ and } y. \tag{4.6}$$

By following Ishikawa & Mee (2002), where the operating frequency f=100Hz, T_m=300K and p_m=10kPa (approximately 0.1 atmospheres) for all runs, the mean thermal penetration distance $\delta_{\kappa m}$ $(=\sqrt{2k/\omega\rho c_p})$ is ≈2.4mm for helium as the working fluid.

Flow and geometry parameters for each run are listed in Table 4.1. Twenty-one runs were completed covering typically four different drive-ratios for five different plate half-thicknesses t_s. The drive-ratio DR is defined as the ratio of the maximum oscillatory pressure amplitude divided by the ambient pressure p_m. The blockage ratio BR is defined as the ratio of open gas area to total device cross sectional area. The BR of a thermoacoustic couple is commonly evaluated as simply

$$BR = 1 - \frac{t_s}{y_0}. \tag{4.7}$$

In addition, Run 22 was developed to compare the current results to those published by Piccolo & Pistone (2006) and hence uses the same operating conditions as Run 1, however it differs in grid mesh density.

4.1.3.1 Turbulence criteria

The approximate free stream 'acoustic' Mach number M_a is defined as

Table 4.1: Flow and geometry parameters for each simulation run used in investigating blockage ratio. Run 22 only differs from Run 1 in using a mesh with grid mesh sizing equivalent to that used by Piccolo & Pistone (2006). DR=$|p_1|/p_m$.

Run	$\|p_1\|$ (Pa)	$\|p_1\|/p_m$ (%)	t_s (mm)	$\delta_{\kappa m}/t_s$	BR
1	170	1.7	0	∞	1
2	340	3.4	0	∞	1
3	510	5.1	0	∞	1
4	680	6.8	0	∞	1
5	170	1.7	0.16	15	0.98
6	340	3.4	0.16	15	0.98
7	510	5.1	0.16	15	0.98
8	680	6.8	0.16	15	0.98
9	170	1.7	0.80	3.0	0.9
10	340	3.4	0.80	3.0	0.9
11	510	5.1	0.80	3.0	0.9
12	680	6.8	0.80	3.0	0.9
13	170	1.7	1.6	1.5	0.8
14	340	3.4	1.6	1.5	0.8
15	510	5.1	1.6	1.5	0.8
16	680	6.8	1.6	1.5	0.8
17	170	1.7	2.4	1.0	0.7
18	340	3.4	2.4	1.0	0.7
19	510	5.1	2.4	1.0	0.7
20	680	6.8	2.4	1.0	0.7
21	850	8.5	2.4	1.0	0.7
22	170	1.7	0	∞	1

$$M_a = \frac{p_1}{\rho_m c^2} \tag{4.8}$$

where p_1 is the acoustic pressure amplitude and c is the gas sound speed. M_a is a useful measure of the "nonlinear behaviour" of the system or an indicator of flow instabilities, linked to the acoustic pressure amplitude (Swift 2002, p153). To compensate somewhat for the effect of blockage ratio BR within stack pores, M_a can be modified to

$$M_a = (2 - BR)\frac{|p_1|}{\rho_m c^2}\cos(kx'). \tag{4.9}$$

This modification follows from the method used by Piccolo & Pistone (2006, Equation 9) and Swift (1988, Equation 61) for setting volume velocity boundary conditions. Poese & Garrett (2000) estimated that drive-ratios of greater than 3% would most likely result in non-linear effects becoming significant, however a similar limit for M_a is not clear. The results presented here include the values of M_a to provide further insight into a linear approximation limit based upon M_a. The free stream Mach number M defined by

$$M = \frac{|u_1|}{c} \tag{4.10}$$

where u_1 is the acoustic velocity amplitude, will also be used as measure of the "nonlinear" behaviour.

In the 'short stack' approximation familiar to thermoacoustic system designers, M_a may be calculated directly and assumed constant within the stack region. In this study, where the amplitude of the local Mach number varies considerably through the stack region, values of M at the mid-spacing and the mid-length of the stack region ($x = L_S/2$, $y = 0$) will be compared with M_a.

Ishikawa & Mee (2002) and Piccolo & Pistone (2006) neglected turbulence effects in each of their studies on the basis that the streaming Reynolds number (Thompson 1987), given by

$$N_{R,S} = \frac{|u_1|^2}{\upsilon\omega} \tag{4.11}$$

was not expected to exceed $(200)^2$ based on the results of Merkli & Thomann (1975*a*). In the context of oscillatory flow, the critical Reynolds number $N^c_{R,S}$ is the condition for which the flow is considered to transition to a turbulent flow

regime (Merkli & Thomann 1975a), that is, the condition for which the Stokes layer becomes unstable (Thompson 1987). Merkli & Thomann (1975a) indicated that this transition at $N^c_{R,S}$ is effectively localised to the boundary layer, provided that the boundary layer thickness is significantly less than "other dimensions" such as the tube radius. In other words, the limiting $N^c_{R,S}$ value of $(200)^2$ was developed for internal flows without small features (Merkli & Thomann 1975a). However, in typical thermoacoustic systems using parallel-plate stacks, the plate thickness is much smaller than the tube radius and could potentially be of similar thickness to the Stokes layer. In this thesis, $N_{R,S}$ values are presented as squared values because they are related to the square of the Reynolds number based upon the boundary layer thickness (Merkli & Thomann 1975a).

The flow impedance created by increasing plate thickness l=$2t_s$ leads to higher velocities and therefore higher $N_{R,S}$ values within the stack region. Decreasing the blockage ratio (thicker plates) would further increase $N_{R,S}$. Concern that decreasing the blockage ratio would increase $N_{R,S}$ above $(200)^2$ was addressed using the model for Run 21, which had the lowest (most flow restrictive) blockage ratio (0.7) and highest drive-ratio (8.5%) of the models used in this study. Comparison of the $N_{R,S}$ values with the limiting value is provided in Section 4.2.1.1.

4.1.4 Material properties

To enable comparison with the results of Ishikawa & Mee (2002) and hence the results of other studies using the same operating conditions (Cao et al. 1996, Piccolo & Pistone 2006), the properties listed in Table 4.2 are common to all tests in this investigation. Density was approximated using the ideal gas law, where constant Prandtl number, specific heats and thermal conductivity were assumed.

The heat exchanger plate material properties of material density and thermal

Table 4.2: Flow conditions and material properties used for all computational runs presented in Chapter 4.

Property	**Value**	**Units**
Operating frequency, f	100	Hz
Ambient temperature, T_m	300	K
Mean pressure, p_m	10	kPa
Gas properties:		
Prandtl number, σ	0.69	
Thermal conductivity, k_0	0.149	W/mK
Heat capacity, c_p	5,193	J/kgK
Dynamic viscosity, μ	2.01 x 10^{-5}	kg/ms
Ratio of specific heats, γ	1.665	
Plate material properties:		
Thermal conductivity, k_s	10	W/mK
Heat capacity, c_{ps}	400	J/kgK
Density, ρ_s	400	kg/m^3

heat capacity were held constant at 400kg/m^3 and 400J/kgK respectively. In following Piccolo & Pistone (2006), a constant thermal conductivity k_s of 10W/mK was applied to the stack region represented by subdomains 'H' and 'P' shown in Figure 3.1. In practice, stack plates have a relatively lower rate of internal thermal diffusivity to that modelled due to higher thermal capacity, higher density and lower thermal conductivity. The plate material properties for the stack region have been arbitrarily set to have a higher internal diffusivity to reduce the time for which thermal gradients develop in the stack region for the given simulation timeframe, and hence enable any subtle performance differences to be detected with greater clarity.

4.1.5 Numerical implementation

The commercial CFD software *Fluent* (version 6.2.16) was used to conduct 2-D simulations of the system. An unsteady formulation was used with first-order discretisation of flow. To enable sufficient resolution of each waveform, 100 time steps per period of oscillation (1/100 seconds) were selected, which resulted in a time step size of one ten thousandth of a second (0.1ms). Convergence criteria for the solution at each time step were based upon the residuals for velocity components and conti-

nuity equal to or below 0.01%, and the residual for energy equal to or below 0.0001%.

For each run, a sinusoidal pressure input was applied to the inlet boundary shown in Figure 4.3(a) with frequency f=100Hz and amplitude $|p_1|$ as listed in Table 4.1.

A mesh spacing of Δx equal to 0.5mm and Δy equal to 0.16mm within the stack region (subdomain 'S' shown in Figure 3.1) was used, however at increasing axial distances from the stack region, that is, decreasing x for $x \leq 0$ and increasing x for $x \geq L_S$, Δx was exponentially increased to reflect less 'detailed' or adiabatic oscillations distant from the stack region. The domains used for Runs 1 to 20 each contained approximately 33,900 nodes. A number of modified grids were also used. Grid independency was checked using a finer mesh with double the number of nodes in the x and y directions (n_x, n_y) or four times greater node density. To match the grid mesh profile used in Run 1 of Piccolo & Pistone (2006), the x-direction mesh sizing Δx was increased to 1.033mm whilst Δy was retained at 0.16mm within the stack region. This resulted in a total of approximately 16,860 nodes used for Run 22.

Figure 4.4 presents the values of p_1, u_1 and $\Delta T_{k,hx}$ normalised by their respective limit state levels, at the oscillatory inlet boundary versus simulation time. Whilst the pressure and velocity states approach a limit-state within the first three to four cycles of simulation, the performance measure $\Delta T_{k,hx}$ reaches the same condition after the first twenty cycles of simulation. Therefore, to ensure each simulation achieved limit state operation, two thousand time steps (twenty oscillations) were calculated to initialise each model. An additional 100 time steps (1 full cycle) were calculated with statistical averaging employed to determine properties such as the time-averaged heat flux distribution or flow parameter.

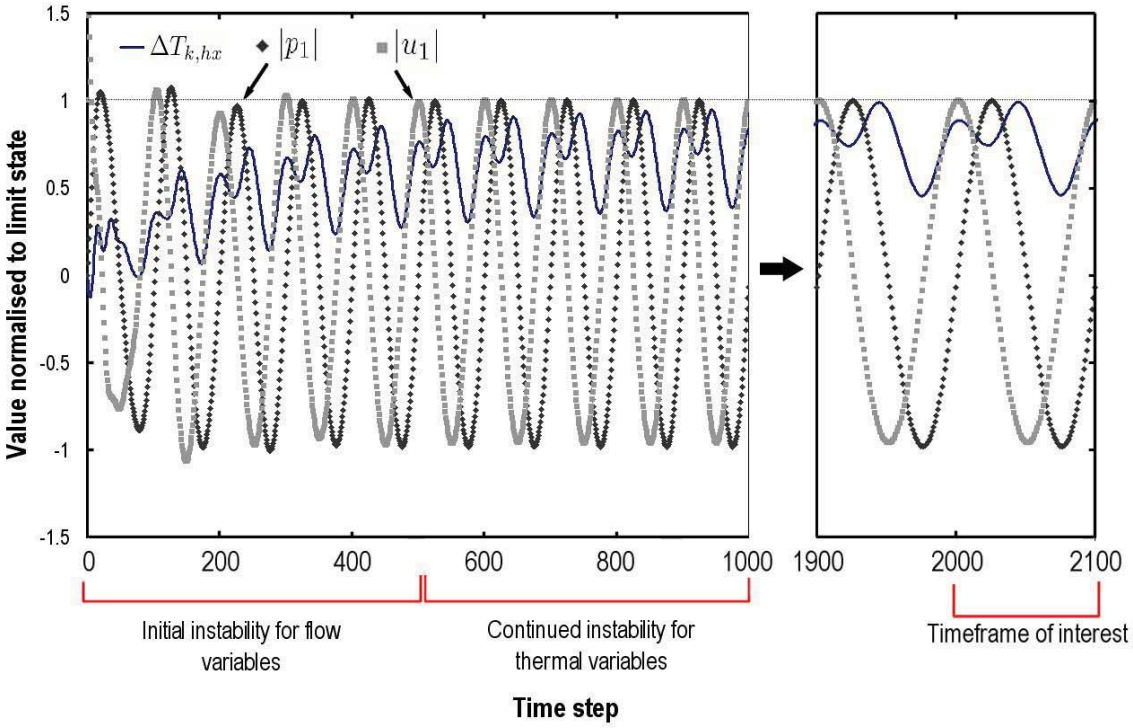

Figure 4.4: p_1, u_1 and $\Delta T_{k,hx}$ (Section 4.1.5.1) at the oscillatory boundary (INLET) versus simulation timesteps 0 to 1000 and 1900 to 2100 for Run 6. Positive velocity is to the right with reference to Figure 4.3.

Figure 4.5 presents the temperature versus specific entropy for the position at the stack plate mid-length (x=0.5L_S) and mid-plate line (y=0) over the first ten cycles of Run 1. This figure indicates that gas states within the stack region approach a limit-state condition at approximately the sixth or seventh cycle.

Note that the ratio $\delta_{\kappa m}/y_0$ is fixed at 0.3 for all runs, because in each simulation the plates are modelled as fixed at centreline distances 16mm apart but increasing in thickness. The ratio of thermal penetration depth to plate-spacing (=2y_0) is therefore also fixed at 0.15. With the plate half-thickness t_s set equal to the thermal penetration depth $\delta_{\kappa m}$, it is the author's opinion that the blockage ratio used in Runs 16 to 20 is representative of a practical system with the same operating conditions.

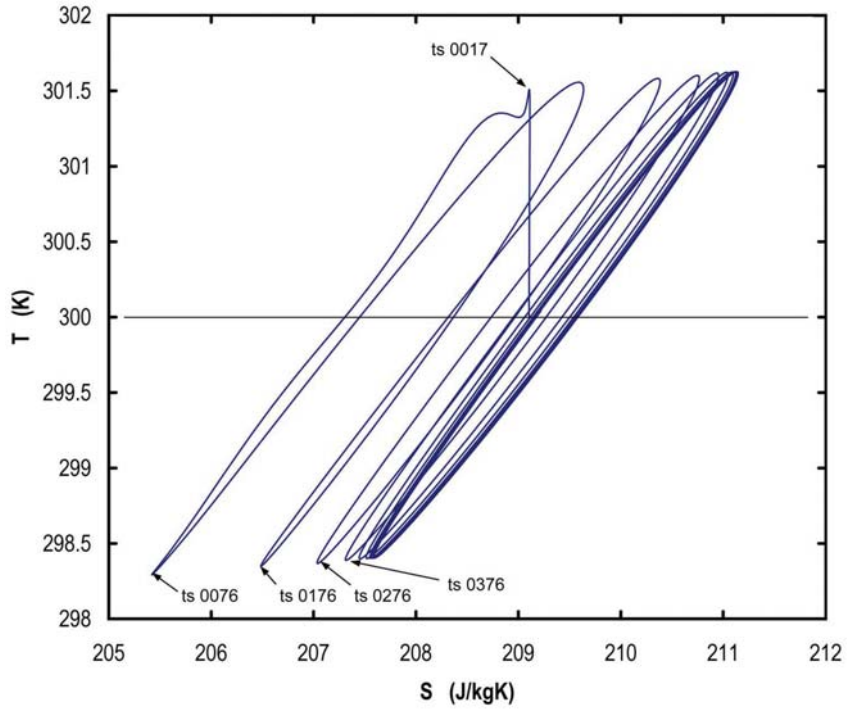

Figure 4.5: Temperature versus specific entropy for position at the midspacing and the midlength of the stack region ($x = L_S/2$, $y = 0$) over the first ten cycles of Run 1. Points of interest are marked for time steps 0017 (flow-time 0.0017s), 0076 (flow-time 0.0076s) and 0176 (flow-time 0.0176s).

4.1.5.1 Performance scales

Performance metrics for the model have been developed to identify limit-state operation and for performance comparisons between each mode of operation. The time-averaged difference in area-weighted average gas temperature between each end of the stack at x=0 and x=L_S is defined as

$$\Delta T_{k,hx} = \langle \left(|T_k|_{x=L_S} - |T_k|_{x=0} \right) \rangle_t \tag{4.12}$$

and could be considered the axial gas temperature difference across the heat exchanging surface, hence the subscript 'hx'.

The distribution of time-averaged heat flux density over an oscillatory cycle at a fluid-solid boundary, $\left\langle \dot{h} \right\rangle_t$ is a useful performance measure that has been

used in the majority of previous studies of thermoacoustic couples. Since previous studies considered a stack plate of zero thickness, this quantity was also referred to as a time-averaged heat flux in the y-direction, here represented by $\left\langle \dot{h}_y \right\rangle_t$. As plates of non-zero thickness will be considered in this study, time-averaged axial or horizontal heat fluxes through the end tips of the stack plates will exist and shall be denoted by $\left\langle \dot{h}_x \right\rangle_t$. The term $\langle \dot{h}_{hx} \rangle_t$ will refer to the time-averaged heat flux through all fluid-solid boundaries of the stack plate.

The thermodynamic cycles experienced by the gas at fixed positions in the computational domain can also yield insight into the performance of the stack configuration. Table 4.3 indicates fixed positions (using the co-ordinate system shown in Figure 4.3(b)) that have been designated as points of interest. Figure 4.6 shows a diagram indicating the location of each point of interest listed in Table 4.3.

Table 4.3: Measurement points of interest.

Code	x	y	**Comments**
C1	0	0	'C' for cold end
M1	$0.5L_S$	0	*c.f.* Position 'M' of Marx & Blanc-Benon (2005*b*)
H1	L_S	0	'H' for hot end
C2	0	y_{hxsf} - $0.5\delta_{\kappa m}$	spaced $0.5\delta_{\kappa m}$ from plate surface
M2	$0.5L_S$	y_{hxsf} - $0.5\delta_{\kappa m}$	'M' for midlength
H2	L_S	y_{hxsf} - $0.5\delta_{\kappa m}$	

Locations C1, M1 and H1 are located transversely on the line of symmetry at mid-spacing between each plate surface (y=0) and axially within the stack region ($0 \leq x \leq L_S$). Locations C2, M2 and H2 are transversely located within half the mean thermal penetration distance of the fluid-solid interface, and gas particles here should theoretically experience a greater heat-pumping effect than those on y=0.

A final performance measure used in this study is the energy dissipation rate

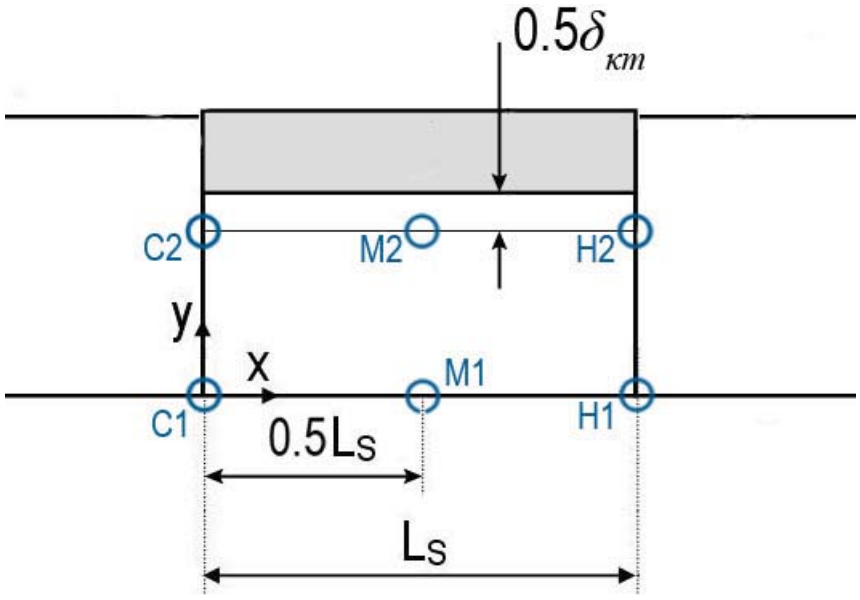

Figure 4.6: Diagram indicating measurement points of interest listed in Table 4.3. Diagram is not to scale.

due to irreversibilities associated with flow disturbances. With the subdomains A, B, C and S shown in Figure 3.1 forming the closed-system volume CV, the rate of change in total system entropy is described by

$$\frac{dS}{dt} = \oint_{CV} \frac{\dot{h}}{T_0} + \dot{S}_{\text{gen}} \tag{4.13}$$

where $\oint_{CV} \dot{h}/T_0$ is the rate of entropy change from heat flux $\dot{h}$ transferred with an external reservoir at temperature T_0, and $\dot{S}_{\text{gen}}$ is the total rate of entropy generated within the system, and (Swift & Wollan 2002, Equation 6.10)

$$\dot{W}_{\text{diss}} = -T_0 \dot{S}_{\text{gen}}. \tag{4.14}$$

where $\dot{W}_{\text{diss}}$ is the lost power due to entropy generation.

At limit state operation, the time rate of change of entropy of the system dS/dt is considered constant, and since all external boundaries to the model

except the 'INLET' boundary are insulated, the rate of energy dissipation due to entropy generation $\dot{W}_{\text{diss}}$ can be approximated using Equation (4.14) over a full oscillatory cycle. In evaluating entropic losses of thermoacoustic couples, Ishikawa & Mee (2002) used this method to show that the increase in rate of entropy generation $\dot{S}_{\text{gen}}$ with drive-ratio has a quadratic relationship for a plate of zero thickness.

However, the *Fluent* software also allows direct measurement of the volume-averaged entropy change dS/dt, and since all external boundaries to the model except the 'INLET' boundary are insulated, in this study, $\bar{\dot{S}}_{\text{gen}}$ can be evaluated by

$$\bar{\dot{S}}_{\text{gen}} = \frac{d\bar{S}}{dt} - \int_{\text{INLET}} \frac{\bar{\dot{q}}}{\bar{T}} \tag{4.15}$$

where the overbar indicates values averaged over a full oscillation.

4.2 Results

In this section results are presented in terms of the computed flow parameters, the observed flow structures and the rate of heat transportation and dissipation in each run.

4.2.1 Flow parameters

The discussion of flow parameters will include a comparison with linear estimates of turbulent limits, the generation of flow vortices and velocity gradients.

4.2.1.1 Comparison with turbulence criteria

It is important to first investigate whether the introduction of the finite plate thickness $2t_s$ in this study leads to instability of the Stokes boundary layer, since numerical models specific to modelling turbulent behaviour such as the Reynolds Stress Model (RSM) were not incorporated into the computational solver for this

study. Numerical models specific to modelling turbulent behaviour are unnecessary for the following simulations in which the flow conditions correspond to the laminar regime of oscillating flow.

Figure 4.7 presents the distribution of mean and RMS velocity magnitude along the mid-plate line (y=0) for Run 20. As expected, the RMS velocity is relatively higher throughout the stack region due to the reduced cross section. However, Figure 4.7 shows that whilst the mean velocity is effectively zero at sufficient distance from the stack (which is to be expected at these locations where the flow is theoretically an adiabatic standing-wave), there is non-zero mean gas flow at the extremities of the stack. These non-zero mean flows indicate that the flow is perturbed by the plate structure and suggest flow recirculation (streaming) effects at these locations.

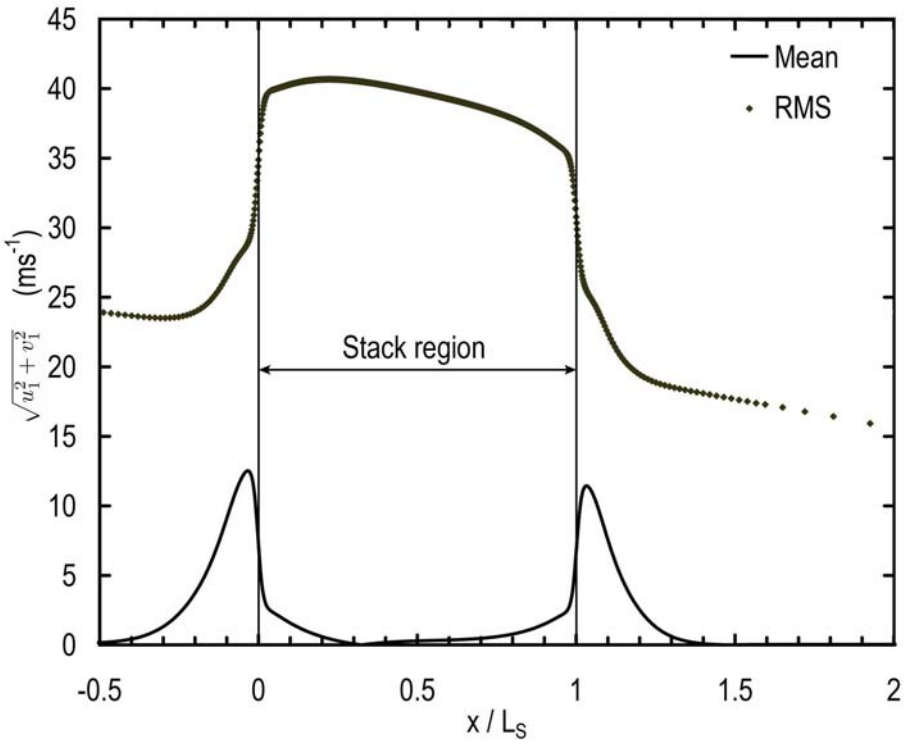

Figure 4.7: Estimated distribution of mean and RMS velocity magnitude along the mid-plate line (y=0), for the time period 0.2000s to 0.2100s. Data shown is for Run 20, with BR=0.7 and DR=6.8%.

Table 4.4 lists the estimated flow parameters used here for the assessment of turbulence. The mean free stream Mach number M as defined in Equation (4.10) and the 'acoustic' Mach number M_a as defined in Equation (4.8) are also provided in Table 4.4, where the overbar represents the mean.

The leftmost plate edge at x=0 (which is closer to the velocity antinode in the theoretical half-wavelength resonator) has greater velocities than at x=$L_S/2$ (0.126m), however the changes in flow disturbance with changes in plate thickness do not allow such straightforward comparison as per Table 4.4. It can be seen that in the midsection of the stack where x is approximately 0.126m, the critical

Table 4.4: Predicted $|\bar{u}_1|$, $\bar{M}_a$ and $\bar{M}$ values at Location M1 (Table 4.3) for each run. $\bar{M}_a\big|_{L_S/2}$ is found from Equation (4.9). $\bar{M}\big|_{L_S/2}$ is found from Equation (4.10). $N_{R,S}|_{L_S/2}$ values reported are maxima.

Run	BR	$\lvert\bar{u_1}\rvert_{L_S/2}$ (ms^{-1})	$\bar{M}_a\big\vert_{L_S/2}$	$\bar{M}\big\vert_{L_S/2}$	$N_{R,S}\big\vert_{L_S/2}$
1	1	8.16	0.007	0.0081	$(9.80)^2$
2	1	16.1	0.014	0.0160	$(19.3)^2$
3	1	24.1	0.021	0.0239	$(29.0)^2$
4	1	32.2	0.028	0.0319	$(38.8)^2$
5	0.98	8.38	0.007	0.0083	$(10.0)^2$
6	0.98	16.5	0.014	0.0164	$(19.8)^2$
7	0.98	24.7	0.021	0.0245	$(29.7)^2$
8	0.98	33.1	0.029	0.0328	$(39.7)^2$
9	0.90	9.38	0.008	0.0093	$(11.1)^2$
10	0.90	18.6	0.015	0.0185	$(21.9)^2$
11	0.90	27.8	0.023	0.0276	$(32.8)^2$
12	0.90	37.1	0.031	0.0368	$(43.7)^2$
13	0.80	11.1	0.008	0.0110	$(12.7)^2$
14	0.80	22.0	0.017	0.0218	$(25.4)^2$
15	0.80	32.9	0.025	0.0326	$(37.8)^2$
16	0.80	43.9	0.034	0.0436	$(50.4)^2$
17	0.70	13.5	0.009	0.0134	$(15.3)^2$
18	0.70	26.9	0.018	0.0267	$(30.5)^2$
19	0.70	40.7	0.027	0.0404	$(45.3)^2$
20	0.70	53.4	0.036	0.0530	$(60.3)^2$
21	0.70	66.7	0.046	0.0662	$(75.0)^2$
22	1	8.04	0.007	0.0080	$(9.68)^2$

Reynolds number criterion for turbulence of $N^c_{R,S} = (200)^2$ as defined by Thompson (1987) was not exceeded for Run 21. The conditions used in Run 21 led to the highest reported $|N_{R,S}|$ value of $(75)^2$, or approximately 14% of the $N^c_{R,S}$ limit value.

Table 4.4 shows that the numerical result $\bar{M}$ exceeds the calculated $\bar{M}_a$ result by around 10% to 15% for BR=1. As BR decreases, the ratio $\bar{M}/\bar{M}_a$ increases. This is because $\bar{M}_a$ is based upon the oscillatory pressure amplitude, whereas $\bar{M}$ is based upon the flow velocity which is more sensitive to the flow impedance of the stack region. As the plate thickness increases and the flow structure deviates further from that expected in linear theory, the ratio between $\bar{M}/\bar{M}_a$ increases. For non-linear studies of thermoacoustic couples, $\bar{M}$ is therefore a more suitable measure of nonlinear flow behaviour.

4.2.1.2 Vortex generation

Figures 4.8 and 4.9 illustrate the evolution of flow vortices at the left end of the stack for Run 20, over a full oscillatory period in ten 0.001s steps beginning at 0.200s. Pathlines are generated throughout the fluid domain and are coloured in these two figures according to the velocity magnitude. Pathlines could be considered as massless 'strings' which are useful in visualising the flow structure, and follow streamlines generated at each time step. The velocity direction at the inlet is indicated to the left of each figure to show the prevailing velocity in the centre of the device. A scale is provided at the top of each figure to indicate the spatial scales of the vortices generated.

In Figure 4.8(a), the fluid is predominantly moving rightward and decelerating. As the flow further slows, entrained flow over the lip of the plate edge results in a small recirculation zone forming below the inside plate edge (Figure 4.8(b)) and growing (Figure 4.8(c)) despite the prevailing flow velocity decreasing. Once

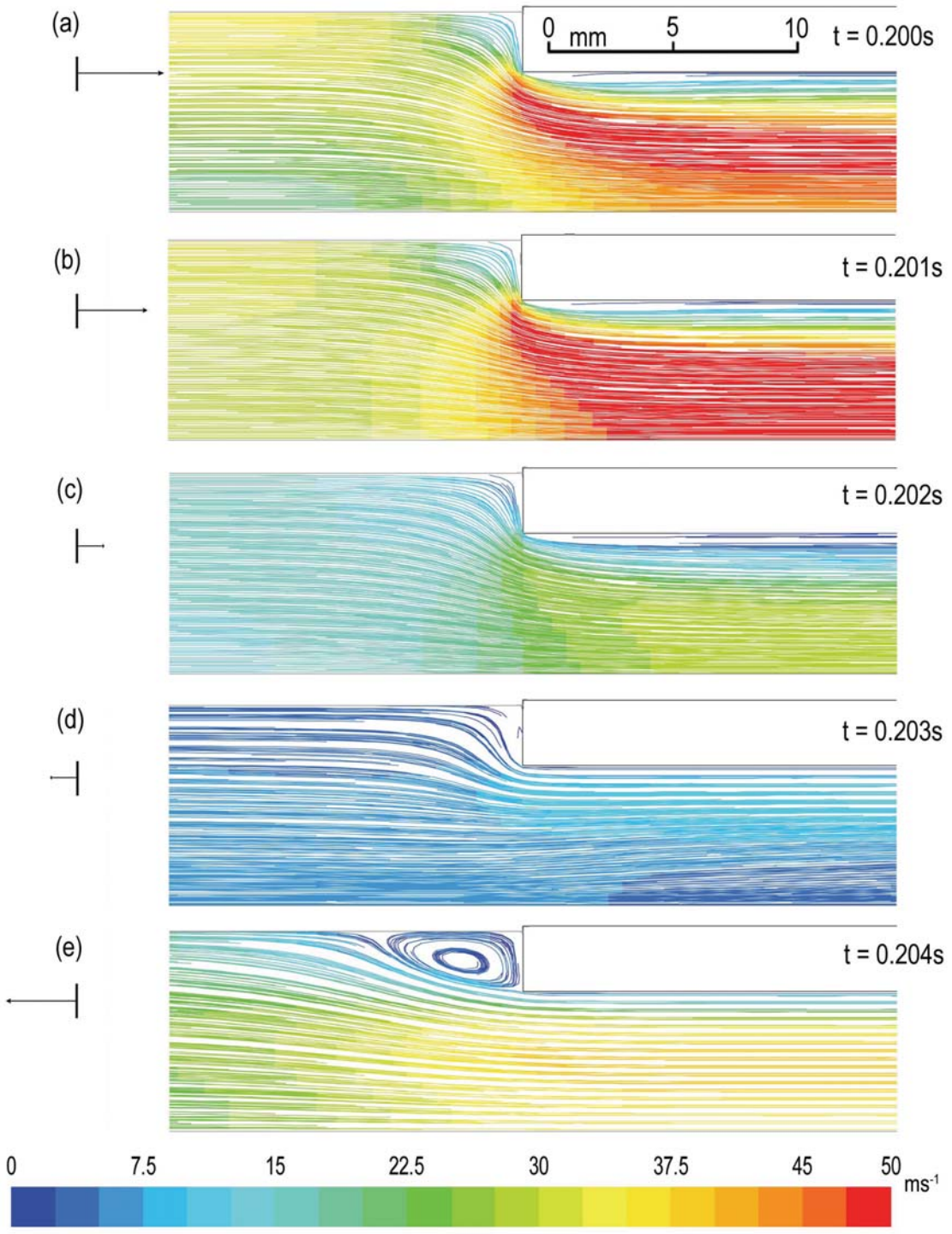

Figure 4.8: Flow pathlines for Run 20, at (a) t=0.200s, (b) t=0.201s, (c) t=0.202s, (d) t=0.203s, (e) t=0.204s. The prevailing flow direction and velocity magnitude are indicated to the left of each figure. Pathlines are coloured by velocity magnitude as indicated by the scale at the bottom of the figure.

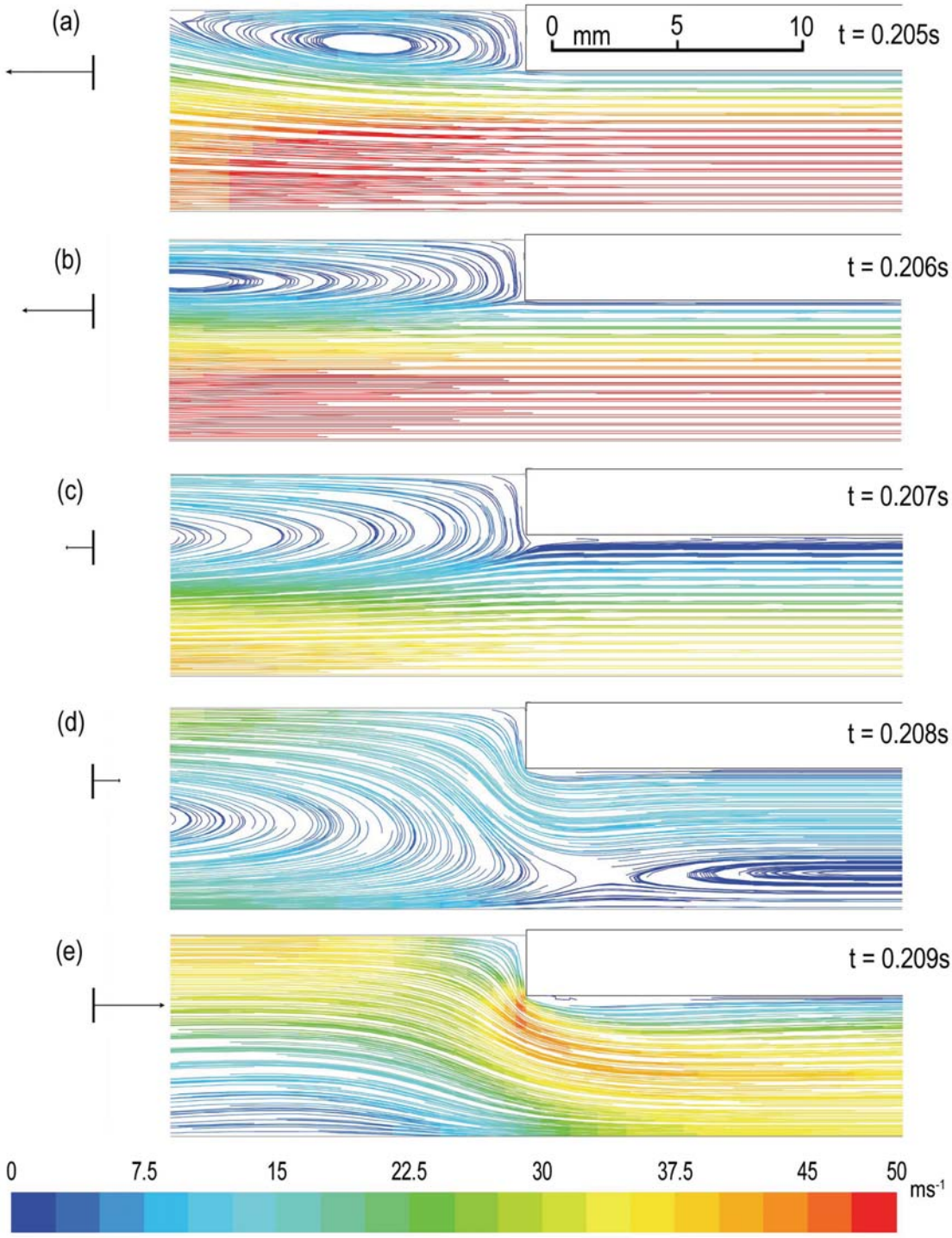

Figure 4.9: Flow pathlines for Run 20, at (a) t=0.205s, (b) t=0.206s, (c) t=0.207s, (d) t=0.208s, (e) t=0.209s. The prevailing flow direction and velocity magnitude are indicated to the left of each figure. Pathlines are coloured by velocity magnitude as indicated by the scale at the bottom of the figure.

the flow is arrested, this recirculation zone collapses and the flow moves leftward (Figure 4.8(d)).

Outside the stack and downstream of the stack plate edge, a flow separation and recirculation zone forms (Figure 4.8(e)) and as the free-stream velocity reaches its peak (Figure 4.9(a)), this recirculation zone increases in size. Figures 4.9(b) and 4.9(c) show that the flow of gas entering the domain from upper left becomes increasingly dominant, pushing the recirculating fluid further downwards. At t=0.208s (Figure 4.9(d)), flow entering from the top left of the figure is split into flow entering the stack (adjacent to the plate surface) and a large recirculation outside the stack region. By 0.209s (Figure 4.9(e)), the recirculation has completely collapsed, and flow upstream of the plate edge begins to approach uniformity to again repeat the cycle.

It can be seen that the structure shown in Figure 4.8(e) is similar to the result presented by Blanc-Benon et al. (2003) and reproduced in Figure 2.7. Although Run 20 uses helium for a working gas compared with air in the Blanc-Benon et al. analyses, and the two figures are produced for different time values two hundredths of a phase apart, the shapes of each recirculation zone are proportionately similar. The formation of separation zones on the plate inside edge observed in Figures 4.8(a) to 4.8(c) was also demonstrated by Worlikar & Knio (1996) for much lower drive-ratios ($DR \leq 1\%$).

4.2.1.3 Entropy generation

Figure 4.10 presents the rate of entropy generation $\dot{S}_{\text{gen}}$ with respect to drive-ratio DR for Runs 1 to 21, grouped by blockage ratio BR. This figure shows the increase in irreversible losses with increasing plate thickness $2t_s$ and drive-ratio DR, against previous results from Ishikawa & Mee (2002) and an analytical estimate of $\dot{S}_{\text{gen}}$

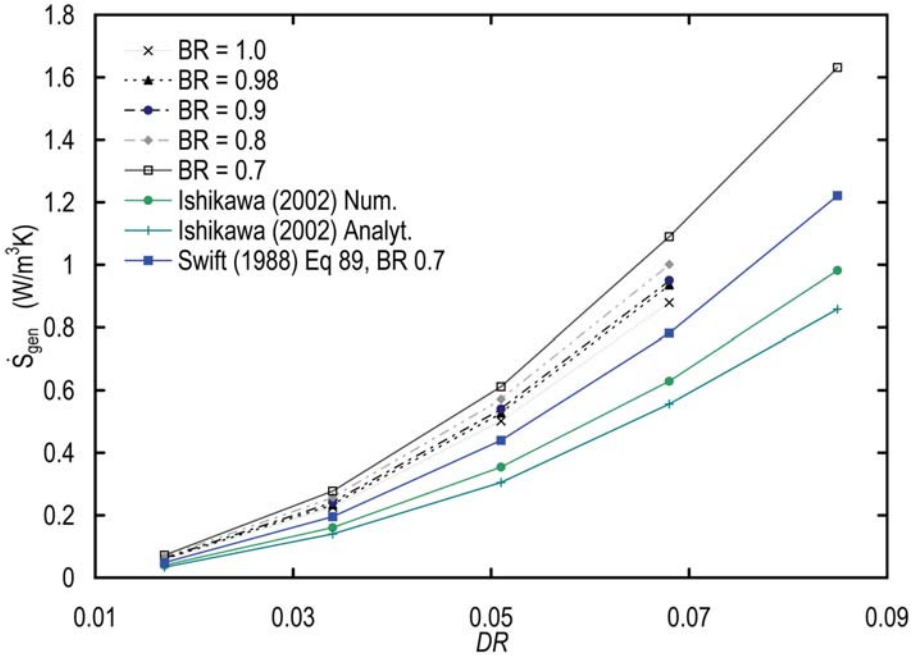

Figure 4.10: Rate of entropy generation $\dot{S}_{\text{gen}}$ versus drive-ratio DR, with selected runs grouped by blockage ratio, as follows: BR=1.0 (Runs 1 to 4), BR=0.98 (Runs 5 to 8), BR=0.9 (Runs 9 to 12), BR=0.8 (Runs 13 to 16), BR=0.7 (Runs 17 to 21). The analytical result of Swift was generated from use of Equation 89 of Ref. (Swift 1988).

calculated as (Swift 1988, Equation 89)

$$\dot{S}_{\text{gen}} = \frac{(L_S + 2t_s)\omega}{4T_0 V}\left[\frac{(p_1^s)^2}{\rho_m c^2}\delta_\kappa \frac{\gamma - 1}{1 + \epsilon_s} + \rho_m (u_1^s)^2 \delta_\upsilon\right] \tag{4.16}$$

where ϵ_s is the heat capacity ratio given by (Swift 1988, Equation 59)

$$\epsilon_s = \frac{\rho_m c_{pk} \delta_\kappa \tanh[(1+j)y_0/\delta_\kappa]}{\rho_s c_{ps} \delta_{\kappa s} \tanh[(1+j)t_s/\delta_{\kappa s}]}. \tag{4.17}$$

and $\delta_{\kappa s}$ the thermal penetration depth in the solid material. In Equation (4.16), the superscript 's' designates values assumed to be constant throughout the stack region, from application of the short stack approximation.

It can be seen from Figure 4.10 that the entropy generation rate $\dot{S}_{\text{gen}}$ obtained

in the present study using a thermoacoustic couple modelled with zero thickness is approximately 40% higher than that calculated by Ishikawa & Mee. However this result is attributed in part to the use here of a mesh density five times greater in the axial direction than that used previously by Ishikawa & Mee. Whilst the axial dimension of subdomain 'A' (Figure 3.1) is also noted to be approximately 75% greater than the equivalent region in the domain used by Ishikawa & Mee (2002), the zones in which the rate of entropy generation is significant are well within regions common to both models.

The analytical result for $\dot{S}_{\text{gen}}$ utilising Equation 89 of Swift (1988) is shown to exceed the numerical results of Ishikawa & Mee by typically 13 to 15% for BR=0.7. This is expected since the finite plate thickness leads to increased gas velocity u_1, which increases the viscous shear dissipation component in Equation (4.16) and hence $\dot{S}_{\text{gen}}$.

4.2.2 Heat transportation

4.2.2.1 Comparison with other models

Figure 4.11 presents the time-averaged heat flux across the plate surface in the y-direction $\left\langle \dot{h}_y \right\rangle_t$ versus axial position x for Run 22 of the current study and Run 1 of Piccolo & Pistone (2006). These results show that there is good agreement between the two results and hence the current model was able to reproduce the previous work for thermoacoustic couples of zero thickness. The slight differences between the results is to be expected because the temperature at the surface of the plate is not fixed at T_0 in the present study whereas it was fixed in the study by Piccolo & Pistone (2006).

The sign conventions used in this paper are such that positive $\dot{h}_y$ indicates net heat transfer from the plate to the working fluid and negative $\dot{h}_y$ indicates net heat

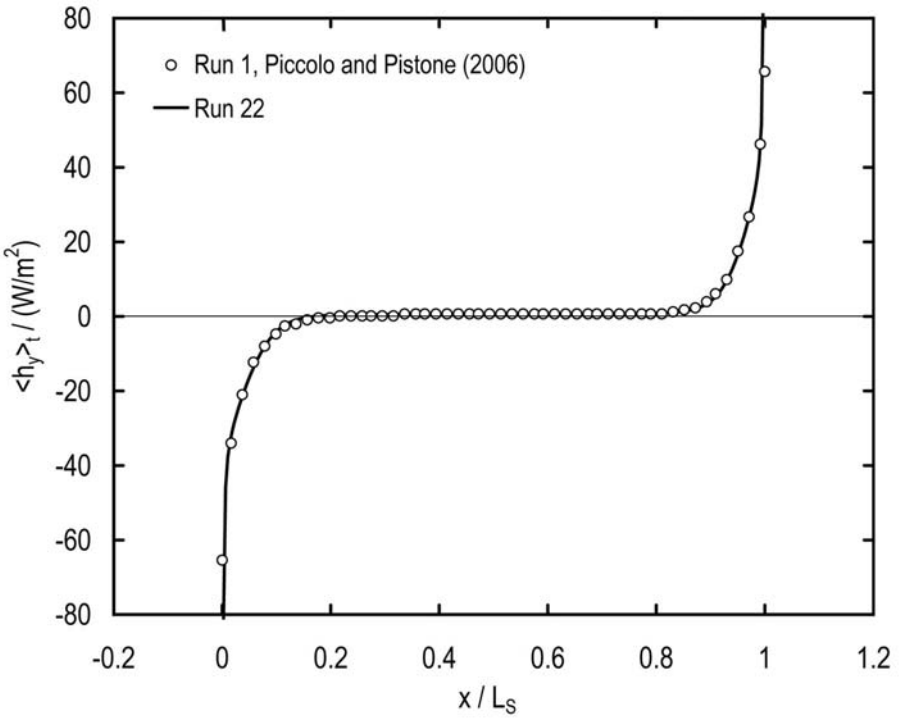

Figure 4.11: Distribution of time-averaged heat flux in the y-direction $\left\langle \dot{h}_y \right\rangle_t$ along the horizontal plate surface according to axial position x. Open circles are approximate numerical data from the study of Piccolo & Pistone (2006, Run 1). Positive $\dot{h}_y$ indicates net heat transfer from the plate to the working fluid.

transfer from the working fluid to the plate. The time-averaged heat flux across the plate surface in a thermoacoustic couple is shown to be concentrated at the extremities or edges of the plate surface, and appears symmetric across the plate midpoint. In fact, the distribution of $\dot{h}_y$ is asymmetric in a thermoacoustic couple, for reasons such as the variation in velocity amplitude along the length of the stack. Figure 4.11 appears symmetric since the thickness of the plate is not modelled. The results from Run 1 indicate that the point at which $\left\langle \dot{h}_y \right\rangle_t$=0 is not x=0.5L_S, but rather $x \approx 0.2L_S$. This is attributed to a positive bias in $\dot{h}_y$ across the plate surface.

4.2.2.2 Thermophysical cycles

In Figure 4.12, temperature-entropy ('T-s') graphs are plotted for Run 1 at limit state for selected locations. The plot of temperature versus entropy for the position M1 is almost a straight line instead of a 'loop', so the oscillations of the gas at

location M1 are effectively adiabatic. However, the cycles experienced at locations C1 and H1 are noticeably different. Locations C1 and H1 are located along y=0, at more than three times the mean thermal penetration distance from the plate surface. The T-s curves at these two locations are perturbed, whereby the T-s curve is expanded at locations C1 and H1 for the phases in the limit cycle for which the heat transfer between the fluid and plate is highest at their respective locations. This suggests that effective heat transportation is occurring at these locations despite their distance to the stack plate being significantly greater than the thermal penetration depth.

Locations C2 and H2 are much closer to the stack plate surface (0.5 $\delta_{\kappa m}$) and are shown in Figure 4.12 to witness higher levels of time-averaged (effective) heat transfer with the plate surface. The 'folded' or 'figure of 8' curves at Locations C2 and H2 indicate that there is an effective transfer of heat, whereas the open, elliptical shape of the curve for Location M2 indicates a storage of potential energy instead. This supports the view that the time-averaged heat transfer to the plate occurs only at the plate edges, as indicated in Figure 4.11.

Figure 4.13 shows the temperature versus entropy for Run 4 and Run 20 during limit state operation at selected locations. The major difference between Runs 4 and 20 is the value of t_s: Run 4 has a plate of zero thickness, whereas Run 20 has a 2.4mm thick plate. This figure gives insight into the influence of the blockage ratio upon the thermophysical cycles obtained on y=0 at each end of the stack plate. In Section 4.2.1, it was evident that increasing the plate thickness increases the magnitude of flow recirculation. The distortion of T-s curves obtained for Run 20 relative to Run 4 supports this view. In Figure 4.13, indicators 'A' and 'B' designate phases in the cycle for which large flow recirculations outside the stack region (see Figure 4.9(d)) influence the T-s curve. The 'indentations' in the T-s curves indicated

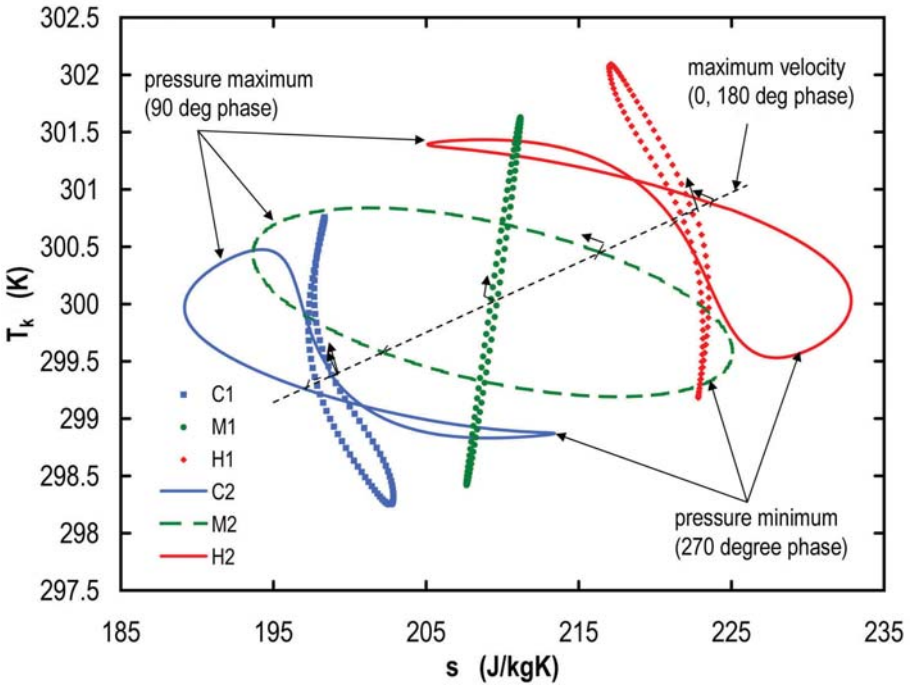

Figure 4.12: Temperature versus entropy cycles at limit state for Run 1 for selected fixed positions defined in Table 4.3. The position and direction of the cycle at the 2000th time step (flow time 0.2s) is indicated with a solid arrow. Phases of maximum and minimum pressure are indicated for locations C2, M2 and H2.

by 'A' and 'B' are due to flow recirculation zones entraining fluid at the edges of the stack region. Specifically, these recirculation zones are non-linear flow effects which are shown to influence the effectiveness of the thermoacoustic couple. Whilst these recirculation zones are shown to increase the rate of entropy generation, they also improve the rate of thermal diffusion at each end of the stack and increase the local rate of heat transfer. The impact of the flow structure upon effective heat transfer is discussed in more detail in the following section.

4.2.2.3 Evolution of thermoacoustic couple heat flux distribution

The evolution of the distribution of normalised transverse heat flux $\dot{h}_y$ through the plate surface for Run 1 is shown in Figure 4.14. The transverse heat flux is normalised to eliminate bulk gas compression effects as per the method described in Appendix C.1. The surface plot is given for the timeframe t=0.2s to 0.21s, and negative heat flux indicates heat transfer from fluid to the plate (i.e. cooling of

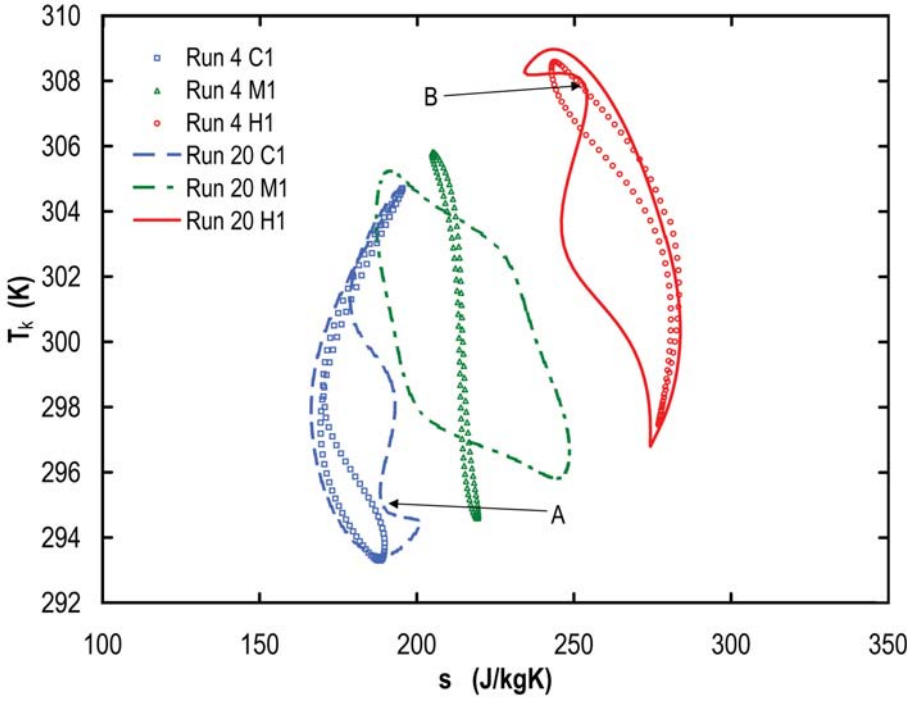

Figure 4.13: Limit state behaviour of temperature versus entropy for Runs 4 and 20 at Locations C1, M1 and H1.

the surrounding gas). Figure 4.15 shows a similar plot for Run 20, which differs to Run 1 in blockage ratio (0.7 in Run 20 and 1.0 in Run 1) and drive ratio (6.8% in Run 20 and 1.7% in Run 1). It is important to note that whilst Figures 4.14 and 4.15 do not include the axial heat flux $\dot{h}_x$ through the edges of the stack plate for clarity, this component of the overall heat flux through the solid-fluid boundary $\dot{h}_{hx}$ is significant, as will be further described in Section 4.2.2.4.

The results shown in Figures 4.14 and 4.15 show the four distinct phases of heat transfer. The cycle can be broken down into phases of compression, heating, expansion and cooling, each of 90° phase duration in a similar manner to most studies discussing the operation of standing-wave thermoacoustic devices (Swift 1988, Ceperley 1979). At 0.2s, the positive (rightward) velocity maximum should denote the midpoint of the compression phase, since at this point in time the pressure is increasing and the velocity is decreasing from a maximum (Figures 4.9(c) and 4.9(d)). However, thermal delays in the system are present and so there

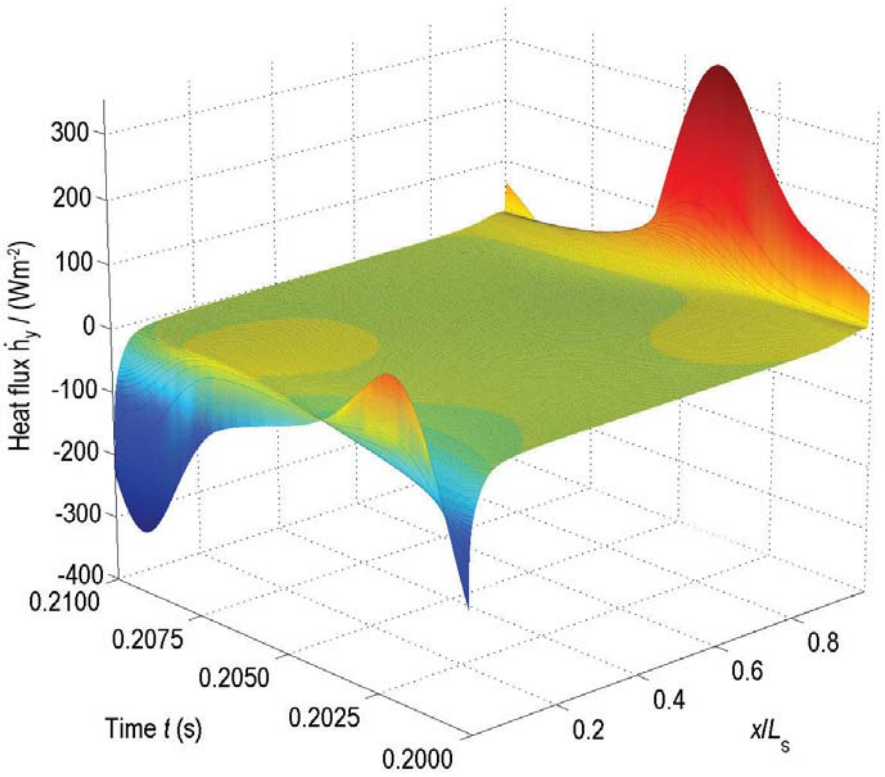

Figure 4.14: Surface plot of normalised transverse heat flux $\dot{h}_y$ (Appendix C.1) through the horizontal plate surface for the limit state cycle of Run 1. Surface colour mapping indicates positions of cooling (blue) and heating (red).

exists a phase bias in the commencement of each cycle.

The heating phase for Run 1 is apparent at around 0.2012s, with heat transfer to the fluid occuring at both ends of the thermoacoustic couple. The cycle then shifts to an expansion phase which begins at around 0.2037s, and leads to the cooling phase denoted by the significant decrease in $\dot{h}_y$ near x/L_S=0. The distribution of $\dot{h}_y$ in the centre of the stack is relatively even for the vertical scale presented, and this again demonstrates the concentration of effective heat transfer to the edges of the stack plate.

Heating and cooling phases for Run 20 are readily seen in Figure 4.15, and there are several interesting phenomena occurring deep inside the stack region. Note that the vertical scaling used in Figure 4.15 is over five times that of Figure 4.14,

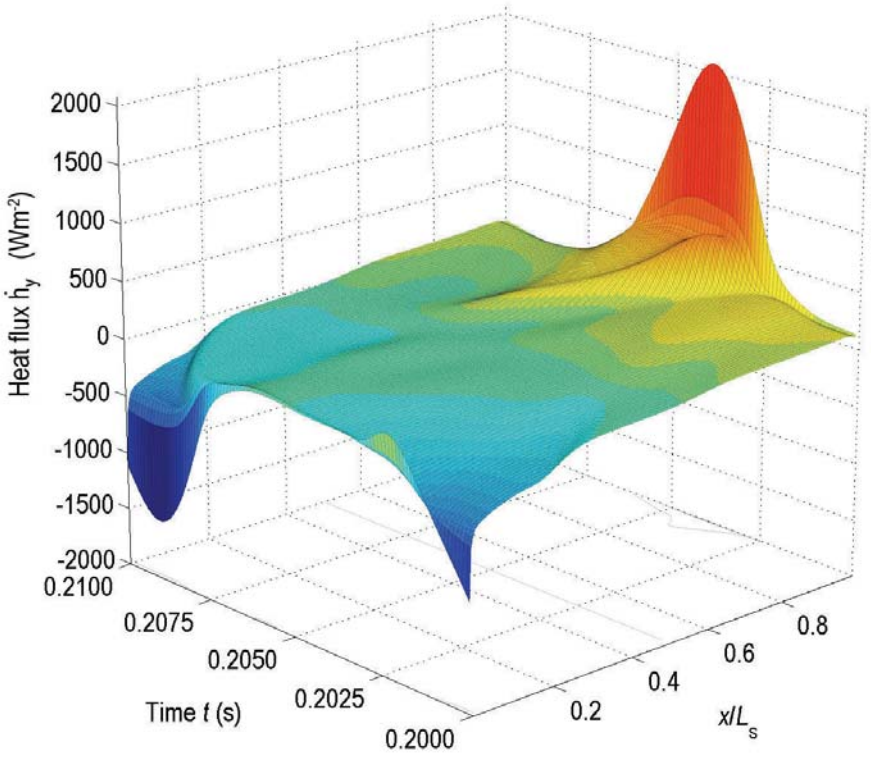

Figure 4.15: Surface plot of normalised transverse heat flux $\dot{h}_y$ (Appendix C.1) through the horizontal plate surface for the limit state cycle of Run 20. Note the difference z-axis scaling to Figure 4.14. Surface colour mapping indicates positions of cooling (blue) and heating (red).

despite the drive ratio being only four times higher. At approximately t=0.2088s, a sharp decrease in $\dot{h}_y$ (effective cooling) can be seen to 'spread' into the stack region. The flow structure about x/L_S=0 during the cooling phase for Run 20 is shown in Figures 4.9(d) and 4.9(e). Half a period earlier at t=0.2038s, a sharp increase in $\dot{h}_y$ near x=L_S also 'spreads' in towards the stack region.

With reference to Figure 4.13, the phase indicated by 'A' corresponds to t=0.2088s at the 'cold' end, the same time and location at which the sharp (desired) decrease in $\dot{h}_y$ is evident in Figure 4.15. The indicator in 'B' in Figure 4.13 corresponds to the 'hot' end of the stack plate at t=0.2038s where a desirable increase in $\dot{h}_y$ is also found. At both locations and phases for which the transverse heat flux $\dot{h}_y$ is improved, the flow is accelerating into the stack region immediately

following the collapse of laminar flow recirculation zones in the vicinity of the stack edge.

4.2.2.4 Plate edge heat transfer

The results presented so far have demonstrated a thermoacoustic heat-pumping effect from the left side (x=0) to the right side (x=L_S) of the plate. Time-averaged temperatures of gas in the vicinity of the left side ('cold end') have decreased, and temperatures on the right side ('hot end') have increased.

Figure 4.16 shows the relative magnitude of axial heat flux through the plate ends in comparison to transverse heat flux through the plate facing for Run 20. The time-averaged heat flux via each of the left ('cold') and right ('hot') plate ends $\langle \dot{h}_x \rangle_t|_{\text{cold}}$ and $\langle \dot{h}_x \rangle_t|_{\text{hot}}$, can be compared to the time-averaged heat fluxes $\langle \dot{h}_y \rangle_t|_{\text{cold}}$ and $\langle \dot{h}_x \rangle_t|_{\text{hot}}$ through the plate horizontal surface. For Run 20, the point at which the time-averaged transverse heat flux is zero was found to be slightly closer to the cold end of the plate (4% of L_S). The transverse heat flux through surfaces forming the physical ends of the plate is shown in Figure 4.16, and more found to be significant fractions of the total heat flux through the plate. Also of interest is the higher proportion of heat leaving the plate than that entering. This demonstrates a time-averaged net loss in thermal energy within the plate material.

4.2.2.5 Effect of blockage ratio upon heat transfer rate

Figure 4.17 shows the time-averaged transverse heat flux, and indicates that increasing the half-thickness of the stack plate (t_s) (and hence decreasing the blockage ratio BR) leads to a greater effective heat transfer through the plate surface (i.e. a larger integral of $\langle \dot{h}_{hx} \rangle_t$ across the surface of the plate) and hence improves the performance of the thermoacoustic couple. This performance increase comes at the expense of increased flow and entropy losses, as discussed in Section

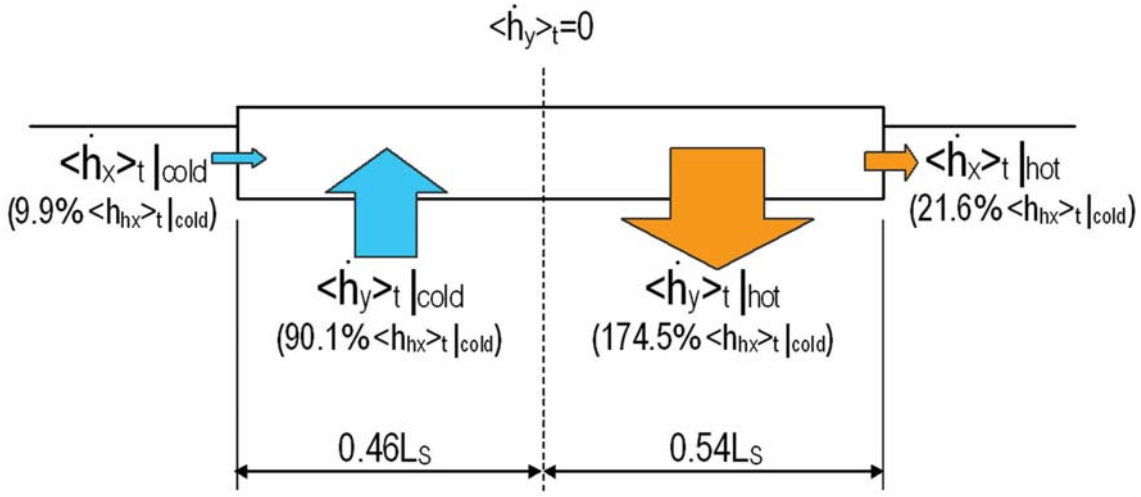

Figure 4.16: Sketch showing the proportion of time-averaged heat flux through the plate surface for limit-state operation of Run 20. Percentage values quoted are referenced to the total heat flux entering the plate over an oscillatory cycle, $\langle \dot{h}_{hx} \rangle_t|_{cold}$.

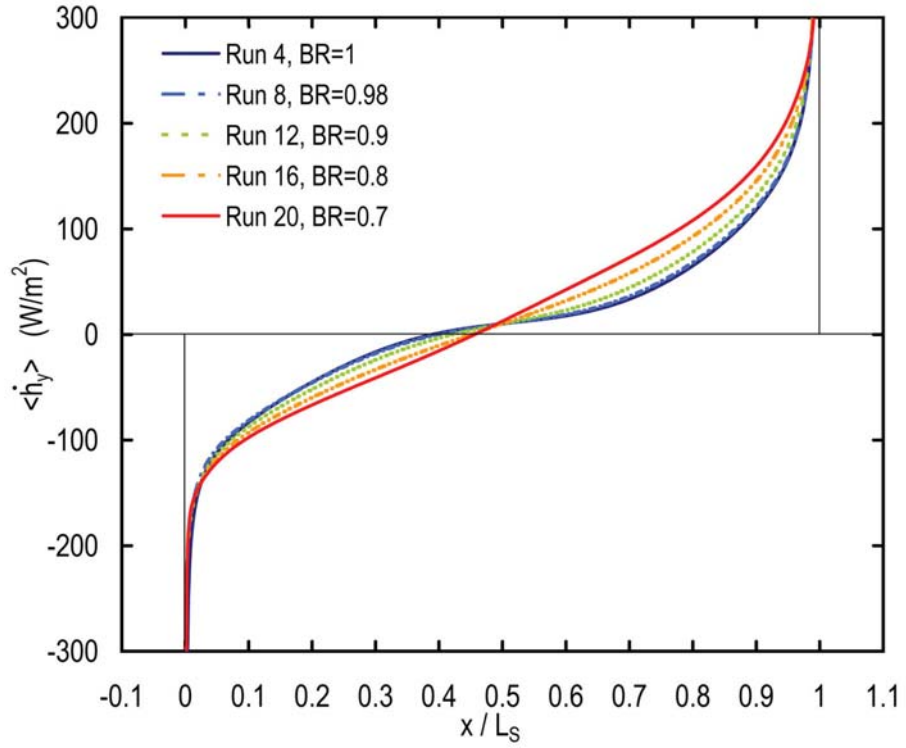

Figure 4.17: Time-averaged transverse heat flux for DR=6.8% and increasing BR. Data shown is for Run 4 (t_s =0), Run 8 (t_s =0.16mm), Run 12 (t_s =0.8mm), Run 16 (t_s =1.6mm) and Run 20 (t_s =2.4mm).

4.2.1.3.

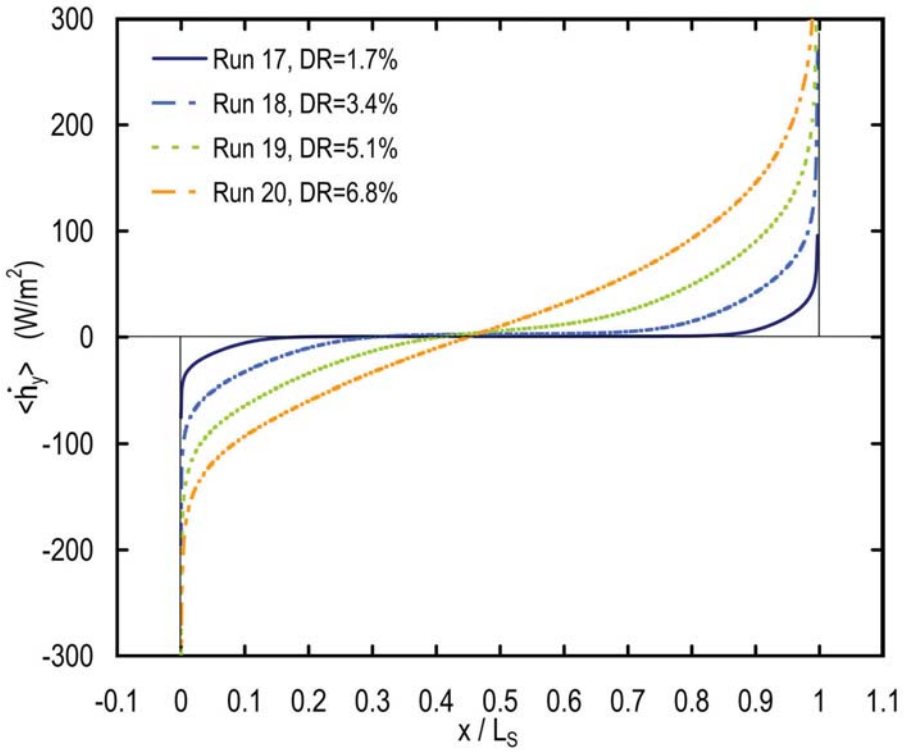

Figure 4.18: Time-averaged transverse heat flux for BR=0.7 and increasing DR. Data shown is for Run 17 (DR=1.7%), Run 18 (DR=3.4%), Run 19 (DR=5.1%) and Run 20 (DR=6.8%).

Figure 4.18 presents the distribution of time-averaged transverse heat flux for increasing drive ratio DR with constant blockage ratio BR. As the drive-ratio increases, a greater area of the plate participates in the contribution of effective heat transfer. For a constant ratio of plate half-spacing to mean thermal penetration depth, Piccolo & Pistone (2006, Figure 3) showed numerically that the normalised distribution of $\langle \dot{h}_y \rangle_t$ is weakly dependent on the gas displacement amplitude. It follows then that as the gas displacement amplitude is increased (by increasing the drive-ratio) whilst y_0/δ_κ is held constant through constant BR and δ_κ, the distribution in time-averaged transverse heat flux is similar but nonetheless different in magnitude between Runs 17 to 20.

Figure 4.19 presents the time-averaged difference in area-weighted average gas temperature, normalised by the result obtained using Runs 1 to 4 with a blockage

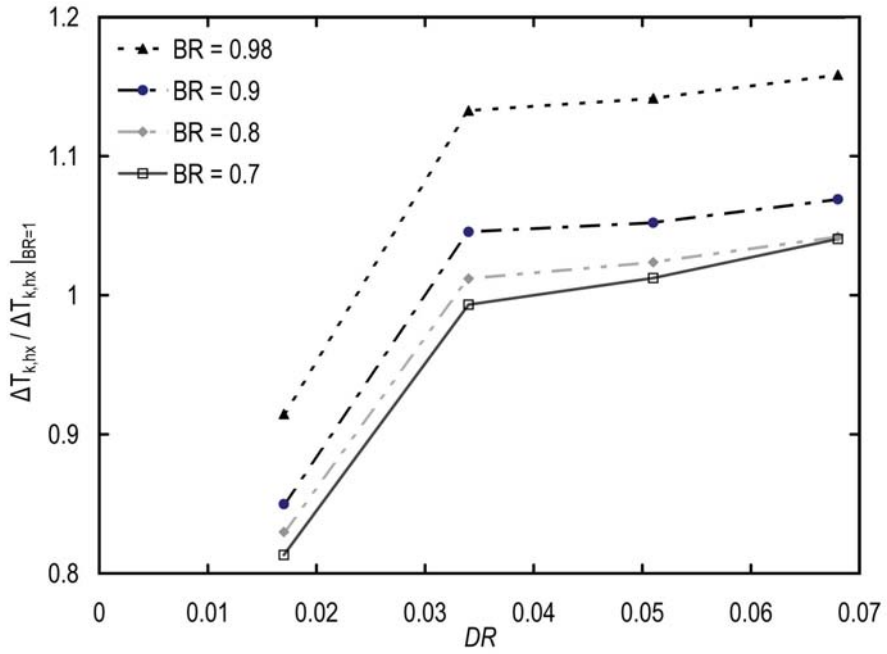

Figure 4.19: Time-averaged difference in area-weighted average gas temperature normalised by same result obtained using a blockage ratio BR of 1 (Runs 1 to 4) versus drive-ratio DR. Data is presented from Runs 5 to 8 (BR=0.98), Runs 9 to 12 (BR=0.9), Runs 13 to 16 (BR=0.8) and Runs 17 to 20 (BR=0.7).

ratio of 1, plotted as a function of the drive-ratio. This figure provides a comparison of the increase in temperature difference across the stack with increasing t_s and DR. For a drive-ratio of 1.7%, it can be seen that the performance of the stack is reduced with increasing plate thickness $2t_s$. However, for all drive-ratios considered above 3%, the performance of thermoacoustic couples with finite-thickness was actually better than the zero-thickness condition (BR=1). Regardless of drive-ratio, it is evident that for thermoacoustic couples of rectangular cross section, maximising BR will enable an increase in the performance scale $\Delta T_{k,hx}$. However, the influence of subdomain 'H' (Figure 3.1) may be significant at such a small plate thickness and a source of error in the results presented here. The thickness (one mesh element) and hence influence of subdomain 'H' is intended to be minimal compared to that of subdomain 'P'. As we seek to move away from models of zero thickness plates, it is perhaps beyond the scope of the current work to quantify its influence.

As noted in previous work by Poese & Garrett (2000), drive-ratios above 3% cannot be expected to correspond to a linear increase in the performance of the stack, and this is shown in Figure 4.19, with the normalised $\Delta T_{k,hx}$ not increasing linearly with DR above 3%. Higher order effects such as the increased rate of entropy generation and viscous losses are considered contributors to this result. Interestingly, the performance increase from DR=5.1% to DR=6.8% is noticably greater than for DR=3.4% to DR=5.1%, although a specific cause for this result is as yet unidentified.

4.3 Conclusions

The results from this study indicate that flow impedances from non-zero thickness stack plates and other fixed objects in the acoustic field will introduce flow and heat transport effects. This study has confirmed results of studies by Ishikawa (2001) and Piccolo & Pistone (2006), and further to the study of Besnoin (2001), investigated the impact of flow recirculation upon the heat transfer performance of a thermoacoustic couple. In achieving this, the current study has addressed the first two 'gaps' in the knowledge detailed in Section 2.4, namely the lack of knowledge with regards to the understanding and modelling of the undesirable loss mechanisms in parallel plate stacks of thermoacoustic devices operating at drive ratios in excess of 3%, and the influence of stack plate thickness upon the distribution of effective heat transfer and efficiency of a thermoacoustic couple at drive ratios in excess of 3%.

Results from the current study indicate that the stack plate thickness and hence blockage ratio strongly controls the generation of vortices outside the stack region and perturbs the flow structure and heat flux distribution at the extremities of the plate. Increases in plate thickness are also shown to improve the integral of the total heat transfer rate but at the expense of increased entropy generation.

The results presented for the flow of fluid inside the thermoacoustic couple shows the generation of vortices around the edges of the stack plates. In practice, typical parallel or rectangular section stacks do not have perfectly square edges. Previous research in thermoacoustic couples has considered only rectangular or zero-thickness (1-D) plates. Hypothetically, it might be possible to improve the heat transfer performance through the stack plate if non-rectangular cross sections, such as rounded or elliptical shaped edges were used. The next chapter describes a CFD analysis of stack plates with profiled edges to investigate this hypothesis.